Dipl.-Ing. Wolfgang Fuchs, BSc

Investigation of Paper - and Printing Process Related Reasons for Print Unevenness

DOCTORAL THESIS

to achieve the university degree of

Doktor der technischen Wissenschaften

submitted to

Graz University of Technology

Supervisor

Assoc.Prof. Dipl.-Ing. Dr.techn. Ulrich Hirn

Institute of Pulp, Paper and Fibre Technology
Graz University of Technology

Prof. D. Steven Keller, Ph.D.
Department of Chemical, Paper and Biomedical Engineering, Miami University, Oh, USA

Graz, September 2016

AFFIDAVIT

I declare that I have authored this thesis independently, that I have not used other than the declared sources/resources, and that I have explicitly indicated all material which has been quoted either literally or by content from the sources used. The text document uploaded to TUGRAZonline is identical to the present doctoral thesis.

Date	Signature

Abstract

Print unevenness is a major component of print quality. For different printing techniques, specific paper properties, such as the electric properties for the xerographic printing or the wetting behaviour of inkjet paper are important.

The conventional approach to reveal the paper related reasons for print unevenness is to measure overall paper properties (e.g. basis weight, gloss, opacity). These single values are then correlated to single print unevenness values, such as the mottle index. The aim of this work was to utilise a different approach to assess print unevenness. This approach was based on the measurement of local paper properties and linking them to the local print reflectance after printing. Furthermore, statistical analysis of the obtained local paper property and print reflectance maps was performed. Multiple linear regression revealed the relevance of the local paper properties with regards to the particular printing technique. Print unevenness was examined for three printing techniques, xerographic –, inkjet – and sheet fed offset printing. For each printing technique the corresponding paper grades were analysed. Printing of the samples was performed on industrial printing machines. The results revealed that for coated paper grades, local variation in coating coverage were the most important factors explaining print unevenness (up to 55 %). Furthermore, local variations in topography, brightness and gloss contributed to the models. For uncoated paper grades, local optical properties and in case of a printing nip in the printing machine, local topography and thickness variation contributed to the models.

Moreover, the influence of the printing machine in sheet fed offset printing was elucidated by tracking the print unevenness over more than 3000 sheets. It was shown, that print mottle patterns were stable in location and over a rather high number of printed sheets. The similarity of print mottle patterns between two consecutively printed sheets was up to 50 % and the similarity of print mottle patterns between two printed sheets, 3000 sheets apart from each other in a printing stack was up to 30 %. However, this effect was not observed for full tone colour fields.

Keywords: printing, print unevenness, print mottle, local paper properties, sheet fed offset, xerography, inkjet, coating coverage

Kurzfassung

Druckqualität ist ein wichtiger Bestandteil der Druckqualität. Hinsichtlich Druckqualität, stellt jede Drucktechnik bestimmte Anforderungen an das jeweilig verwendete Papier. Zum Beispiel, spezielle elektrische Eigenschaften beim Xerografie Druck oder das Benetzungsverhalten beim Inkjet Druck. Traditionell werden papierbezogene Kennzahlen (z.B.: Weiße, Glanz, Opazität) ermittelt, um die vom Papier verursachte Druckunruhe abzuschätzen. Diese Kennzahlen werden in weiterer Folge mit Kennzahlen des Druckbilds (e.g. Mottle Index) korreliert. In der vorliegenden Arbeit wurde ein innovativer Zugang gewählt, um die vom Papier verursachte Druckunruhe zu bestimmen. Der Ansatz basiert auf der Messung lokaler Papiereigenschaften und deren punktweiser Korrelation zur lokalen Druckdichte. Anschließende multiple lineare Regression gibt Auskunft über die Relevanz oder Redundanz der vermessenen Papiereigenschaften bezüglich Druckunruhe.

Drei verschiedene Drucktechniken wurden untersucht: Xerografie -, Inkjet - und Bogenoffset Druck. Für jede Drucktechnik wurden die zugehörigen Papiere vermessen und auf Druckmaschinen in Industriemaßstab verdruckt. Die Ergebnisse zeigten, dass für gestrichene Papiere, lokale Variationen in der Strichabdeckung für Druckunruhe verantwortlich waren; bis zu 55 % der Druckunruhe wurden dadurch erklärt. Darüber hinaus, konnten Variationen in lokaler Topografie, Weiße und Glanz einen Teil der Druckunruhe erklären. Für ungestrichene Papiere waren Variationen in lokalen optischen Eigenschaften und, im Falle eines vorhandenen Drucknips, lokale Topografie und Dickenvariation von Bedeutung.

Zusätzlich wurde der Einfluss der Druckmaschine im Bogenoffset bewertet. Hierfür wurde bei mehreren Drucktests die Druckunruhe über mehr als 3000 Bögen untersucht. Es konnte gezeigt werden, dass die Muster der Druckunruhe zweier unmittelbar aufeinander folgender Bögen bis zu 50 % korrelierten. Diese Korrelationen wurden in sogenannten Ähnlichkeitsmatrizen dargestellt. Weiter konnte gezeigt werden, dass die Korrelation zweier Druckunruhemuster von Bögen, die 3000 Bögen entfernt voneinander im Stapel bedruckt worden sind, bis zu 30 % beträgt. Dieser Effekt beziehungsweise diese Korrelation wurde nur für Rastertöne, aber nicht für Volltöne gefunden.

Acknowledgements

I want to thank Univ.-Prof. Dr. Wolfgang Bauer for his support and the great possibility to write this thesis at the Institute of Paper, Pulp and Fibre Technology. His helpful advices were very important for the development of the different approaches in this thesis. I am grateful to my supervisor Assoc.Prof. Dr. Ulrich Hirn for spending a lot of time in discussing new ideas and aspects. Additionally, for his support and constructive advises where I greatly benefited from. Furthermore, I am thankful to Prof. Dr. Steven Keller for his support and fruitful discussions during his stay in Graz as a guest professor and for reviewing this thesis.

I want to thank Claudia Bäumel and Kerstin Schefzik for their support with administrative tasks, Harald Streicher for keeping my computer up to date. I am also thankful to Adelheid Bakhshi and the whole laboratory staff for helping in the laboratory. Thanks to Anton Albert and Gerhard Massek supporting me during the print trials. I am grateful that Michael Dauer shared his huge MATLAB knowledge with me. Many thanks to Daniel Mandlez for helping me throughout the whole project duration.

I am very grateful to Dr. Wolfgang Fischer, Dr. Christian Lorbach, Dr. Albrecht Miletzky, Dr. Frederik Weber and Dr. Wolfgang Pacher for being great colleagues and friends as well as Rafael Giner Tovar, Marina Jajcinovic, Dr. Jussi Lahti, Georg Urstöger, Lukas Jagiello, Samir Kopacic, Dr. Matthias Trimmel and Melanie Mayr.

I would like to acknowledge Andritz AG, BASF AG, Mondi Frantschach, Mondi Neusiedler GmbH, Océ N.V., Omya AG, SAPPI Gratkorn GmbH, Stora Enso AG and the Austrian research promotion agency FFG for funding this research project.

My deepest dept of gratitude is to my parents Walter and Theresia for their unlimited love and support. They, Viktor and Karoline encouraged me throughout my whole lifetime. Last but not least, I want to thank my girlfriend Lucia for her support and listening to my problems.

Wolfgang Fuchs
Graz, 22.09.2016

Contents

List of Figures

List of Tables

Chapter 1

Introduction

1.1 Scope of the thesis

Print quality is often related to print unevenness (also cloudy print), which are disturbances in the printed image. Instead of print unevenness the term print mottle is often used. Print mottle can be defined as the undesired unevenness of the perceived print colour, print density or print gloss (Eid et al., 2008). The three main elements in printing are the printing machine (e.g. sheet fed offset, heat set web offset, inkjet or xerography), the printing substrate (e.g. various paper grades) and the ink (e.g. offset printing ink, dry toner, liquid toner, aqueous inkjet ink). Print mottle is generated by either one of the three main components or an imperfect interaction of two or more main components involved during printing.

This thesis is mainly concerned with the investigation of the substrate (i.e. paper) related reasons for print unevenness or mottle respectively. From the manifold printing techniques available, the thesis focuses on sheet fed offset printing, xerography printing and inkjet printing.

The conventional procedure to evaluate printing paper grades regarding print unevenness is to measure overall paper properties (e.g. basis weight, gloss, brightness, PPS roughness, opacity, ...). The approach in this thesis, instead of measuring overall paper properties, is to measure the paper properties locally with high resolution measurements which captures the local variation in local paper properties caused for example by flock structure in the paper, which yield information unattainable by conventional methods (Chinga-Carrasco, 2009). This is performed by utilising both, established high resolution measurement techniques and novel techniques. Measuring local paper properties in combination with registration (i.e. image alignment) of printed samples enables statistical modelling of the reasons for print unevenness. The result of statistical modelling directly reveals the effect of different local paper properties on the print unevenness. For example, it is well known that coating layer uniformity influences print quality in sheet fed offset printing, but the approach of statistical modelling might show to which extent.

Furthermore, the influence of the printing machine has been evaluated for two different sheet fed offset printing machines. This shows the importance of perfect interaction between the three main components during the printing process.

1.2 Relationship between local paper properties and print unevenness

Figure 1.1 shows an example for print unevenness. The arrows in Figure 1.1b indicate regions where the image is perceived inhomogeneous. Within this regions the print composes of several zones of lighter an darker areas. This inhomogeneities may origin from local variations in ink penetration into the paper (Engström and Rigdahl, 1992). In addition, variations in other factors could cause this inhomogeneities such as brightness, opacity, gloss, surface roughness, topography and basis weight. The hypothesis is that lower variation in local paper properties leads to an even printed image. In terms of print unevenness it is more important to control local variation of single paper properties rather than concentrating on overall or absolute values of paper properties.

(a) Even printed image. **(b)** Uneven printed image.

Figure 1.1 Comparison of two printed images: **(a)** even printed image and **(b)** uneven printed image (arrows indicate enhanced regions of unevenness).

What does local exactly mean? The term local basically describes the measure scale or the resolution of the image acquisition device. Within this thesis, the majority of the obtained two dimensional data maps exhibit a pixel size between 1 µm/pixel to 100 µm/pixel. However, statistical modelling is subsequently performed at the scale where the structures effect the visual perception of the human eye (i.e. 2 mm to

8 mm). This scale is considered to be the macro structure of paper. Thus, the scale of local is equivalent to millimeter (or macro) scale (Chinga-Carrasco, 2009).

In order to clarify the interrelation between local paper properties and print unevenness a significant number of research activities has focused on the analysis of local paper properties being able to evaluate and predict the final print quality. In most cases one local paper property was selected and examined with regard to one specific printing technique. Subsequently a correlation between one print quality parameter and the variation of the local paper property was performed. For example Kajanto (1989b, 1991) studied the effect of formation on print quality for woodfree offset papers by point to point comparison of paper formation and the printed surface. Thus, he studied the interrelationship between local print reflectance and local basis weight examined with β-radiography as well as local ink transfer.

Ström et al. (2010) examined the impact of local variation in coating structure on print gloss uniformity. In this study local variation of coating properties such as coating surface porosity and coating surface smoothness was measured. From image analysis of the printed samples in the region relevant for print gloss a measure for print quality was derived (i.e. coefficient of gloss variation). The following correlation of local coating properties and the coefficient of variation of print gloss led to the conclusion that nonuniformities in surface smoothness and surface porosity are the controlling factors (Ström et al., 2010; Ström and Preston, 2013).

Local print density variations have also been compared to maps of surface topography and formation (i.e. local basis weight) (Dickson, 2006; Kasajova and Gigac, 2013; Kumpulainen et al., 2011; Mettänen, 2010) as well as coating property maps (Ozaki et al., 2008; Vyörykkä et al., 2004) and surface compressibility (Mangin et al., 1994).

Hirn et al. (2008) developed a method to analyse registered 2-D paper property maps. In this approach the 2-D property maps were aligned which enabled point wise correlation of local paper properties and the printed image. Statistical analysis of registered images reveals the interrelation between the specific paper properties and their influence on print unevenness. Furthermore, image registration enabled the analysis of the effect of 3-D paper structural information (e.g. coating layer thickness) on print unevenness (Hirn et al., 2009a).

The analysis of the relationship between local paper properties and print unevenness in this thesis is based on the approach presented in Hirn et al. (2009a) and Hirn et al. (2009b).

1.3 Outline

After this introduction chapter, the present thesis is divided into the following chapters:

Chapter 2 *Measurement of Local Paper Properties* describes all the high resolution measurement methods used to analyse the paper samples regarding print unevenness. There, these methods are also compared to other relevant measurement methods.

Chapter 3 *Print Unevenness in Xerography* presents the general aspects for xerograpic printing and the research related to print unevenness. Subsequently the print tests are explained and the results of statistical modelling are discussed.

Chapter 4 *Print Unevenness in Inkjet Printing* presents the basics about inkjet printing and subsequently print unevenness in inkjet printing is discussed. Afterwards the print test on the two inkjet printers is explained and the results are discussed.

Chapter 5 *Print Unevenness in Offset Printing* exhibits a similar structure as compared to the other print unevenness chapters. The discussion is a little more detailed due to a higher amount of measured local paper properties.

Chapter 6 *Memory Effect* presents a new method for evaluation of a novel print defect and gives an overview of how much the printing machine contributes to the print unevenness.

Chapter 7 *Conclusion and Outlook* summarises the most important results and conclusions and gives a brief outlook for future work in the field of print unevenness.

1.4 List of Publications

Peer Reviewed Articles

1. Fuchs W.; Dauer M.; Hirn U.; Bauer W.; Keller D.; (2015). Fast Evaluation of Spatial Coating Layer Formation using Ultraviolet Scanner Imaging, TAPPI Journal 14(8), pages 527 – 535

2. Fuchs, W.; Dauer, M.; Hirn, U.; Bauer, W.; A Memory Effect in Sheet Fed Offset Printing. In: Advances in Printing Media and Technology IARIGAI, Vol XLII; 2015, pages 13 – 23, Helsinki, Finland.

Contribution to conference proceedings

1. Fuchs, W.; Dauer, M.; Hirn, U.; Bauer, W.; Effect of local paper properties on xerographic print mottle. In: Tokyo Paper 2015, International Paper Physics and Paper Chemistry Conference (2015), pages 97 – 97, Tokyo, Japan.

2. Fuchs, W.; Hirn, U.; Bauer, W.; Keller, D.; Fast Evaluation of Spatial Coating Layer Formation using UV Scanner Imaging. In: TAPPI Coating Conference PAPERCON 2015 Conference Proceedings, Atlanta, USA.

3. Fuchs, W.; Evaluating Time Stability of Print Mottle Patterns in Sheet Fed Offset Printing. In: Cellulose Materials Doctoral Students Summer Conference ; 2015, Grenoble, France.
4. Fuchs, W.; Hirn, U.; Bauer, W.; Keller, D. S.; Determining the Coating Layer Distribution on Paper using UV Scanner Imaging. - in: Progress in Paper Physics Seminar 2014, Raleigh, USA
5. Fuchs, W.: Investigation of Print Unevenness in Sheet Fed Offset Printing. - in: Cellulose Materials Doctoral Students Summer Conference 2014, Ebernburg, Germany.
6. Fuchs, W.; Keller, D.; Hirn, U.; Bauer, W.; The Use of an Ultra Violet Scanner for Characterization of Surface Treatments in Coated and Uncoated Papers. - in: 10. Minisymposium Verfahrenstechnik (2014), pages 37 – 42, Vienna, Austria

Invited presentations

1. Fuchs, W.: Progress in Project Print Quality. In: Print Quality Meeting OCÉ 10.11.2015. Venlo, Netherlands.

Chapter 2

Measurement of Local Paper Properties

2.1 Registration

The measurement of local paper properties and print reflectance mostly lead to two dimensional data maps. Two dimensional data maps of paper properties enable a variety of analysis methods. The analysis or evaluation of the obtained information can be divided into different groups:

Visual evaluation is the result of a subjective analysis method. Within this evaluation ranking methods are very common (Chinga et al., 2007a; Jaehn, 1990). However, visual observation is highly dependent on the perception of the evaluating persons. Thus, either a large number of experiments must be performed or the prints must be evaluated by an unchanged group of experienced professionals in order to provide reproducible results. Therefore, objective image analysis methods are preferable.

Coefficients are the result of various image analysis techniques. The coefficients mainly comprise of calculations including standard deviation and its derivations (e.g. formation index, roughness index, mottle index). These coefficients are then correlated to each other. For example Kasajova and Gigac (2013) correlated a mottle index to coefficients describing the topography of paper.

Texture analysis includes methods of second order statistics. These methods take into account the spatial separation between the data points (i.e. the pixels of the 2D data mats). Ultimately these methods are decomposing the printed image into different structure size classes and evaluate the contrast for these structure size classes. The most common ones are Fourier spectral analysis (Johansson, 1993; Sadovnikov et al., 2008; Trepanier et al., 1998), co-occurrence matrices

(Cresson and Luner, 1990; Juric et al., 2014) and wavelet analysis (Bernié et al., 2004).

Point wise correlation is the result of a point to point comparison of two or more registered (i.e. aligned) 2D data maps. There are two possible approaches to obtain registered images. First 2D data maps can be correlated if they are captured simultaneously in one measurement. For example the imaging reflectometer used by Elton and Preston (2006a) (described in Section 2.8) delivers different 2D data maps (e.g. gloss and macroroughness) which can be correlated immediately. The second approach is to register the 2D data maps and subsequently correlate it. An example of point wise correlation in a scatter plot is shown in Figure 2.1. The dashed lines indicate corresponding brighter points and the full lines indicate corresponding darker points. This registration procedure is discussed hereafter.

Registration (i.e. also called matching) enables point wise correlation of data maps not simultaneously captured. Image registration basically can be divided into different groups. On the one hand the area based registration and on the other hand the landmark based registration. The area based approach assumes that the images to be registered exhibit similar structures or textures (Petrou, 2004). The drawback of this method is that the registration fails for images with no to little similarity of the structures. The second approach based on landmarks, uses distinctive structures present in each image to be registered (i.e. landmarks). A possible landmark is an adhesive tape with a rectangular shape in order to define a coordinate system as described by Hirn et al. (2008). Another landmark is a hole introduced into the sample e.g. (Hirn et al., 2009a; Kajanto, 1989b; Pawlak and Keller, 2004).

The image registration method applied in this thesis was based on the landmark approach. The landmarks in this case were laser holes introduced by a CO_2 laser as described by Hirn et al. (2009a). In Figure 2.2 a basis weight map of an office paper grade ($80\,g/m^2$) is depicted. Brighter regions represent areas of higher local grammage and darker regions represent lower local grammage. The laser holes can be identified as black spots on the edge of the image.

For image registration a target image in an x,y coordinate system was defined. With help of the laser marks which were visible on all obtained 2D data maps, source images with coordinates x′, y′ were introduced (Figure 2.3). All source images were mapped to the target image which was unrotated and had its origin at $x = 0$ and $y = 0$ (i.e. left upper corner). This is achieved by mapping the target pixel coordinates x, y to the source pixel coordinates x′, y′ and extracting the image data from the source images. The pixel coordinates are defined by the translation vector **t**, the scale parameter s and the rotation matrix **r** with the rotation angle ϕ according Equation 2.1.

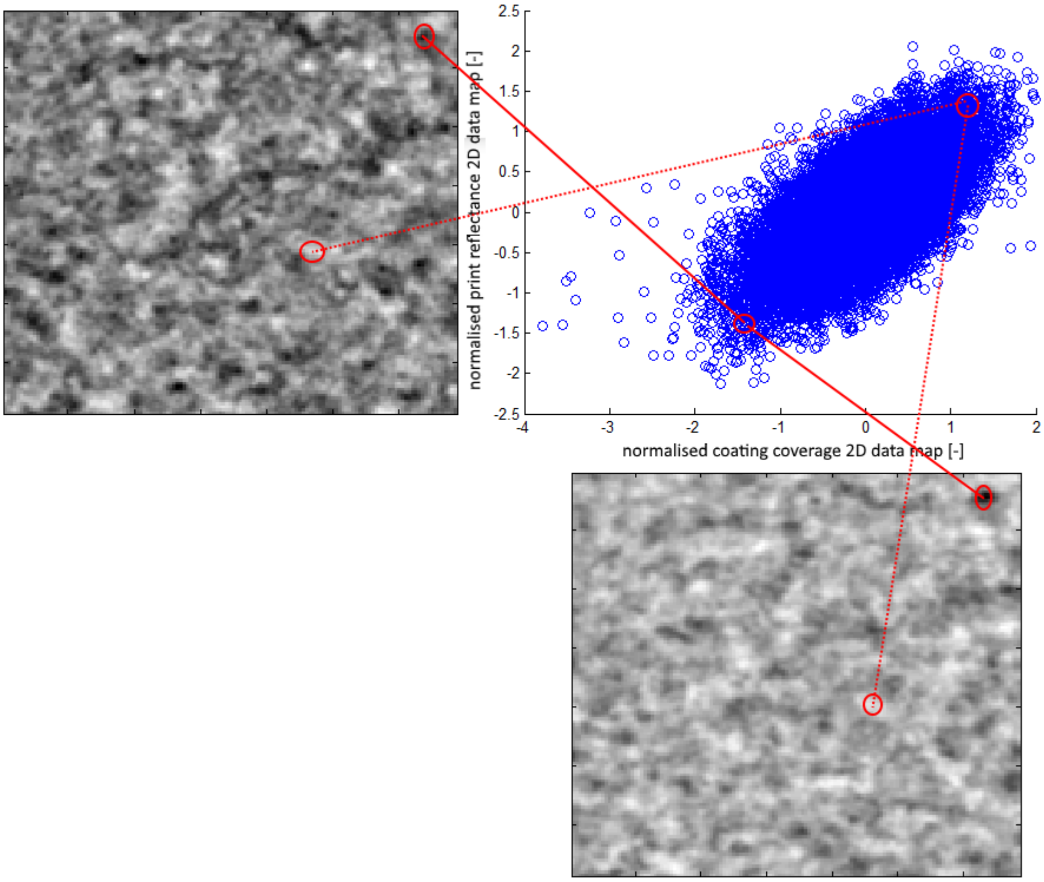

Figure 2.1 Point wise correlation of two 2D data maps (i.e. images obtained from the measurement device). The upper left image represents the contrast enhanced filtered image of print reflectance and bottom right image represents the filtered and contrast enhanced image of coating coverage obtained with UV LED. The dotted lines indicate corresponding brighter points (i.e. same coordinates in the image) and the full lines indicate corresponding darker points. (size of images 35 mm × 35 mm).

The scale parameter $s = \frac{p_t}{p_s}$ enables rescaling of the source pixel size p_s to a desired target pixel size p_t (Hirn et al., 2008; Petrou, 2004).

$$\begin{pmatrix} x' \\ y' \end{pmatrix} = \mathbf{t} + s \cdot \begin{pmatrix} x \\ y \end{pmatrix} \cdot \mathbf{r} = \begin{pmatrix} t_x \\ t_y \end{pmatrix} + s \cdot \begin{pmatrix} \cos\phi & \sin\phi \\ -\sin\phi & \cos\phi \end{pmatrix} \cdot \begin{pmatrix} x \\ y \end{pmatrix} \tag{2.1}$$

The evaluation of the image registration method with respect to local paper properties and print unevenness was performed by point wise correlation of the registration of one and the same sample with different target pixel sizes. It was found that the registration error is 1 % when an image with a source pixel size of 21 µm is registered

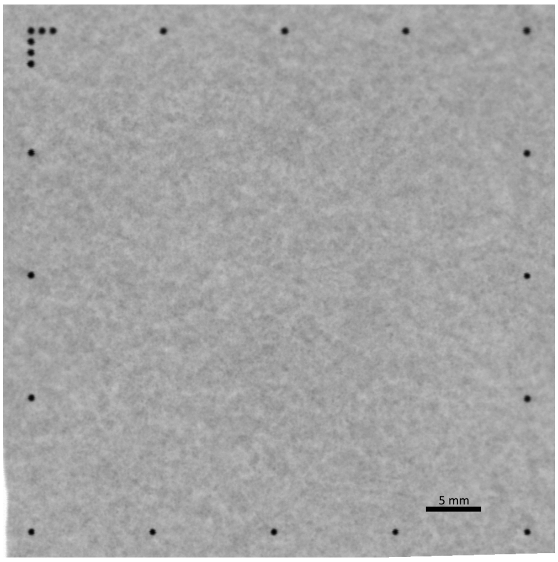

Figure 2.2 Basis weight map (office paper grade 80 g/m^2) with laser marks (i.e. black holes).

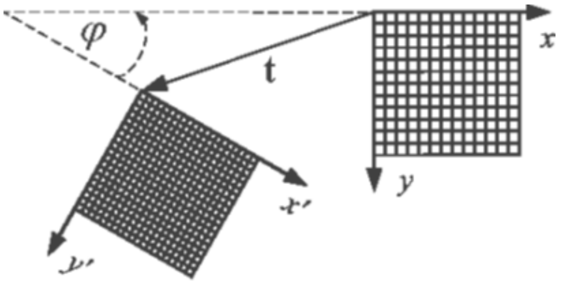

Figure 2.3 Principle of image registration, which is a shape preserving coordinate transform or similarity transform Hirn et al. (2008).

to a target pixel size of 254 µm (Hirn et al., 2008). The subsequent analysis of the registered and thus aligned images is described in Section 2.2.

After registration, the images were descreened by means of a FFT filter and then post processed in two ways. On the one hand, spectral filtering (i.e. a FFT pass band filter) was performed in the wavelength band of 2 mm to 8 mm. The reason for spectral filtering is that the human eye visually perceives non-uniformities differently at different length scales. The region of interest for visual perception of print mottle according to Johansson is located in the wavelength band of 2 mm to 8 mm (Johansson, 1993). This type of filtering produces images where only the structures most relevant for print mottle are preserved.

On the other hand, the images were rescaled to a pixel size of 250 µm. That is the size of structures, which the human eye can resolve under good illumination at a viewing distance of 30 cm (Olzak and Thomas, 1986). Hence, at a pixel size of 250 µm all structures perceived by the human eye are preserved.

2.2 Multiple Linear Regression Analysis

This chapter mainly follows the presentation of regression analysis in (Neter et al., 1996). The analysis of the obtained data in this thesis was based on the hypothesis that the print reflectance depends to a certain extent on the various measured local paper properties. From the statistical point of view this is problem of multivariate data analysis. Backhaus et al. (2003) described common methods to analyse multivariate data such as linear regression, principal component analysis or cluster analysis. For the analysis of the present data, linear regression was the method of choice.

Regression analysis is one of the most widely used of all statistical methods. Its use is to analyse the relationship between one dependent variable and one or more independent variables. Presently, the local print reflectance is ought to be the depend variable and the local paper properties are the independent variables. The aim of regression analysis is to describe and explain this relationship quantitatively (Backhaus et al., 2003). The most facile one is the simple linear regression. Simple, because there is only one predictor variable and linear, because no parameter appears as an exponent or is divided or multiplied by another parameter. An example of simple linear regression can be seen in Figure 2.1. The scatter plot shows the print reflectance (y axis, predictor variable) in dependence of the coating coverage (x axis, independent variable). The pixel size of the images is 250 µm and the size of the images is 35 mm, thus, the scatter plot is built of 19600 data points. The simple linear regression model for this example can be stated as follows (Neter et al., 1996):

$$Y_i = \beta_0 + \beta_1 X_i + \varepsilon_i \tag{2.2}$$

where

Y_i is the value of the response variable of the ith data point,

X_i are known constants (i.e. the values of the predictor variable in the ith data point),

β_0, β_1 are parameters (e.g. the coefficient of the underlying parameter of the model),

ε_i is a random error term with mean $E\{\varepsilon\} = 0$

i = 1,. . . , n (i.e. the index of the data point).

The response of Y_i in the ith data point is the sum of two components, the first constant term $\beta_0 + \beta_1 X_i$ and the second random term ε_i. Thus, Y_i is a random variable. Since $E\{\varepsilon\} = 0$ and the response Y_i comes from a probability distribution whose mean is

$$E\{Y_i\} = \beta_0 + \beta_1 X_i \tag{2.3}$$

where $E\{Y_i\}$ is the expectation or expected value of Y_i, the regression function for the model in Equation 2.2 becomes

$$E\{Y\} = \beta_0 + \beta_1 X \tag{2.4}$$

In order to estimate the parameters β_0, β_1 of the regression function, the experimental or observational data is used (i.e. print reflectance – and coating coverage data map). For each data point, there is a X observation and Y observation. Since the data map consists of 19600 data points, there are 19600 observations. For this model, $i = 1, \ldots, n$ becomes $i = 1, \ldots, 19600$.

The standard model to estimate the regression parameters β_0, β_1 is the so called method of least squares. According to the method of least squares, the estimators β_0, β_1 are those values b_0, b_1 that minimise the criterion Q for the given sample observations (Y_1, X_1), (Y_2, X_2) $\ldots$ (Y_{19600}, X_{19600}):

$$Q = \sum_{i=1}^{n} (Y_i - \beta_0 - \beta_1 X_i)^2 \tag{2.5}$$

Given the sample estimators b_0 and $_1$ of the parameters β_0 and β_1 in the regression function (Eq. 2.4), the regression function can be estimated as follows:

$$\widehat{Y} = b_0 + b_1 X \tag{2.6}$$

where $\widehat{Y}$ is the value of the estimated regression function at the level X of the predictor variable. Thus, $\widehat{Y}_i$ is the fitted value for ith data point in distinction to Y_i, the observed value:

$$\widehat{Y}_i = b_0 + b_1 X_i \tag{2.7}$$

In case of the present data from Figure 2.1, the estimated regression function is:

$$\widehat{Y} = 0.02 + 0.60X \tag{2.8}$$

Since there are more than one explaining variables examined within this thesis, the case of multiple linear regression is discussed here. The model of multiple linear regression can be stated as follows (Neter et al., 1996):

$$Y_i = \beta_0 + \sum_{k=1}^{p} \beta_k X_{ik} + \varepsilon_i = \beta_0 + \beta_1 X_{i1} + \beta_2 X_{i2} + \beta_3 X_{i3} + \ldots + \beta_p X_{ip} + \varepsilon_i \tag{2.9}$$

where

Y_i is the value of the response variable of the ith data point,

$X_{i1}, \ldots, X_{ik}$ are known constants (i.e. the values of the predictor variables in the ith data point),

$\beta_0, \ldots, \beta_p$ are parameters (e.g. the coefficient of the underlying parameter of the model),

ε_i is a random error term with mean $E\{\varepsilon\} = 0$

i = 1,. . . ,n (i.e. index of the data point)

k = 1,. . . ,p (i.e. index of predictor).

The response function of the assumed regression model (Eq. 2.9) becomes then:

$$E\{Y_i\} = \beta_0 + \sum_{k=1}^{p} \beta_k X_{ik} = \beta_0 + \beta_1 X_{i1} + \beta_2 X_{i2} + \ldots + \beta_p X_{ip} \tag{2.10}$$

and the estimated regression function:

$$\widehat{Y}_i = b_0 + \sum_{k=1}^{p} b_k X_{ik} = b_0 + b_1 X_{i1} + b_2 X_{i2} + \ldots + b_p X_{ip} \tag{2.11}$$

Again, the parameter b_k in the estimated regression function in Equation 2.11 is determined by the so called least square criterion and indicates the change in $\widehat{Y}_i$ with a unit increase in the predictor X_{ik}, when all other predictor variables in the regression model are held constant (Neter et al., 1996). This means that the change of $\widehat{Y}_i$ can be qualitatively interpreted. For example a b_k exhibiting a positive sign indicates that $\widehat{Y}_i$ increases with increasing X_{ik} and vice versa.

The quantitative interpretation of the multiple linear regression model is delivered by the analysis of variance (i.e. ANOVA). The measure of the total variation of the regression is given by Equation 2.13. It is the sum of the squared deviations (i.e. SSTO) where $\overline{Y}$ is the mean value of Y_i data points. The total sum of squared variation consists of the variance explained by the model (sum of squares regression: SSR) described by Equation 2.14 and the variance not explained by the model (sum of squares error: SSE, i.e. the random error term in Eq. 2.9) described by Equation 2.15. In Figure 2.4 the sum of squares are visualised.

$$SSTO = SSR + SSE \tag{2.12}$$

$$SSTO = \sum (Y_i - \overline{Y})^2 \tag{2.13}$$

$$SSR = \sum (\widehat{Y}_i - \overline{Y})^2 \tag{2.14}$$

$$SSE = \sum (Y_i - \widehat{Y}_i)^2 \tag{2.15}$$

The quantitative measure for the strength of the model is the so called coefficient of determination (R^2). R^2 is defined as the proportion of the reduction in variation ($SSTO - SSE = SSR$) to the total variation $SSTO$ (see Equation 2.16). Thus, R^2 measures how much of the variation in the data can be explained by the regression

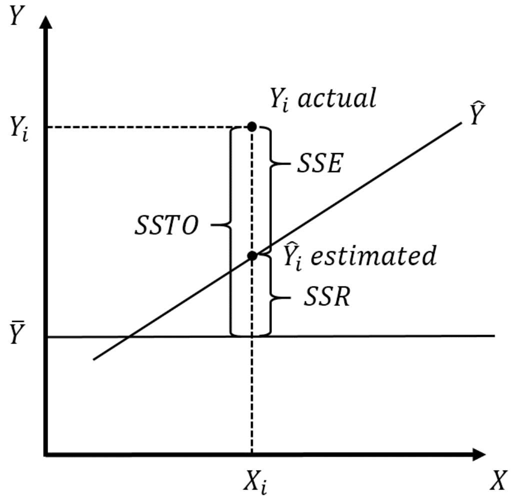

Figure 2.4 Visualisation of SSTO, SSR and SSE.

model. A R^2 value of 1 indicates that there is a perfect linear relationship between the dependent and independent variables and thus, the model can fully predict the data. Whereas a R^2 value of 0 is evidence for no linear relationship (Backhaus et al., 2003).

$$R^2 = \frac{SSR}{SSTO} = 1 - \frac{SSE}{SSTO} \tag{2.16}$$

With help of Equation 2.16 one can quantify how much of variation of the data can be explained by one measured predictor (i.e. single linear regression model) or by all measured predictors (multiple linear regression model) together. Another point of interest is the quantification of how much one predictor contributes to the whole multiple linear regression model. This is information is obtained by the so called extra sum of squares which decomposes the coefficient of determination of the whole model into coefficients of partial determination (COPD). The COPD, like R^2, explains a part of the total variation $SSTO$ in the data. In comparison to R^2, the COPD particularly explains the increase of R^2 if a new predictor is added to the model (Backhaus et al., 2003). Figure 2.5 depicts an exemplary result plot illustrating the components of the multiple linear regression model. The *total* r^2 is the R^2 calculated from the whole regression model as described by Equation 2.11. The r^2_{alone} is the R^2 calculated from a single linear regression model, which means no other predictors are in the model (i.e. single linear regression model in Eq. 2.2). The $r^2_{exclusive}$ is calculated from the COPD. Thus, $r^2_{exclusive}$ shows the increase of R^2 if this predictor is added to the model at last. In accordance, $r^2_{redundant}$ shows how much of the information contributed by this predictor is also contained in other predictors. Thus, by calculating $r^2_{exclusive}$ and $r^2_{redundant}$ a decision criteria whether a predictor is valuable or not is available.

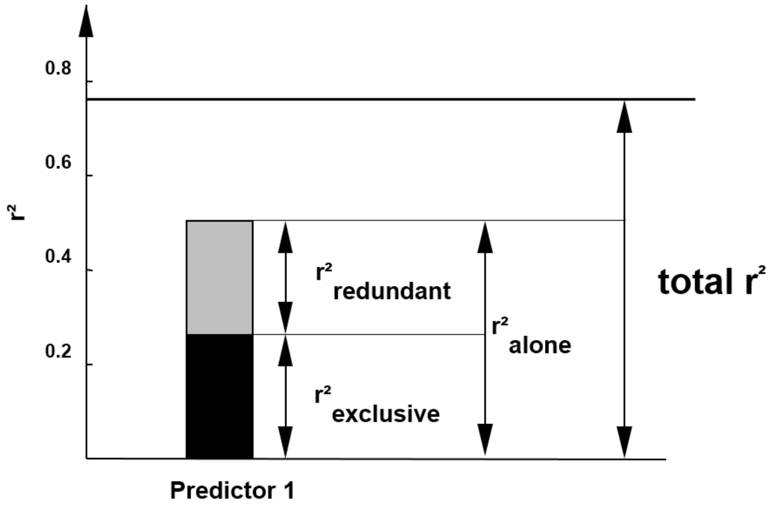

Figure 2.5 Illustration of the difference between the coefficient of partial determination ($r^2_{exclusive}$), the r^2 of the whole multiple linear regression model (*total* r^2) and the single linear regression model r^2_{alone} in an example result plot used in this thesis.

The mathematical in depth description of the development of this approach are discussed can be found in Hirn et al. (2009b) and Lechthaler (2007) and the background of the concept of the extra sum of squares and the coefficient of partial determination is described in Backhaus et al. (2003).

In Figure 2.6 a complete exemplary result plot is shown with seven predictors. In comparison to the result plot in Figure 2.5 additionally the coefficients of the predictors $b_1 - b_7$ are included as error bars with 95 % confidence limits (see second y-axis). A b of one predictor exhibiting a positive sign indicates that the predictor and the target are positively correlated (e.g. predictor 1, 4 and 6) and vice versa. When the error bar crosses the zero line it is not clear whether the correlation is positive or negative, thus the predictor is not valid. This is the case for predictor 3 and 5. The recommendation is then to dismiss these predictors and to repeat the regression analysis without those predictors. Figure 2.6 also illustrates a high redundancy of the predictors (i.e. light grey amount of the bars), thus the predictors itself are highly correlated. Only predictor 1 and 6 exhibit a reasonable $r^2_{exclusive}$. The conclusion for this plot is that only predictors 1 and 6 provide statistically significant (b does not cross zero line) and non redundant ($r^2_{exclusive}$ is considerable larger than zero) information; all other variables are not relevant.

This type of result plot was used to examine the relationship between print unevenness and the local paper properties within this thesis. Furthermore, small adjustments of the result plot are explained in the chapters affected.

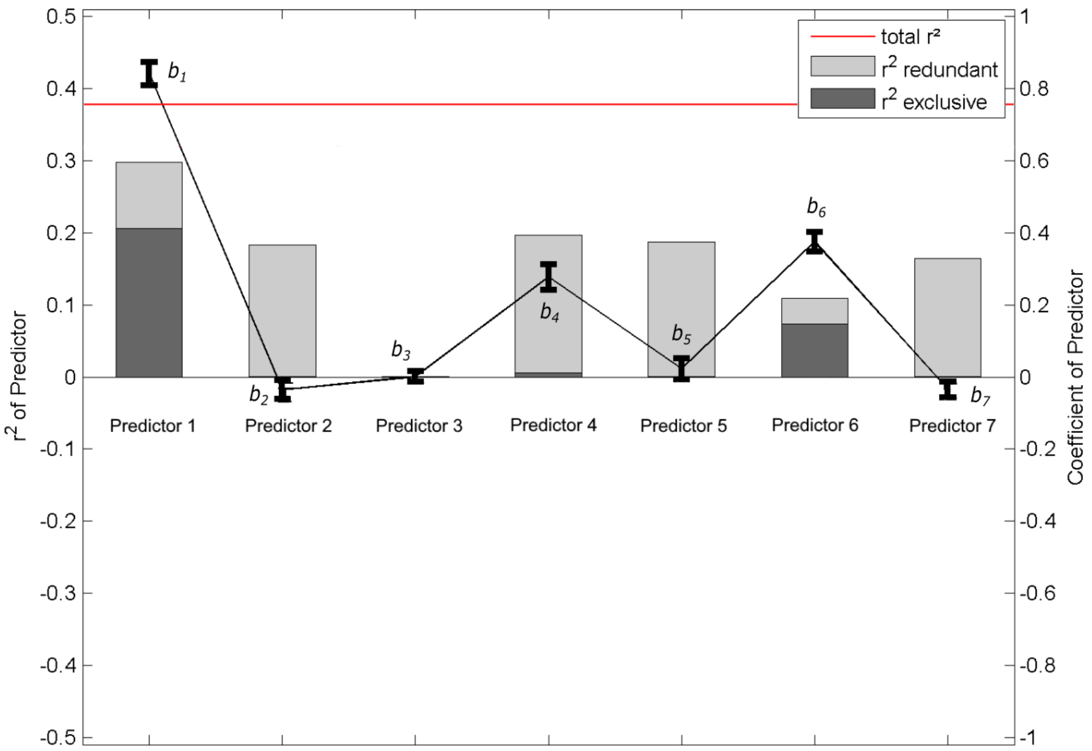

Figure 2.6 Exemplary result plot with seven predictors.

2.3 Topography Measurement

2.3.1 Infinite Focus Variation

The topography of paper can be measured either with mechanical or optical instruments. The optical instruments can be further divided in scanning optical and areal optical techniques. Focus variation belongs to the areal optical techniques. It combines vertical scanning with the small depth of focus of optical systems to gain topographical information from the variation of focus. Figure 2.7 shows the schematic drawing of a measurement device based on focus variation.

The main component of the measurement system is an optical microscope with interchangeable objective lenses. Mounting of different objectives (Nr. 5 in Fig. 2.7) enables measurements with different lateral resolution. In order to capture the surface with full depth of field, the optical arrangement moves vertically along the optical axis while continuously capturing surface data. Implemented algorithms convert the obtained sensor data into 3-D information as well as a true colour image with full depth of field. Two of the requirements for a successful focus variation measurement are that the examined specimen must not be transparent and the arithmetic average of roughness $R_a > 10\,\text{nm}$ at a cut off wavelength of 10 µm (Leach, 2010, Chapter 6).

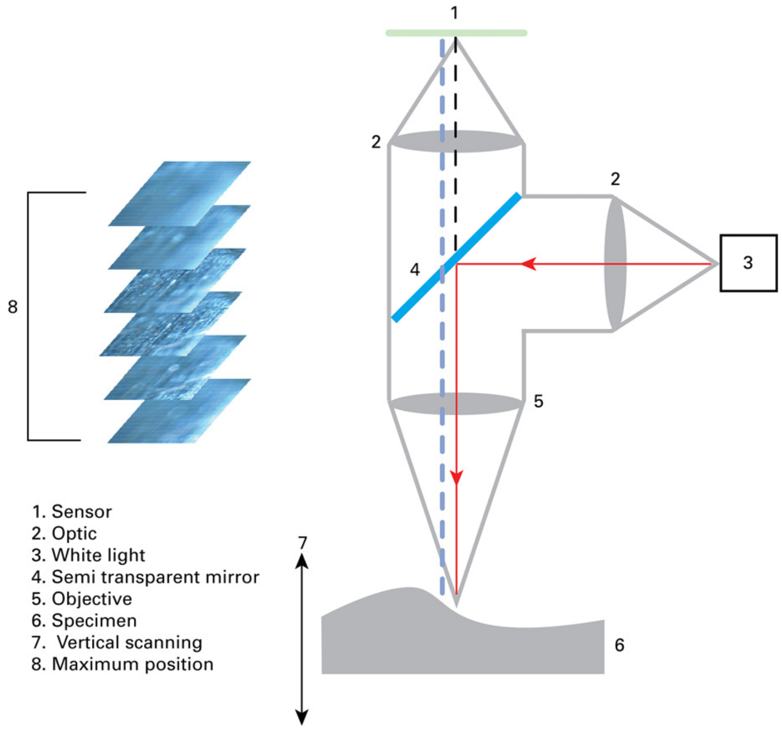

Figure 2.7 Schematic drawing of measurement principle based on focus variation (Leach, 2010, Chapter 6).

The infinite focus variation measurement device ALICONA INFINITE FOCUS G3 INSTRUMENT (abbrev. IFM) utilised for the topography measurements in this thesis was developed by Alicona (Alicona Imaging GmbH, Grambach, Austria). Its primary use was to perform roughness, form and wear measurements of tools (Danzl et al., 2011). In the field of topographical measurements of paper the IFM has been evaluated by Wind (2011) and compared to other stylus (Lechthaler and Bauer, 2006) and optical topography measurement techniques (Mettänen and Hirn, 2015).

The obtained IFM images had a pixel size of 3.18 µm/pixel for the evaluation in Lechthaler and Bauer (2006) and 6.4 µm/pixel in Mettänen and Hirn (2015) and was varied from 3.18 µm/pixel to 12.8 µm/pixel in Wind (2011). In conclusion a convenient solution was to examine the topography of large area samples (e.g. 35 mm × 35 mm) at a pixel size of 12.8 µm/pixel.

As mentioned before, roughness is an important factor for reliable results of the IFM. There is no conversion between arithmetic average of roughness R_a and PPS roughness available, but the deductions were similar: the rougher the surface the better the reproducibility of the results. For rough paper grades such as lightweight coated paper and office paper (PPS roughness >0.7 µm), the topography information obtained from optical topography measurement was coherent. For smoother paper grades, however, the topography information yielded, differed from the measurement technique applied. Furthermore, cellulose fibres are transparent which might explain part of the divergent results. In addition, a factor not mentioned in the studies is the vertical resolution of the IFM. A too low vertical resolution might negatively influence the calculation of the topography information due to less vertical scanning steps.

The IFM settings for measurement of local topography of the samples for modelling local print unevenness in this thesis were the same for all samples. The pixel size chosen was 12.8 µm/pixel (5x magnification objectiv) and the vertical resolution was set to 800 nm. The only difference between the specific paper samples was the exposure time. This is due to the fact that the different paper samples did not exhibit the same brightness.

Subsequently the IFM internally calculated the whole topography map. Due to IFM inherent software issues the obtained topography maps had to be post processed. The maps exhibited a certain curvature and in order to get rid of it, the images were highpass filtered with a cut off wavelength of 20 mm.

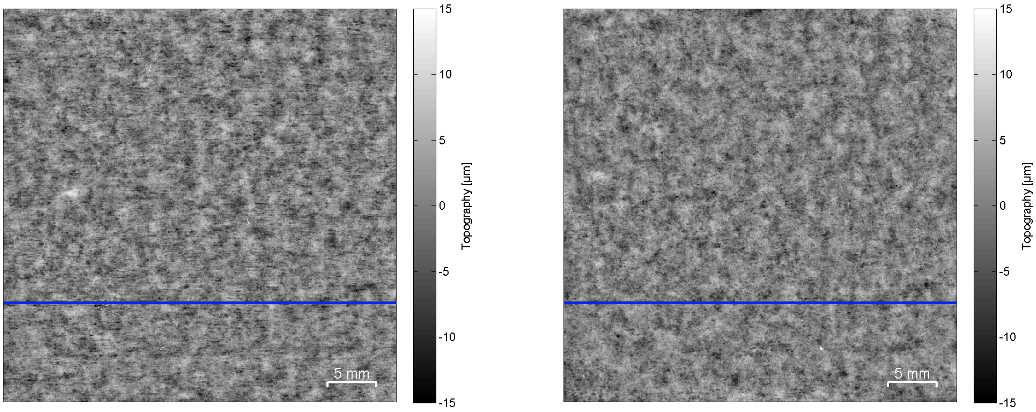

(a) Topside.

(b) Bottomside.

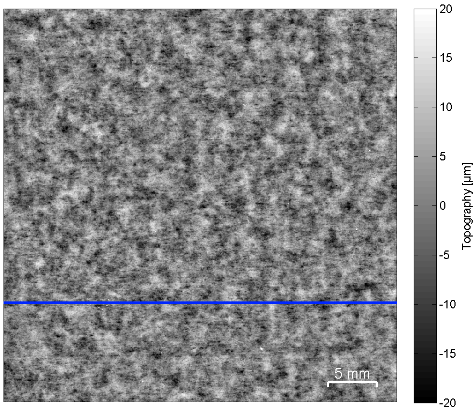

(c) Thickness variation.

Figure 2.8 Registered topography maps of **(a)** topside and **(b)** bottomside of the same sample. **(c)** shows the thickness variation calculated out of **(a)** and **(b)** (office paper grade 80 g/m^2). Visualisation of blue line data is given in Figure 2.9.

2.3.2 Thickness Variation

For local thickness variation different measurement techniques are available. On the one hand, thickness variation can measured with a stylus apparatus as used in Wink and Baum (1983) and in Schultz-Eklund et al. (1992). On the other hand, thickness variation can be measured with a pair of noncontact laser triangulation sensors as used in Pawlak and Keller (2004).

The approach in this thesis differed from the mentioned measurement techniques. Local thickness variation was calculated of local topography maps. First the topography of the topside of the sample (see Fig. 2.8a) and secondly the topography of the bottomside of the sample (see Fig. 2.8b) was measured. After registration and align-

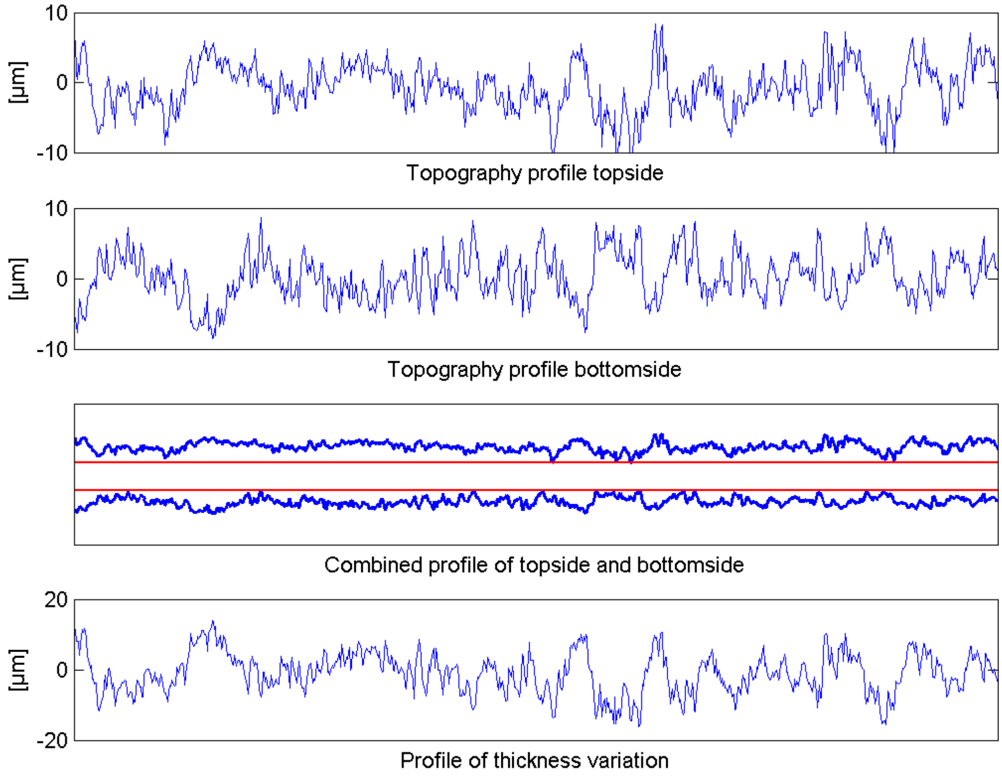

Topography profile topside

Topography profile bottomside

Combined profile of topside and bottomside

Profile of thickness variation

Figure 2.9 Exemplary z-profiles extracted from the blue lines in images in Figure 2.8. Top down: topside, inverted bottomside, the combined profile of top- and bottomside (the real sample thickness is indicated by the distance between the red lines) and thickness variation.

ment of the topography maps (see Section 2.1) the thickness variation was calculated by adding up the top- and the bottomside of the topography map. The bottomside of the topography map is the topography measured from the backside of the sample:

$$\begin{aligned}
Thickness\quad Variation &= Topo\quad Topside \quad - \quad Topo\quad Bottomside \\
Topo\quad Bottomside &= -(Topo\quad Bottomside\quad up) \\
Thickness\quad Variation &= Topo\quad Topside - (-(Topo\quad Bottomside\quad up)) \\
Thickness\quad Variation &= Topo\quad Topside \quad + \quad Topo\quad Bottomside\quad up
\end{aligned}$$

Figure 2.8c shows the result of the calculation of the thickness variation for an office paper grade (80 $\mathrm{g/m^2}$). Figure 2.9 depicts the profile of the top- and inverted bottomside topography as well as the combined profile of top and bottom and the profile of the thickness variation exemplary taken from the images in Figure 2.8a and 2.8b (blue lines). It is apparent from Figure 2.9 that the real sheet thickness can not be calculated by this method because the distance between the two red lines in the combined profile is unknown. However, the relevant information (i.e. local thickness variation) is captured by this method.

2.4 Brightness and Opacity

Traditional methods such as those for **brightness**, **Y-value** and **opacity** are usually measured according to standardised measurement methods. **Brightness** (ISO:2470, 2008) is calculated by summing a set of weighted spectral reflectance values which are obtained as the product of the spectral reflectance values and tabulated spectral values of the brightness function over a limited wavelength range from 400 nm to 510 nm. The effective wavelength of brightness function is 457 nm (Pauler, 2012). For brightness examination there are three standards available:

- ISO Brightness (ISO:24701, 2009)
- D65 Brightness (ISO:24702, 2008)
- Non-fluorescence brightness (ISO:24701, 2009)

The second standard measure is the **Y-value**. The Y-value is one of the three tristimulus values X (red), Y (green) and Z (blue). This three values describe the function of the human eye with respect to colour with its relative sensitivities of the three types of cone cells (Hubbe et al., 2008). In 1931, CIE (Commission Internationale de l'Eclairage) adopted a system for colorimetry, which is based on the Young & Helmholtz three colour theory. Within this CIE system certain colour matching functions were standardised based on the sensitivity of the average human eye in various wavelength regions. Therefore, the CIE system defines the X, Y and Z values. This means that each perceived colour can be described with the tristimulus values (Pauler, 2012). For colour measurements, there are three different combinations of illuminant and colour matching functions standardised according to ISO (ISO:5631, 2008).

- ISO 5631-1 Determination of colour with illuminant C (daylight) at 2° observer angle (C/2°)
- ISO 5631-2 Determination of colour with illuminant D65 (daylight with little higher UV amount) at 2° observer angle (D65/10°)
- ISO 5631-3 Determination of colour with illuminant D50 (daylight with little higher UV amount) at 2° observer angle (D50/2°)

The third standard measure for characterisation of optical properties for paper is **opacity**. Opacity is related to be the degree of non transparency of a specimen. It is calculated as the ratio of the reflectance factor of a single sheet over a black background (R_0) to the reflectivity (R_∞) (see Eq. 2.17). The reflectance values R_∞ and R_0

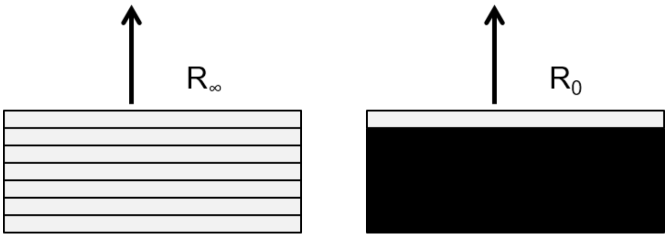

Figure 2.10 Schematic description of the measurement of the reflectance values R_∞ and R_0.

are the Y-values measured with illuminant C at 2° observer angle (C/2°). Thus, determination of opacity is analogue to the determination of the Y-value. Experimentally it has to be ensured that R_∞ is measured over a sufficiently thick opaque stack of paper (Pauler, 2012). When using Equation 2.17 it is apparent from Figure 2.10 that paper grades of lower grammage exhibit a lower R_0 and thus, have a lower opacity.

$$Opacity = 100 \times \frac{R_0}{R_\infty} \tag{2.17}$$

In order to better understand the optical properties such as **brightness**, **Y-value** and **opacity** the Kubelka Munk theory is usually utilized. The two key factors in the Kubelka Munk theory are light scattering (s) and the light absorption (k) (Kubelka and Munk, 1931). These two parameters are of fundamental importance in numerous processes involved during paper manufacturing. Bleaching for example decreases light absorption. Refining and addition of certain types of fillers increases light scattering because of the creation of new surfaces.

The Kubelka Munk equations are derived for a sheet placed over a sufficiently thick background with the reflectance factor R_g. Several assumptions were made in the derivation of the equations (Pauler, 2012):

- No surface phenomena at the interface between the sheet and air (e.g. scattering).
- Illumination of the sheet is perfectly diffuse with monochromatic light.
- The sheet is isotropic with regard to scattering and absorption.
- Light scattering and light absorption are homogeneously distributed within the sheet.

According to the derivation by Kubelka and Munk, the beam or stream of light travelling downwards is defined as $\mathrm{i}(x)$ and the one travelling upwards is defined as $\mathrm{j}(x)$. The change in the intensity of an incident light beam that is passing through a layer $\mathrm{d}x$ in the paper is then defined as -di and the change of the intensity of the

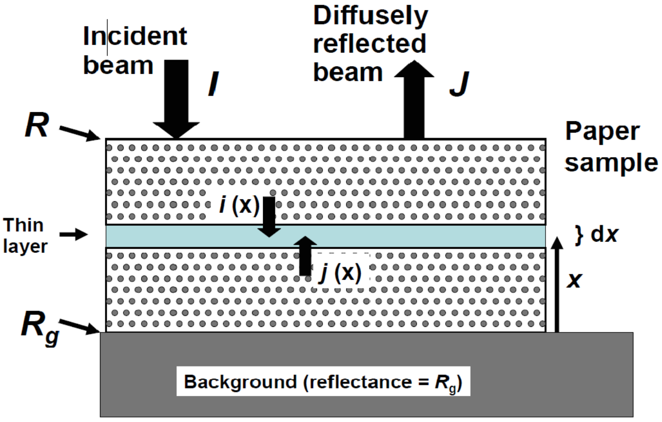

Figure 2.11 Basic model for the derivation of the Kubelka Munk equations (Hubbe et al., 2008).

beam that is travelling upwards through a layer dx is defined as -dj. For a thin layer examined (dx) the change can be expressed by Equation 2.18 and 2.19. Figure 2.11 illustrates the basic principle of the Kubelka Munk derivations.

$$-\,\mathrm{d}i = -(s+k)i\mathrm{d}x + sj\mathrm{d}x \tag{2.18}$$

$$\mathrm{d}j = -(s+k)j\mathrm{d}x + si\mathrm{d}x \tag{2.19}$$

The measurement of local opacity differs from the above explained standards. In this thesis the ALICONA INFINITE FOCUS G3 INSTRUMENT (IFM) was used in the imaging mode to obtain local opacity maps of the paper samples. The pixel size chosen was 25.6 µm/pixel. In order to fulfil the requirement of diffuse illumination, a LED dome light was mounted on the objective of the IFM (see Fig. 2.12a). For calculation of opacity the green channel of the CMOS camera of the IFM was used, because the green channel acts similar to the matching function of the Y value. The method was evaluated in an internal report by Hirn (2010). Figure 2.12b shows the measurements necessary to calculate local opacity. First the reflectance of the white R_{gw} and black R_{gb} reference samples is measured. Subsequently the reflectance of the examined sample is measured over the black R_b and the white R_w reference paper. Equation 2.20 and 2.21 show a possible way to calculate R_∞ of different reflectance values measured over two reference samples provided by Kubelka Munk. Furthermore, it is possible to calculate the values s and k for light scattering and light absorption according to derivations from Equation 2.20 and 2.21 (Pauler, 2012).

Within this thesis R_b and R_w was locally measured for one and the same sample. After registration of the reflectance maps, local opacity was calculated for each point according to Equations 2.17, 2.20 and 2.21, where $R_0 \sim R_b$ in Equation 2.17. Local

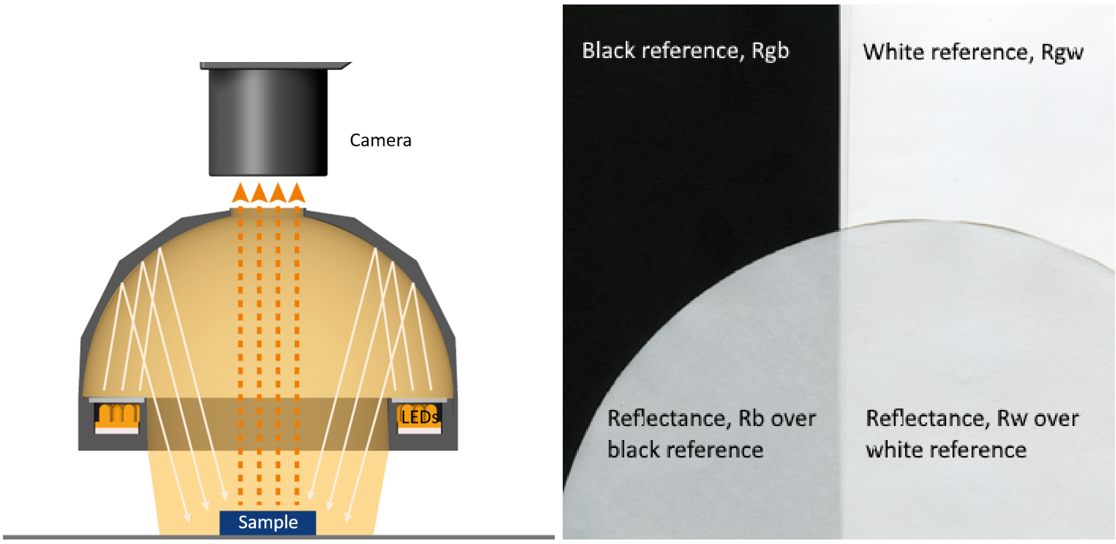

(a) LED dome. **(b)** Reflectance measurements.

Figure 2.12 **(a)** Schematic illustration of the principle of diffuse illumination with a LED dome (adapted from www.iimag.eu) and **(b)** example of the necessary reflectance measurements for calculating R_∞ (Hirn, 2010).

opacity was only calculated for uncoated paper samples, because this kind of Kubelka Munk equations are not valid for layered structures.

$$a = \frac{1}{2} \times \frac{(R_{gw} - R_{gb})(1 + R_w R_b) - (R_w - R_b)(1 + R_{gw} R_{gb})}{R_b R_{gw} - R_w R_{gb}} \tag{2.20}$$

$$R_\infty = a - \sqrt{a^2 - 1} \tag{2.21}$$

2.5 Wetting Phenomenon and Ink Penetration

When printing ink is brought into contact with the paper, the ink distributes laterally and vertically. Figure 2.13 illustrates the behaviour of a water based inkjet droplet on a surface of an uncoated substrate such as an office paper grade. The first interaction is the release of the kinetic energy of the droplet, it causes a mechanical spreading. In the second phase capillary spreading occurs, which is caused by the capillary structure of the paper. At that point, the ink moves in both directions, vertically and laterally. Vertical spreading of the droplet is called penetration (Oittinen and Saarelma, 2009).

The wetting phenomenon is ideally described by the Young equation (Eq. 2.22),

$$\cos \Theta \cdot \gamma_{lv} = \gamma_{sv} - \gamma_{sl} - \pi_e \tag{2.22}$$

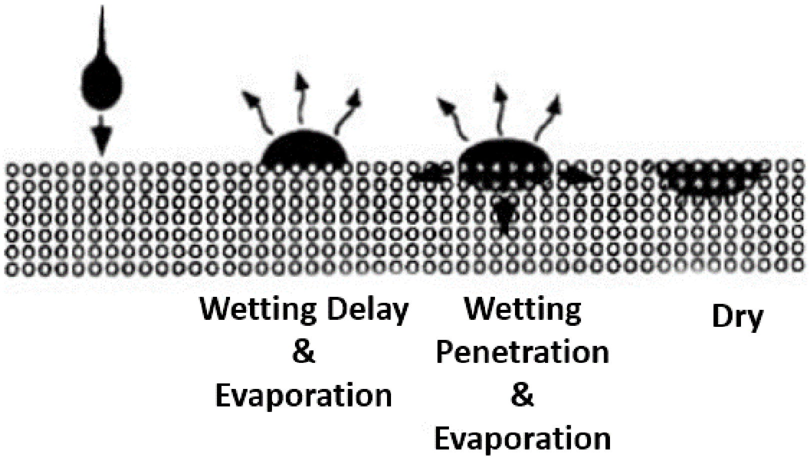

Figure 2.13 Drying mechanisms of a water based inkjet drop on a plain paper (Le, 1998).

where γ_{lv}, γ_{sv} and γ_{sl} are the free energies of the liquid and solid against their saturated vapour and of the interface between liquid and solid, respectively. π_e is the equilibrium pressure of adsorbed vapour of the liquid on the solid, also called spreading pressure (Owens and Wendt, 1969). π_e is usually very small and often neglected. Θ is the contact angle between the liquid and the solid surface.

Furthermore, the Young-Laplace equation (Eq. 2.23) describes the capillary pressure of a liquid capillaries,

$$p_c = h\rho g = \frac{-2\cos\Theta\gamma_{lv}}{r} \tag{2.23}$$

where p_c is the Laplace pressure, h is the height to which the liquid rises in equilibrium state, ρ is the liquid density, g is the acceleration due to gravity and r the internal capillary radius. During liquid motion, the Young-Laplace pressure pushes (for $\Theta < 90°$) the liquid into the pore against the viscous Poiseuille drag force, expressed by

$$\frac{dV}{dt} = \frac{\pi r^4}{8\eta l}\Delta p \tag{2.24}$$

where $\frac{dV}{dt}$ is the volume flow rate of a liquid of viscosity η (i.e. dynamic viscosity $[Pas]$) through the effective capillary of radius r and length l under the driving pressure difference Δp, which is in this case the Laplace pressure defined by Equation 2.23 (Kettle et al., 2010). The so called Poiseuille flow assumes laminar flow in the tube (i.e. a parabolic veclocity distribution).

Moreover, the most common equation to describe the rate uptake of liquid into a porous system was introduced by Washburn (1921) and Lucas (1918). By combining the Young-Laplace equation (Eq.2.23) with Poiseuille's equation (Eq. 2.24), they obtained the following expression:

$$x^2 = \frac{rt\cos\Theta\gamma_{lv}}{2\eta} \tag{2.25}$$

where x is the distance the liquid front travels in time t and r is the effective hydraulic radius (i.e. the pore radius in the ideal case of cylindrical pores). According to Lucas-Washburn the volume of liquid in a capillary should increase with the radius at a given time. However, various authors observed, that smaller radius capillaries initially fill faster than larger ones (Kettle et al., 2010; Lundberg et al., 2011; Schoelkopf et al., 2002). This disagrees with Lucas-Washburn. Schoelkopf et al. (2002) mentioned, that the main draw back of the Lucas-Washburn approach is the disregard of the inertial flow. Therefore, another approach was taken into account – the Bosanquet equation. The Bosanquet equation takes into account the initial acceleration of the fluid (Kettle et al., 2010; Ridgway et al., 2002; Schoelkopf et al., 2000). During the initial flow regimen the fluid accerates until stationary laminar flow is achieved, this is called inertial flow and follows Equation 2.26. According to the inertial flow, the ink penetration is stronger for smaller pores. For a detailed discussion on the different flow regimes and the transition between initial flow and Lucas-Washburn flow please refer to Schoelkopf (2002) .

$$x = t\sqrt{\frac{2\gamma_{lv}\cos\Theta}{r\rho}} \tag{2.26}$$

The wetting phenomenon is usually assessed by contact angle measurements (Lundberg et al., 2011; Oko et al., 2011; Pykönen and Aura, 2012). However, local mapping of contact angle measurements were not reported so far.

In order to study ink penetration, a variety of microscopy techniques have been utilized. Cross sections of printed samples have been examined via SEM (scanning electron microscopy) (Eriksen and Gregersen, 2005; Yang et al., 2011) as well as with optical microscopy (Kappel et al., 2008; Lundberg et al., 2011; Yang et al., 2005). Vyörykkä et al. (2004) studied surface ink density with confocal Raman microscopy.

On the other hand, there are alternative approaches to assess ink penetration. Most often the negative and unwanted result (i.e. print through) of ink penetration is evaluated. Print through (PT) is a major effect of ink-paper interaction. It is referred to be the reduction of light reflectance factors (R) on the backside of the printed sheet. It can be quantified by measuring the distance in the L^*a^*b space (see Eq. 2.27) between unprinted and printed paper (Chinga et al., 2007b; Eriksen and Gregersen, 2005). The index u refers to unprinted and index p to printed, respectively.

$$PT = \sqrt{(L_p - L_u)^2 + (a_p - a_u)^2 + (b_p - b_u)^2} \tag{2.27}$$

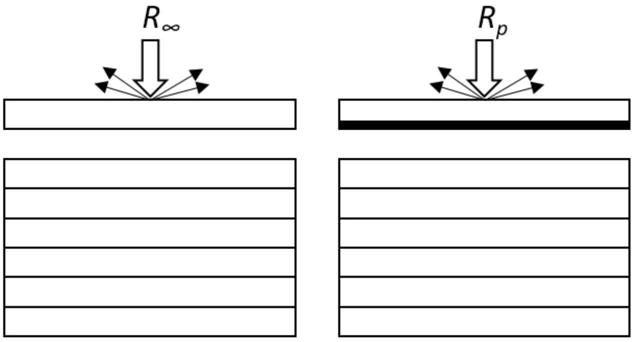

Figure 2.14 Reflectance measurements to calculate print through according to Eq. 2.29.

Print through comprises of three different effects. First, when the pigment particles move deeper into the paper, the visibility of the ink on the backside of the paper sheet increases. Secondly the decrease of opacity due to separation and penetration of the ink vehicle and at last, the show through which is the transparency (opacity) of the paper (see Equation 2.28).

$$PT = PT_{ST} + PT_{PP} + PT_{VS} \tag{2.28}$$

where

PT_{ST} ... show through component
PT_{PP} ... pigment penetration component
PT_{VS} ... vehicle separation component

According to Larsson and Trollsas (1976) the total print through can be expressed by Equation 2.29 where R_∞ is the reflectance of the unprinted sheet measured over a sufficiently thick layer of sheets and R_p the reflectance of the reverse side of the printed sheet respectively. This method is the traditional way of describing print through (Larsson and Trollsas, 1976; Makinen et al., 2008, 2007). The reflectance measurements needed to calculate print through are depicted in Figure 2.14.

$$PT = log\left(\frac{R_\infty}{R_p}\right) \tag{2.29}$$

Within this thesis, print through was determined in a different way than described above. On the local (i.e. micrometer) scale, overall measurements such as the above suggested ones are not applicable. Thus, a different approach for examination of ink penetration was chosen. For determination of the ink penetration, $R_{0,r}$, the re-

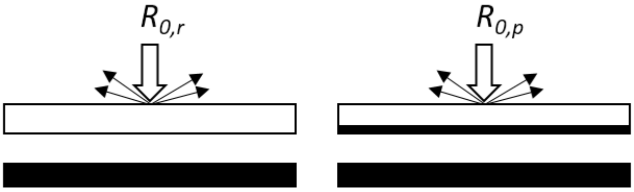

Figure 2.15 Reflectance measurements to calculate ink penetration according to Eq. 2.30.

flectance of the reverse side of the unprinted sheet over a black standard and $R_{0,p}$, the reflectance of the reverse side of the printed sheet was measured (see Fig. 2.15). The ink penetration IP was then defined as the ratio of $R_{0,r}$ to $R_{0,p}$ as illustrated by Equation 2.30. IP increases with increasing ink penetration and vice versa. The advantage of using this type of characterisation is, that the show through caused by the sheet opacity is eliminated. Thus, the pure influence of the ink penetration is observed. The ink penetration was measured with the IFM in the imaging mode and diffuse lighting conditions with the 2.5 zoom objective and with a pixel size of 25.6 µm/pixel.

$$IP = \frac{R_{0,r}}{R_{0,p}} \tag{2.30}$$

2.6 Topography under Load

Many printing techniques such as offset - and rotogravure printing are based on the principle that the printing ink is transferred in a pressure nip. Therefore, besides surface smoothness or topography without loading, surface smoothness under load is of high importance for print quality. Under an increasing compressive load, paper thickness decreases on the one hand and on the other hand the surface smoothness increases (Heikkilä, 1997).

In general there are three different measurement principles for topography under load available with various measurement devices (Bliesner, 1970; Chapman, 1954; Fetsko, 1958; Singh, 2008; Wagberg and Johansson, 1993):

- Air flow techniques (or air leak techniques)
    - Bekk
    - Bendtsen
    - Parker Print Surf
- Optical contact techniques
    - Fograkam

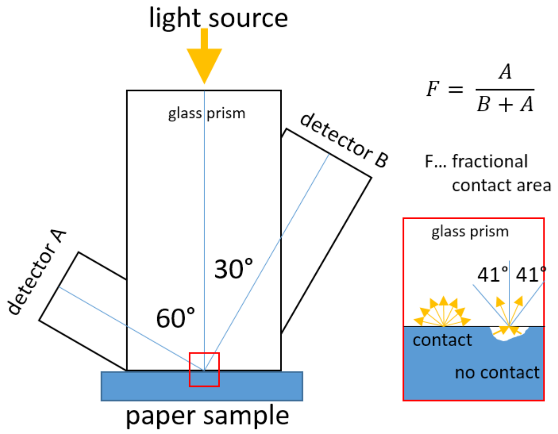

Figure 2.16 Schematic drawing of the principle of the Chapman prism.

  - Chapman prism
  - Print simulation tester
- Surface profilometry
  - Universal surface tester

Air flow techniques (e.g. Bekk, Gurley, Bendtsen, Sheffield and Parker Print Surf) generally measure the required time for a given quantity of air to flow between a sample and a flat surface pressed against it (Fetsko, 1958; Lechthaler and Bauer, 2006). The smoother the sample, the longer the given amount of air needs to flow through the gap. Air flow techniques are criticised because the results obtained can be influenced by the permeability of the sample. Furthermore, the results represent a gross average whereas smoothness varies locally to a large extent. In addition, the conditions (e.g. applied pressure) do not exactly approach those used in the printing machines (Bliesner, 1970).

Optical methods of smoothness measurements are based on the use of a glass prism pressed against a sample such as the Chapman prism. A light beam is sent through a glass prism and its reflectance is measured at two angles. If the prism is not in optical contact with the sample, the light beam reflected is confined to a cone of about 41° according to Snell's law (refractive index of glass prism = 1.52, see Eq. 2.32). However, if the paper sample is in optical contact with the prism the light beam is scattered. When measuring the amount of light within and outside the 41° cone, one can calculate the fractional contact area (Chapman, 1954). The operating principle of the Chapman prism is illustrated in Figure 2.16. Fetsko (1958) compared in his study air flow techniques to the Chapman prism and concluded that the optical method matched the visual ranking tests at the best. The Chapman prism was further devel-

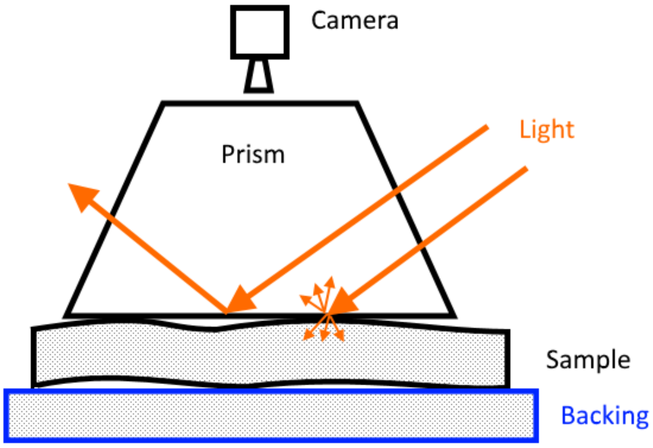

Figure 2.17 Schematic drawing of the principle of the Print Simulation Tester (PST).

oped resulting in optical smoothness tester such as the FOGRA optical contact tester (FOGRA, Germany) used by Klein et al. (2006) or the Print Simulation Tester (PST, Fibro System AB, Sweden) described in Boström (2012). In Figure 2.17 a schematic drawing of the principle of the PST is depicted where a light beam travels through a prism similarly to the Chapman prism (i.e. illumination source and detector system was interchanged) and the fraction of contact and no contact is calculated. The calculation is threshold based. The third group involves measurement techniques which record the **surface profile** either with an optical stylus (e.g. Chinga et al. (2007a); Sung et al. (2005); Wagberg and Johansson (1993)) or with an mechanical stylus (e.g. Singh (2008)). Wagberg and Johansson (1993) compared an optical profile tester to a mechanical stylus profilometer and concluded that coating structure and fibre composition could be clearly described with both methods. Lechthaler and Bauer (2006) described a mechanical stylus profilometer (i.e. UST Mistan, Innowep, Germany) which is able to capture the viscoelastic behaviour (e.g. compressibility) of paper by applying different loads on the stylus. The advantage of mechanical profiling is that geometrical features of the surface are directly recorded. However, when applying a certain load onto a small stylus (e.g. 5 µm) there is the inherent risk of scratching or marking (Singh, 2008; Wagberg and Johansson, 1993). Thus, this technique is not applicable for modelling local print density because the marks would influence the subsequent printing of the sample.

The smoothness under compression or topography under load in this thesis was measured with the Print Simulation Tester (PST) introduced by Boström (2012). The PST enables measurement of topography under load at various nip loads (i.e. up to 10 MPa) and with various dwell times (i.e. 5 ms to 1000 ms). Thus, the testing set up can be adjusted to simulate the desired printing procedure. For example, typical nip loads for flexography printing are between 0.1 MPa to 0.5 MPa, for offset printing

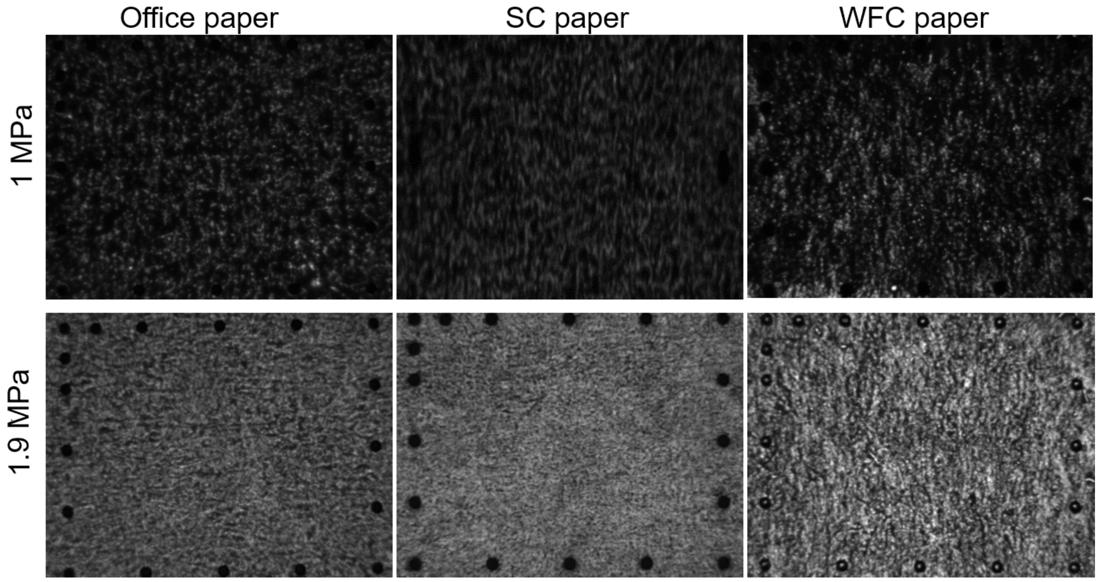

Figure 2.18 PST images of three different paper grades captured at two nip loads (size of images 9 mm × 10 mm).

0.8 MPa to 2 MPa and for rotogravure printing 1.5 MPa to 2 MPa (Kipphan, 2000). Furthermore, the backing (see Fig. 2.17) can be replaced and adjusted to the desired backing used in the real printing process.

For the measurements within this thesis the always same backing (i.e. rubber blanket from offset printing machine) was used. For different paper grades various nip loads were evaluated. In Figure 2.18 there are images of three different paper grades — office paper for xerography printing, SC paper for rotogravure printing and woodfree coated paper for sheet fed offset printing — at two nip loads (i.e. 1 MPa and 1.9 MPa) depicted. It is apparent from Figure 2.18 that a certain nip load is required to obtain a grey value image which can be used for further analysis. At a nip load of 1 MPa the histogram of the obtained image was clipped and calculation of a threshold became impossible. Thus, the black regions exhibit no valuable information regarding contact and no contact. Therefore, it was decided to adjust the nip load in order to achieve usable images. The adjustments were chosen to be within the range of the nip loads of the real printing process. The size of the sample was 9 mm × 10 mm and the size of the finally examined area was 7 mm × 7 mm in order to avoid effects from the laser holes (see Fig. 2.18).

2.7 Formation

Formation is one of most important structural characteristics of paper. Formation, which is the distribution of basis weight in paper, affects many other properties (e.g.

thickness, opacity and porosity). The main approach to capture the local basis weight is by measuring the transmittance of radiation. The relationship between grammage and transmittance of radiation is expressed by the Lambert-Beer equation (see Eq. 2.31) (Kajanto, 1989a).

$$T = \frac{I}{I_0} = e^{-\alpha m} \tag{2.31}$$

where T is the transmittance of radiation, I and $I_0$are the intensities of transmitted and incident radiation, m is the grammage and α is the absorption coefficient. When using the visible region of the electromagnetic spectrum as radiation (i.e. optical measurement) it is known that the scattering coefficient and absorption coefficient (as described in Section 2.4) of paper influence the absorption coefficient α and Equation 2.31 had to be adjusted as described by Tomimasu et al. (1991). For example, different amounts of fines and fillers or dye additives influence the transmittance of light through the sample. Thus, the composition of the paper sample strongly influences the result. Furthermore, optical formation is only applicable for uncalendered paper grades, because for calendered paper, optical transparency showed now correlation with local basis weight. The density variations are creating such differences in local scattering, that regions with high local grammage are more transparent (e.g. calender blackening of SC paper) (Komppa and Ebeling, 1981). Despite these drawbacks, the measurement of optical formation is widely used in paper manufacturing (e.g. Bernie and Douglas (1996); Tomimasu et al. (1991)).

A more accurate characterisation of mass distribution is achieved with more energetic sources such as X-rays, β-rays and electron beams. This type of radiation overcomes scattering effects of paper (Tomimasu et al., 1991, 1989). Keller and Pawlak (2001); Keller et al. (2004) give a comprehensive overview on the assessment of local basis weight with β-rays using storage phosphor screens. They concluded that β-radiographic imaging with storage phosphor screens is an accurate method for measuring local basis weight and more simple with regards to imaging and digitisation procedures compared to other β-radiographic methods.

The method of choice in this thesis was β-radiographic transmission. The basis weight maps were captured by recording the β-radiographic transmission on storage phosphor screens in a Formex Betaformation Box (Science Imaging Scandinavia AB, Saltsjö-boo, Sweden) and subsequently scanned in a Fujifilm BAS 1800-II scanner (Fujifilm, Tokyo, Japan). The pixel size of the obtained images was 50 µm/pixel and each pixel represents an absolute measure for basis weight. Figure 2.19 depicts an exemplary basis weight of an office paper grade with a mean basis weight of 70 $\mathrm{g/m^2}$. Darker regions represent areas of lower basis weight and vice versa. By calculation of the mean value of the grayscale image one can verify the specified basis weight (assuming a sufficiently large sample). In case of the examined image the calculated mean value was 70.46 $\mathrm{g/m^2}$.

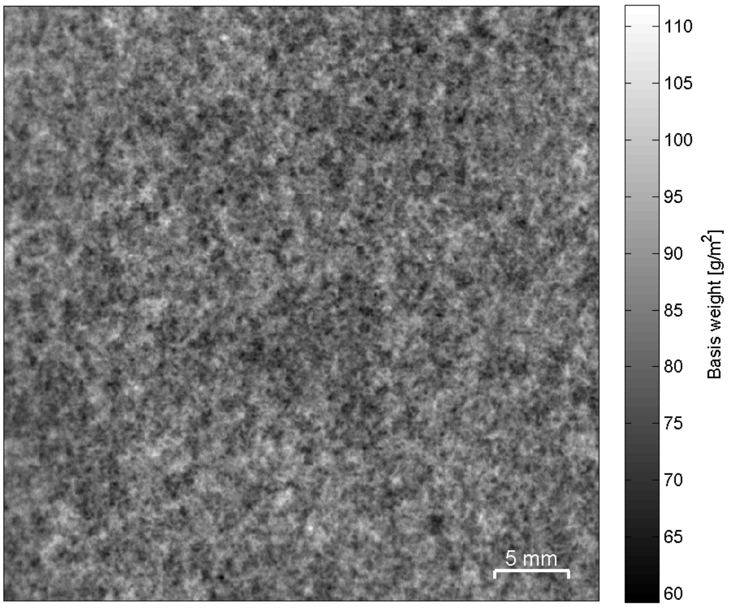

Figure 2.19 Grayscale image of local basis weight of an office paper (mean basis weight 70 g/m^2).

2.8 Polarised Light Reflectometry

The characterisation of paper surface structure also includes gloss measurements. The industrial standard gloss measurements are performed with a simple glossmeter (e.g. ISO 8254, TAPPI T480, TAPPI T653). A more sophisticated approach to assess gloss and other important surface and material properties is reflection goniometry or imaging reflectometry. The device used in this thesis is based on the reflection goniometer developed by Gate and Parsons (1993), it is discussed in detail in Elton and Day (2009). The Surfoptic Imaging Reflectometer (Data Systems, Bristol, UK) uses polarised light at two different wavelengths (635 nm and 670 nm).

The instrumental layout of the Surfoptic Imaging Reflectometer is illustrated in Figure 2.20. The fixed incident angle of the two laser beams is 75°. The light is reflected and scattered at the surface of the sample and subsequently the angular intensity distribution of the reflected light is captured with an imaging photodetector over a range of about ±10°. The scattered light is detected with another camera under 90° angle to the sample (Elton, 2007b). According to Elton (2007b) polarised light reflectometry with the Surfoptic Imaging Reflectometer enables quantitative analysis of:

- Effective refractive index
- Macroroughness

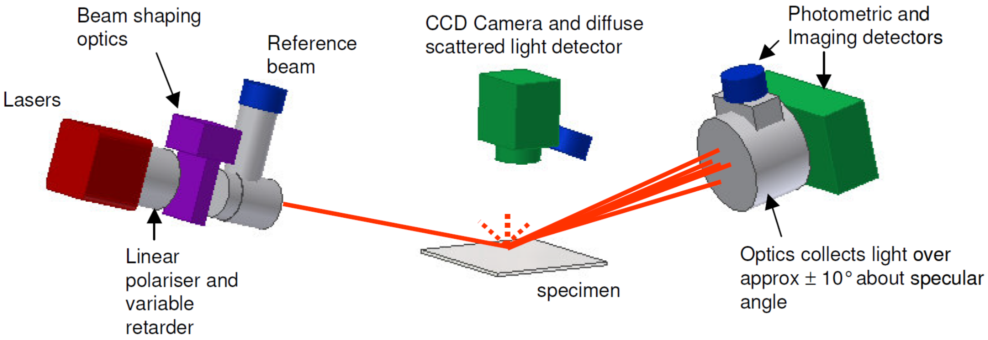

Figure 2.20 Schematic drawing of the Surfoptic Imaging Reflectometer (Elton, 2007b).

- Microroughness
- Gloss according to various standard definitions
- Surface reflectance anisotropy

The **refractive index** of a substrate describes how light propagates through that substrate and is defined as the fraction of the speed of light in vacuum to the velocity of light in the substrate. When it comes to refraction of light at an interface of two materials with the refractive index n_i and n_t (see Fig. 2.21) Snell's law (Eq. 2.32) describes the relationship between incident angle θ_i and the angle the transmitted light propagates through the second medium (i.e. refraction angle) θ_t. The electric field amplitude of the incident, transmitted and reflected waves are denoted as E_i, E_t and E_r in Figure 2.21.

$$\frac{n_i}{n_t} = \frac{\sin(\theta_t)}{\sin(\theta_i)} \tag{2.32}$$

The intensity of the reflected light beam R from a perfectly smooth, homogeneous, isotropic and non absorbing medium can be determined as follows:

$$R = \frac{|E_r|^2}{|E_i|^2} = R_P + R_S \tag{2.33}$$

Furthermore, the intensity reflection coefficient can be decomposed into two polarisation components which are described by the Fresnel equations (Eq. 2.34 and 2.35), one S polarised (i.e. orthogonal to the incident plane) and one P polarised (i.e. parallel to the plane of incidence) part (Elton and Preston, 2006a; Lvovsky, 2013).

$$R_P = \frac{\tan^2(\theta_i - \theta_t)}{\tan^2(\theta_i + \theta_t)} \tag{2.34}$$

$$R_S = \frac{\sin^2(\theta_i - \theta_t)}{\sin^2(\theta_i + \theta_t)} \tag{2.35}$$

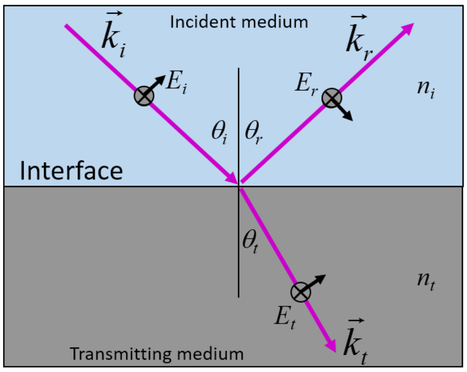

Figure 2.21 Geometry of reflection and refraction between the incident and transmitting medium at a smooth interface (adopted from Lvovsky (2013)).

Solving equations 2.32, 2.34 and 2.35 (assuming $n_i = 1$ for air) for n_t gives:

$$n_t = \sin(\theta_i)\left(1 + \left(\frac{1-\rho}{1+\rho}\right)^2 \tan^2(\theta_i)\right)^{1/2} \tag{2.36}$$

where

$$\rho = \sqrt{\frac{R_P}{R_S}} \tag{2.37}$$

Thus, by measuring the intensity of reflection of S and P polarised light, the refractive index can be determined according to Equation 2.36. The refractive index obtained by this method is called effective refractive index. Since paper is a complex material and composes of several components (e.g a coating layer or various types of fillers) the effective refractive index represents a combination of the individual refractive indices. According to Elton and Preston (2006a); Ström et al. (2010) the effective refractive index is a measure for surface porosity, because of the difference in refractive index of the particular component (i.e. air has n=1, thus, 1 for voids, 1.50 for latex, 1.56 for kaolin and 1.65 for calcium carbonate). Calendering experiments showed, that increased calendering resulted in higher TAPPI gloss and higher effective refractive index due to lower amount of surface pores.

The values of the effective refractive index are furthermore influenced by the surface roughness of the sample. Although, as mentioned above, the Fresnel equations are defined for perfectly smooth, homogeneous, isotropic and non absorbing surfaces, they are applicable. This is due to the fact that all reflection measurements are made at an incident angle of 75°, where the effects on the effective refractive index are expected to be negligible (Elton and Preston, 2006a). Exceptions are very rough sur-

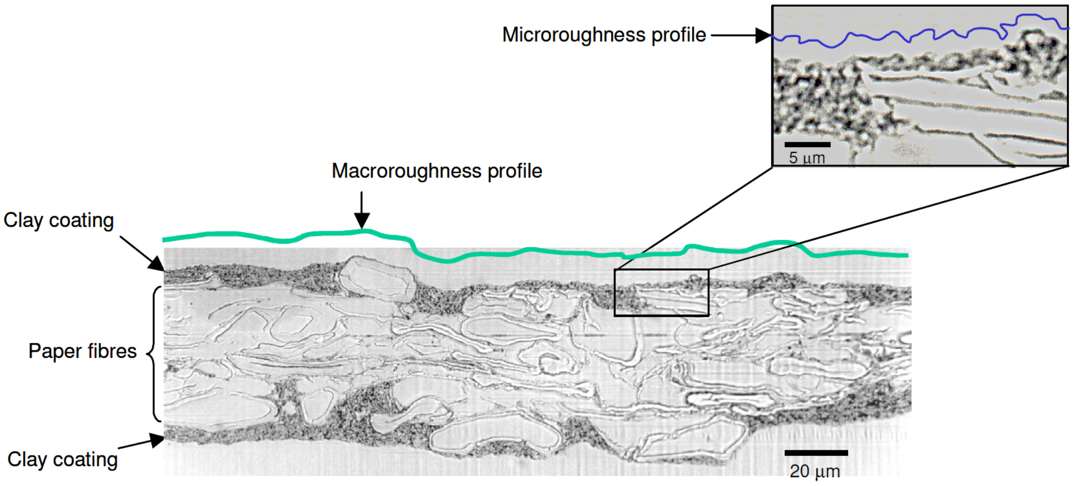

Figure 2.22 Optical microscope cross section of a light weight coated paper sample indicating the size scale of micro- and macroroughness (adapted from (Elton, 2007a)).

faces, materials with periodic structures or transparent multi layered materials (Elton, 2007b).

Another measure provided by the Surfoptic Imaging Reflectometer are two types of **roughness**. The roughness of a sample depends on how the roughness is measured (compare Section 2.3). For example when measuring surface roughness with a mechanical stylus with a 5 µm tip it may appear rough whereas it might appear smooth with a 50 µm tip. The same applies for reflectometry for a given surface roughness of the same scale as the wavelength of light. Within this order of magnitude or smaller the light scattering behaviour is wavelength dependent and is generally denoted as microroughness. Accordingly, roughness at a scale higher than the wavelength is denoted as macroroughness. An example of a micro- and macrorough surface is a coated paper sample (see Fig. 2.22). Macroroughness is mainly determined by the roughness of the base sheet comprising the base sheet structure and some effects of coating coverage and coating holdout. Microroughness on the other hand is mainly caused by the size, shape and packing of the coating pigment (Elton, 2007a; Elton and Preston, 2006a).

Micro- and macroroughness are measured by evaluating the angular distribution of the scattered light (i.e. the reflectogram in Figure 2.23) of the incident light. The imaging detector collects the scattered light over a range of about ±10°. The obtained reflectogram is subsequently analysed. The hypothesis is, that the shape of the reflectogram is determined by the macroroughness and that the microroughness contributes to the broadening of the reflectogram. Thus, the macroroughness is defined as the full width at half maximum (FWHM) of the distribution. Since microroughness is influenced by the wavelength of light, it can be determined by comparing the

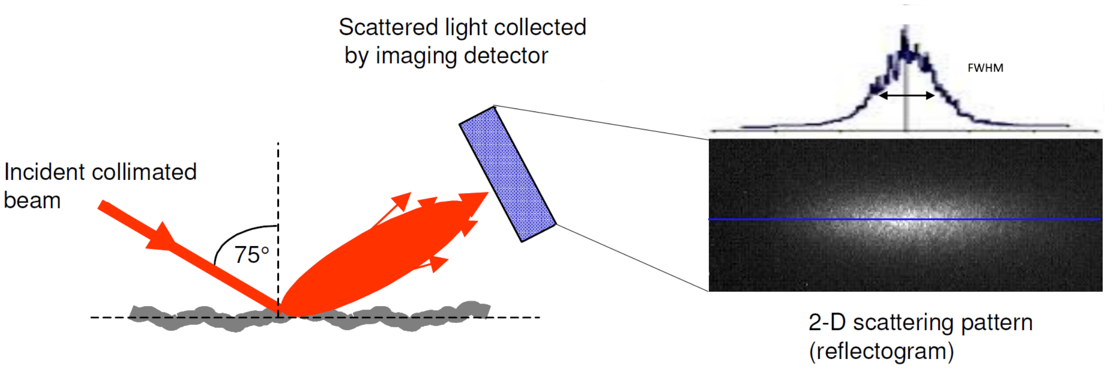

Figure 2.23 Schematic drawing of the basic principle of measuring micro- and macroroughness (Elton, 2007a).

reflected intensity at two wavelengths according to Beckmann and Spizzichino (Elton, 2007a; Pauler, 2012). The **gloss** measurements are calculated according to Equation 2.38. Gloss is defined as the fraction of the reflected intensity from a calibration standard I_c and the reflected intensity of the specimen I_m at a defined acceptance angle. The Surfoptic Imaging Reflectometer has two fixed photodectors, one with a nominal acceptance angle of 2° and one with 20° (Elton, 2007a).

$$G = \frac{I_m}{I_c} \times 100 \text{ in } [\%] \tag{2.38}$$

All measurements conducted (i.e. effective refractive index, gloss, micro- and macroroughness) with the Surfoptic Imaging Reflectometer (spot size of ~1 mm) are performed with a step size of a x-y linear table of 200 µm. Thus, the obtained pixel size of the surface property maps is 200 µm. The measurement technique applied in this thesis was evaluated by Wind (2011) and application to coated coated papers by Elton and Preston (2006b) showed that it is a useful tool to examine coating structure and for explaining the origins of gloss. Examples of the obtained measurements of one Wood Free Coated paper sample are depicted in Figure 2.24. The images show the same sample area because the measurements were obtained simultaneously.

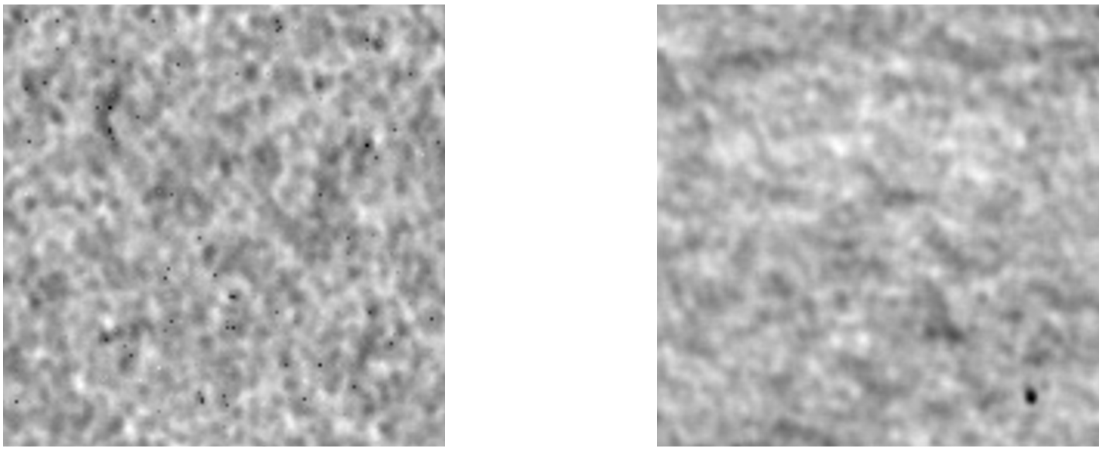

(a) Macroroughness.

(b) Gloss 20°.

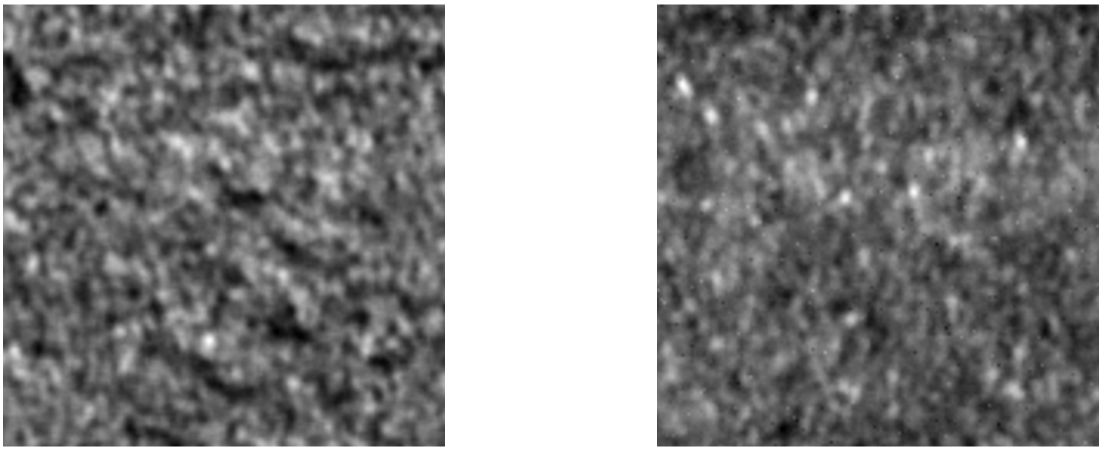

(c) Gloss 2°.

(d) Effective refractive index.

Figure 2.24 Examples of the Surfoptic Imaging Reflectometer of a Wood Free Coated sample (size of images: 40 mm × 40 mm).

2.9 Coating Layer Uniformity

The main part of this section comprises of the publications of Fuchs et al. (2015b,c) where the measurement method of ultra violet (UV) imaging for examination of the coating layer uniformity is evaluated.

In general, the analysis of coating layer distribution can be divided into two groups. The first group consists of methods for direct measurement of coating thickness in cross sections of paper. Scanning electron microscopy (SEM) combined with sectioning techniques is frequently used as a direct method. The single cross sections have a high resolution but a limited sample size. In order to facilitate the differentiation between coating layer and base sheet, imaging is performed in the back scattered electron mode (Dickson et al., 2002; Peterson and Williams, 1992). Allem (1998) introduced a concept which has been used to characterize local coating thickness and the correlation to base sheet properties (Dahlström and Uesaka, 2009; Zou et al., 2001).

Another direct method using serial sectioning combined with light microscopy and a novel image analysis technique was presented by Wiltsche et al. (2006). The method is capable of automatically obtaining 3D paper structure data for sample areas of about 100 mm^2 (e.g. 5 mm×20 mm) in a reasonable timeframe. In this method, the coating layer is identified by a color segmentation algorithm extracting the coating layer information from the paper cross sections images.

The second group consists of indirect methods which allow the characterization of relatively large sample areas (e.g. 50 mm×50 mm). The burnout test combined with image analysis is one of the most commonly used indirect methods to determine the coating coverage (Dobson, 1975). The burnout test is based on high temperature carbonisation of a paper sample. As a consequence, the cellulosic material becomes black, while the coating stays white. Coating layer unevenness is then evaluated by imaging of the coating on the blackened paper. The drawback of this method is, that the blackening of the base paper might be non-uniform and the porosity of the coating layer influences the result of the burnout treatment. Since the burnout method is based on reflection of light, different compression levels of the coating layer influence the light scattering properties of the coating layer. However, the burnout test provides direct assessment of the optical homogeneity of the coating layer which is most relevant for the perceived print quality of the paper. Thus, the burnout test has successfully been applied as a reference method (e.g. (Azimi et al., 2009; Dahlström et al., 2008; Järnström et al., 2010)).

Furthermore, radiography has been used with X-ray imaging by Azimi et al. (2009). A paper sample is exposed to X-rays and the transmitted X-rays are detected providing a gray scale image. To eliminate the base sheet absorption effect, the average absorption due to the base sheet was subtracted from the X-ray image of the coated paper. Kartovaara (1989) used β-radiography for determination of local coating mass distribution, by subtracting the local grammage of the uncoated base paper from the local grammage of the coated paper. Tomimasu et al. (1989, 1990) used electron beams (50 keV to 200 keV) for a similar approach. They concluded, that the advantages compared to β-radiography are a higher image resolution and a reduced exposure time.

Another indirect method is inspection of coated paper under UV light making use of the fluorescence behaviour of the fluorescing whitening agent (FWA) primarily contained in the coating layer. It is a standard procedure in many paper mills targeting the detection of coating layer defects. The coated paper is placed under UV light under controlled lighting conditions and visually checked for coating faults and coating layer uniformity. UV fluorescence imaging has also been utilized for measuring coating layer distribution with a simple setup (Carlsson et al., 2004; Järnström et al., 2010). The coated samples were illuminated by two UV light sources and images were captured with a camera. Afterwards the burnout test was performed on these samples. The coefficients of variation of both images were compared and indicated a reasonable correlation between both methods.

The purpose of the studies (Fuchs et al., 2015b,c) was to evaluate the suitability of high resolution UV scanner imaging as a fast, simple and non-destructive way to estimate the spatial uniformity of the coating layer. Different coated paper grades — commercial as well as hand sheets — were evaluated. The FWA present in the coating color was used as an internal marker providing valuable information regarding the spatial coating layer formation. Initial results of the application of this method (Fuchs et al., 2014) showed a high correlation of the results obtained by UV scanner imaging to burnout test images, especially for light-weight coated paper.

Furthermore, in Fuchs et al. (2014) it was shown that the light source and detector geometry (described in Section 2.9.2) causes problems when measuring very rough samples. In order to overcome this so called shadowing artefact another method for measuring the spatial coating layer formation with a UV light source will be introduced in Section 2.9.2.

It is obvious that the FWA amount contained in the coating formulations and in the base paper will influence the intensity of fluorescence and thus the results of UV scanner imaging and the subsequent estimation of spatial coating layer formation. In order to evaluate this influence, laboratory trials were carried out varying the concentration of FWA in the coating color (e.g. less FWA corresponds to lower fluorescence intensity) and in the base paper respectively. As the intensity of fluorescence is likely to be also influenced by the applied coat weight, laboratory trials with varying coat weight were also conducted.

2.9.1 Evaluation of UV Scanner Imaging Method

For evaluation of the UV scanner imaging method three different substrates were used:

1. Lab coated hand sheets (HS), 80 g/m^2, 100 % refined eucalypt kraft pulp (2000 revolutions in a PFI mill), part of the hand sheets contained no FWA. These hand sheets had a brightness of 87.85 %. The other part contained 1 % FWA (Blankophor® PT, BASF) and had a brightness of 108.38 %.

2. Lab coated commercial wood free baser paper (WFC), 70 g/m^2, containing 30 % broke and 15 % filler (i.e. $CaCO_3$ and clay). WFC base paper contained a small amount of FWA due to the usage of broke (brightness 83 %).

3. 4 samples of commercially produced light-weight coated (LWC) paper, 80 g/m^2, furnish composition: 40 % groundwood pulp, 50 % recycled pulp and 10 %

bleached softwood kraft pulp, coat weight per side 14 g/m^2. LWC contained FWA in the base paper due to the usage of broke.

Table 2.1 shows the coating color recipes. The FWA content in the coating formulation varied from 0.1 % to 0.3 %.

Table 2.1 Coating formulation.

In parts	Colour 1	Colour 2	Colour 3
GCC	100	100	100
FWA (Blankophor® PT)	0.1	0.2	0.3
PVOH	0.5	0.5	0.5
SB Latex	8	8	8
Solids Content	70 (65)	70	70

The HS samples (with and without FWA) were blade coated on one side on a laboratory blade coater (Enz Technik AG, Switzerland) in the stiff blade mode using a blade of 0.4 mm thickness. The applied blade pressure was identical for all samples. The target coat weight for these samples was 19 g/m^2.

The commercial WFC base paper was coated with Colour 1 (see Tab. 2.1) using a laboratory flat-bed rod coater (Control Coater, RK Print Coat Instruments Ltd, England). Three standard metering rods were used to apply the target coat weights of 13 g/m^2 to 32 g/m^2. The solids content of the coating color was reduced to 65 % to achieve the lower coat weights. The coated samples were dried in a drying chamber at 150 °C for about 2 minutes.

UV Scanner Imaging

The UV flatbed scanner (Chromimage®, AR 2i, France) used for this study was equipped with a low pressure mercury vapour lamp. The spectral energy distribution of the mercury vapour lamp is shown in Figure 2.25a. The primary energy emission is located in the UV region of the electromagnetic spectrum with the maximum intensity located at a wavelength of 253.7 nm. Hence, the emittance of the lamp is in the region, where the FWA absorbs the energy (see Fig. 2.25b). As a consequence, the image information obtained from UV scanner imaging is based on the reflection of the emitted blue light of the excited FWA. A small amount of energy is also emitted in the visible range of the EM spectrum. The fluorescent light source is located at an angle of about 45° and the detector is located at 90° on the scanning head, compare Figure 2.35.

The sample size may be varied up to maximum size of an A4 sheet and the scanning speed depends on the chosen resolution. For the used settings, one scanning cycle lasted three minutes. All samples were scanned at 1200 dpi (pixel size of 21.17 nm)

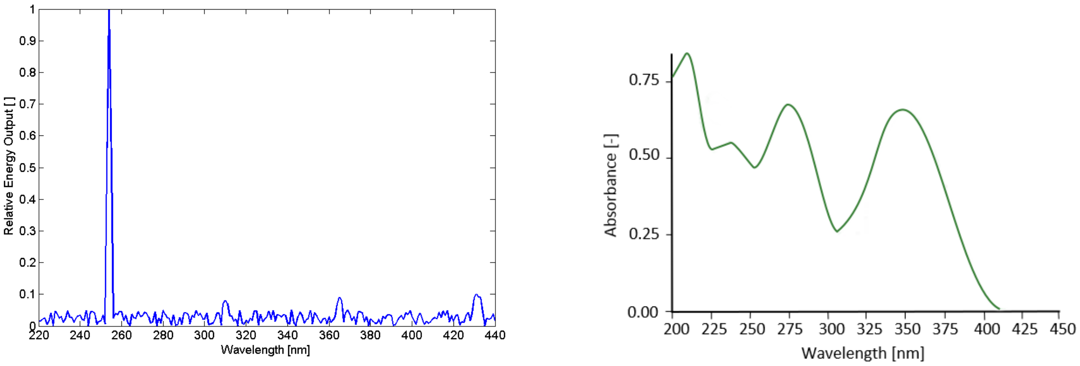

(a) Spectral energy distribution of the low pressure mercury vapor lamp installed in the UV scanner (adopted from www.crystec.com).

(b) Absorbance spectrum of the FWA Blankophor® P, BASF.

Figure 2.25 Characteristics of the UV scanner and the FWA.

in full RGB colour. Since the excited FWA emits energy mainly in the blue region of the visible light, only the blue channel has been used for evaluation of spatial coating layer formation.

Reference Methods

Two methods were used as independent reference methods. First the burnout test for imaging spatial coating layer formation and secondly the β-radiography method for calculation of local coat weight maps.

The burnout test is an easy and fast method used to visualize the uniformity of the spatial coating layer formation on coated papers. The paper samples are soaked in a charring agent and afterwards placed in an oven at a temperature of 225 °C. High temperature dehydration of the paper samples causes the cellulosic materials to become black while the inorganic coating color remains white. In case of using samples containing mechanical pulp fibres, inadequate blackening is caused by the presence of lignin (O'Neill and Jordan, 2000). Trimmel et al. (2012) presented a burnout test for wood containing papers and this procedure has been chosen for carbonisation of all samples containing mechanical pulp (LWC) as well as for the wood free samples (WFC and HS). Imaging of the burnout test samples was carried out with the IFM (see 2.4) using diffuse lighting conditions with a pixel size of 25.6 µm. The resulting images were converted into grey scale value images.

β-radiography was utilised as another reference method in the evaluation of the UV scanner imaging method for the WFC samples. Basis weight maps with a pixel size of 50 µm before and after coating were captured by β-radiographic transmission and recorded on a phosphor storage screen (as described in 2.7). Local coat weight maps were calculated after registration (see Sample Handling and Image Analysis) of the images by subtracting the basis weight map before coating from the basis weight map after coating. In an analogue procedure the coat weight was gravimetrically determined by weighing the samples before and after coating. The correlation of the gravimetrically obtained coat weights and the mean gray value of the coat weight map led to a R^2 of 0.96 (slope 0.99, intercept 0.99). Thus, the resulting information of the coat weight map is an absolute measure for coat weight.

Sample Handling and Image Analysis

Prior to any measurement, all paper samples were marked with holes (500 µm diameter) introduced by a CO_2 laser as described by Hirn et al. (2009a). These holes were needed for subsequent image registration which is performed by a shape preserving coordinate transform according to Hirn et al. (2008), see 2.1. This assured a point by point correlation of the images obtained from the measurements. The marked samples had a size of 45 mm × 45 mm and the examined area was 40 mm × 40 mm.

The human eye visually perceives non-uniformities differently at different length scales. The region of interest for visual perception of print mottle according to Johansson (1993) is located in the wavelength band of 2 mm to 8 mm. Knowing that coating uniformity is crucial for print quality (Allem, 1998; Allem and Uesaka, 1999; Dahlström and Uesaka, 2009; MacGregor and Johansson, 1991), spectral filtering (i.e. a FFT pass band filter) was performed with a pass band ranging from 2 mm to 8 mm. Afterwards the images were rescaled to a pixel size of 250 µm in order to minimize the registration error.

After spectral filtering and rescaling, the images acquired from the UV scanner, β-radiography and the burnout test were point wise correlated. Figure 2.26a shows the result of a point wise correlation of a burnout test – and an UV scanner image. Every point in the scatter plot represents the measurement results of one square with size 250 µm × 250 µm on the paper. The coefficient of determination (R^2) of the linear regression was utilized as a measure of the similarity between the UV scanner images and the images of the reference methods. A R^2 value of 1 indicates a perfect linear relationship between the measurement results, a value of 0 means that the measurements are not related. Thus, the R^2 value quantifies how well UV scanner imaging coincides with the reference methods. The coefficient of determination between UV scanner images and burnout test images was calculated for the HS, LWC and WFC samples. In addition, R^2 between UV scanner images and β-radiography images were calculated for the WFC samples.

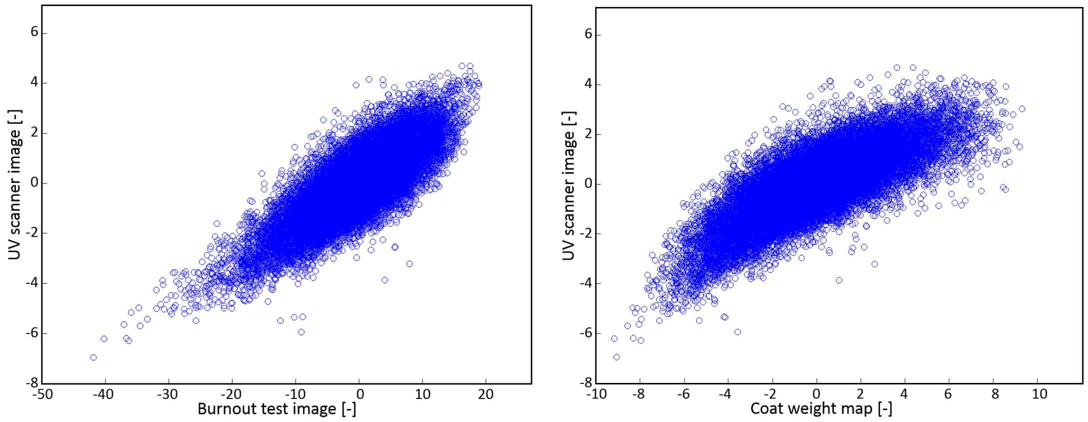

(a) Point wise correlation of the UV scanner image and the burnout test image shown in Figure 2.28d and 2.28e.

(b) Point wise correlation of the UV scanner image and the coat weight map shown in Figure 2.28d and 2.28f.

Figure 2.26 Point wise correlation of the pass band filtered UV scanner image and the image of the burnout test **(a)** and the coat weight map **(b)**. The images are depicted in Figure 2.28d, 2.28e and 2.28f. Each dot in the scatterplot represents the measurement result in a paper surface area of 0.0625 mm^2. R^2 between the two images in **(a)** is 0.64 and **(b)** 0.62.

In theory a logarithmic relationship between local coat weight and local light remission can be expected. However, it turns out that in fact the relationship between coat weight (in $\mathrm{g/m^2}$) and light remission of the burnout test and UV scanner images is almost linear. Figure 2.26b shows the point wise correlation of UV scanner images and the coat weight map. The cloud of points is bent slightly. An almost linear relation between coating thickness and light remission was also described in Hirn et al. (2009a).

The coefficient of determination (R^2) of the linear regression exhaustively describes the linearity between the measurement methods. Slope and intercept of the regression analysis was not reported because these values are fully controlled by the scanner settings (i.e. illumination, gain and cutoff of the sensors) and thus provide no useful information. If there is a direct, linear relationship between the results of the individual measurement methods, this information is fully covered by the reported R^2 value of the linear regression.

Results of the Evaluation

The investigated methods for coating layer evenness — UV imaging, burnout test and beta radiography — are reflecting three different aspects of the coating layer distribution. β-radiography measures the actual local coat weight but neglects local variations of the optical properties. Especially density variations of the coating, which impairs optical coverage, is not detected by radiography. The burnout test instead captures the actual optical coverage of the coating layer, however it is influenced by coating density variations and by inhomogeneous blackening of the base paper. The UV imaging technique is mainly influenced by the fluorescent whitening agent and its distribution in the coating layer. A key insight of this evaluation is that these three different techniques provide widely equivalent results for low coat weights.

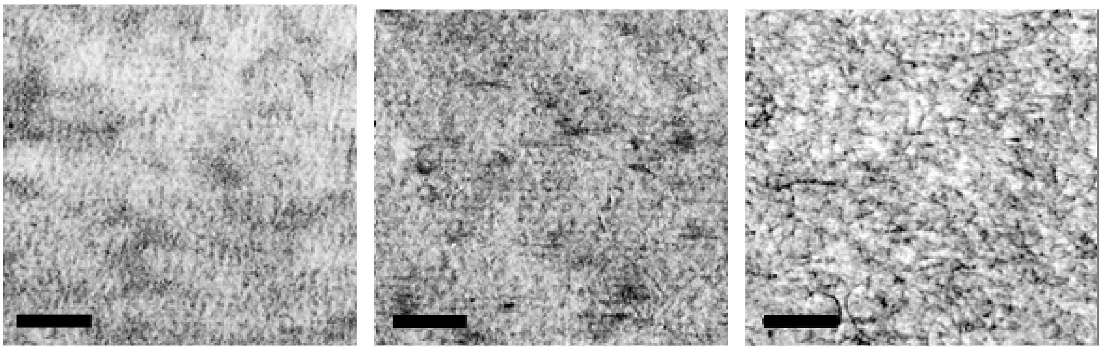
(a) HS lab coated. **(b)** Lab coated WFC base paper. **(c)** Commercial LWC sample.

Figure 2.27 UV scanner images of **(a)** lab coated HS sample: coat weight 19 g/m^2, Colour 1, no FWA in base paper, and **(b)** lab coated WFC base paper: coat weight 13 g/m^2, Colour 1, and an industrial LWC sample **(c)**, scale bar = 2 mm.

In Figure 2.27, UV scanner images using only the blue channel of a lab coated HS sample **(a)**, a lab coated WFC base paper sample **(b)** and an industrial LWC sample **(c)** are shown. The contrast of all images depicted in this study was enhanced in order to achieve a better visibility. In the UV images, darker regions represent regions containing less FWA and brighter regions those containing more FWA. Darker areas, especially in the WFC **(b)** and LWC **(c)** images look like fibres or fibrous features, which are apparently less covered with coating color. Since the FWA is mainly contained in the coating color, lower luminosity should be related to locally lower coat weight.

The burnout test was performed on all samples (LWC, HS and WFC). Furthermore, β-radiography was performed on the flat-bed rod coated samples (WFC), before and after coating to calculate local coat weight maps. In Figure 2.28 the images of all measurements of one WFC sample (13 g/m^2 coat weight with Colour 1) are depicted. The images are registered (see Sample Handling and Image Analysis) and have a size of 40 mm × 40 mm. Registered means that the measurement areas are congruent, i.e. each position in all three images refers to exactly one position on the paper sample.

Figure 2.28a, 2.28b and 2.28c show the contrast enhanced raw images obtained from UV scanner imaging. The images below the raw images show the corresponding images after spectral filtering in the wavelength band from 2 mm to 8 mm (Fig. 2.28d, 2.28e and 2.28f). When comparing the images **(d)**, **(e)** and **(f)**, the similarity between the images can be observed (see dashed ellipse as an example). R^2 between UV scanner image **(d)** and burnout test image **(e)** is 0.64 and between UV scanner image **(d)** and coat weight map (β-radiography) **(f)** 0.62. The information obtained from UV scanner imaging is similar ($R^2 = 0.62 - 0.64$) to the information obtained from both reference methods. This indicates that UV imaging of the FWA in the coating indeed reveals the spatial coating layer formation

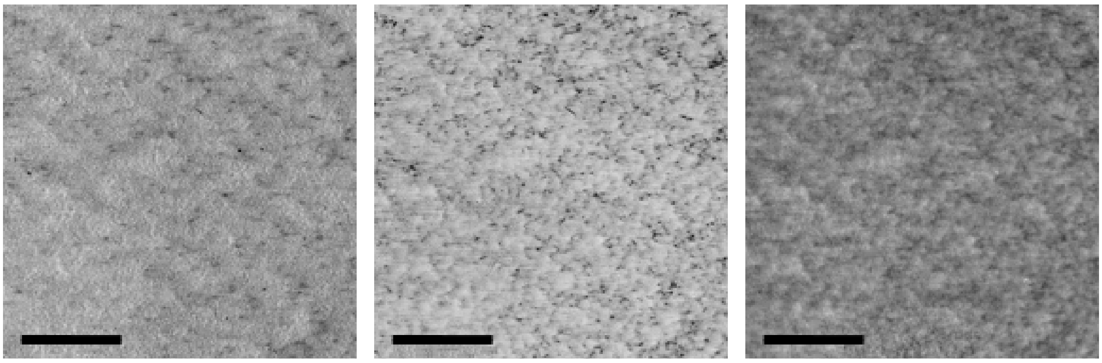

(a) Raw UV scanner image. **(b)** Raw burnout test image. **(c)** Raw β-ray map.

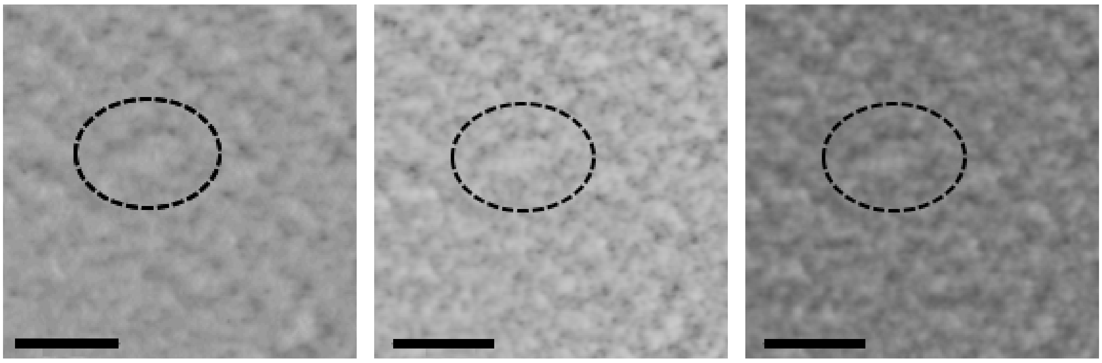

(d) Filtered UV scanner image. **(e)** Filtered burnout test image. **(f)** Filtered β-ray map.

Figure 2.28 Images of registered WFC sample (coat weight 13 g/m^2, Colour 1) before and after spectral filtering (2 mm to 8 mm pass band). R^2 between **(d)** and **(e)** is 0.64 and between **(d)** and **(f)** 0.62, scale bar = 10 mm.

Influence of coat weight on the correlation

Figure 2.29 shows the coefficient of determination (R^2) of the UV scanner images to the burnout and β-radiography images in dependence of the applied coat weight for the WFC samples. Each point represents the R^2 of the point wise correlation of one sample. In Figure 2.29 a good correlation between UV scanner imaging and burn out test images can only be observed for low coat weight samples. There is also a reasonable correlation between UV scanner images and local coat weight maps obtained from β-radiography images ($R^2 = 0.58$) again only at low coat weights. R^2 clearly decreases with increasing coat weight. One likely reason for that is the better coverage of the base paper at higher coat weights leading to a lower variance in fluorescence intensity. This effect could be explained on the basis of the images depicted in Figure 2.31. Another explanation could be the coating thickness itself. The thicker the coating layer, the higher is the opacity of the coating layer. As a consequence only the light emitted from the top surface layer of the coating is detected. This effect could be aggravated by migration of the FWA into the paper. With lower solids content and slower drying during coating increasing amounts of water and FWA penetrate into the paper. The migration of the FWA may also be influenced by the carrier used (i.e. PVOH).

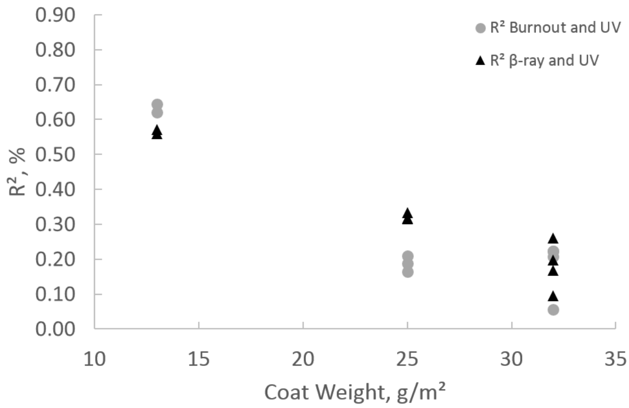

Figure 2.29 R^2 of point wise correlation of UV scanner -, burnout test - and β-radiography images of WFC samples coated with Colour 1.

Figure 2.30 displays the R^2 between β-radiography images and the burnout test images. This diagram shows how well the burnout test corresponds to the absolute information of β-radiography coat weight map. The R^2 values are generally higher and there is a similar trend as can be seen in Figure 2.29. With increasing coat weight, the correlation decreases. The higher the coat weight, the lower the ability of the blackened base paper in the burnout test to shine through the coating layer and to provide enough contrast for a proper analysis of the coating layer distribution. The burnout test and UV scanner imaging are both based on reflection. Thus, both methods are less effective at high coat weights (>19 g/m^2).

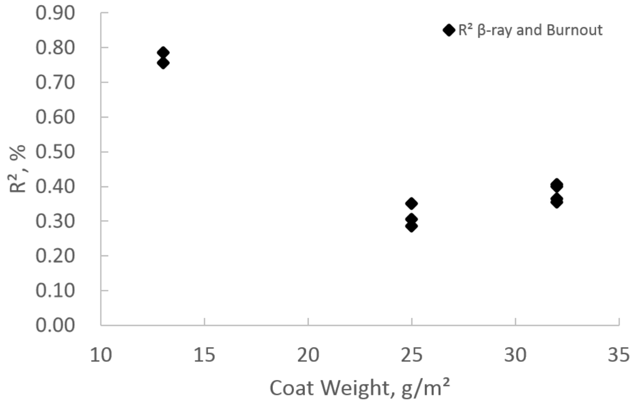

Figure 2.30 R^2 of point wise correlation of burnout test - and β-radiography images of WFC samples coated with Colour 1.

Figure 2.31 shows examples of the UV scanner images of WFC samples with different coat weights, coated on the flat-bed rod coater (Colour 1). From the images it is apparent that the fluorescence intensity becomes more homogeneous with increasing coat weight. Furthermore, fibrous features in the image representing the sample having the highest coat weight (Figure 2.31c) are not visible whereas those features are present in the image of the sample with the lowest coat weight (Figure 2.31a). This is due to the higher coat weight that leads to a better coverage of the base paper. Furthermore, the thicker coating layer hinders the emitted light to be detected. This implies that the determination of the spatial coating layer formation with UV scanner imaging is better suitable for paper grades of lower coat weights.

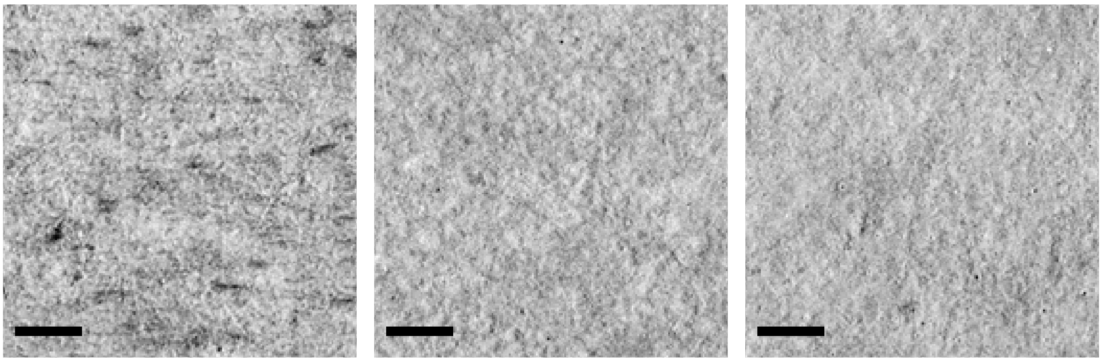

(a) WFC sample (13 g/m^2). **(b)** WFC sample (25 g/m^2). **(c)** WFC sample (32 g/m^2).

Figure 2.31 UV scanner images of flat-bed rod coated (Colour 1) WFC samples with coat weights **(a)** 13 g/m^2, **(b)** 25 g/m^2 and **(c)** 32 g/m^2, scale bar = 2 mm.

Influence of variation of FWA concentration in the coating color

The coefficient of determination (R^2) of the UV scanner images to the burnout test images in dependence of the FWA amount in the coating color applied to the hand sheet samples containing no FWA is shown in Figure 2.32. Each bar in Figure 2.32 represents the mean R^2 of the point wise correlation of at least two HS samples. R^2 decreases with increasing FWA amount in the coating color for the blade coated HS samples. The lower the FWA concentration in the coating color, the higher is the correlation between the measurement methods.

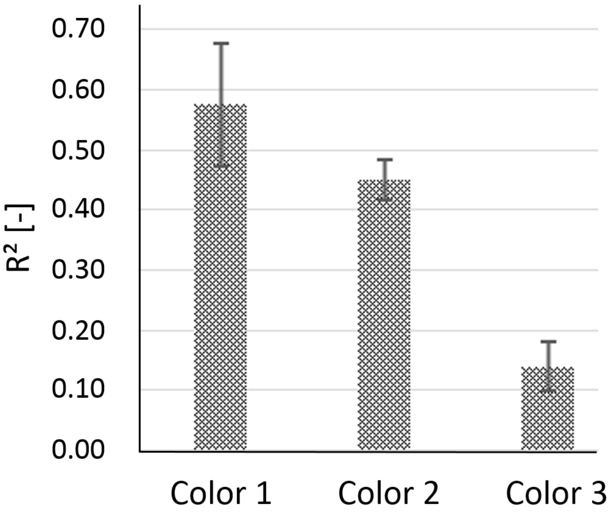

Figure 2.32 R^2 of point wise correlation of burnout test - and UV scanner images of HS samples (without FWA in base paper) coated with Color 1 (0.1 % FWA), Color 2 (0.2 % FWA) and Color 3 (0.3 % FWA).

A possible reason for this can be seen in the images depicted in Figure 2.33 showing images of blade coated HS samples (19 $\mathrm{g/m^2}$ coat weight) with different FWA content (0.1 % to 0.3 %). For these images a similar effect occurs as found for those in Figure 2.31. Areas (i.e. structure size $\simeq$2 mm) having higher and lower luminosity can clearly be distinguished in the image of the sample containing a lower concentration of FWA (see Figure 2.33a and 2.33b), whereas at higher FWA concentration the difference between these structure size regions is almost impossible to detect, the scale of the structures dominating is smaller (Figure 2.33c). The higher the concentration of FWA in the coating color, the higher the average fluorescence intensity level and therefore it might be that differences between regions of locally higher or lower coat weight cannot be observed. As a result, the determination of local coat weight distribution determined by UV scanner imaging appears to be more precise at lower FWA concentrations in the coating color. This is contrary to our expectations that a higher amount of FWA in the coating color gives a better contrast and thus a higher correlation.

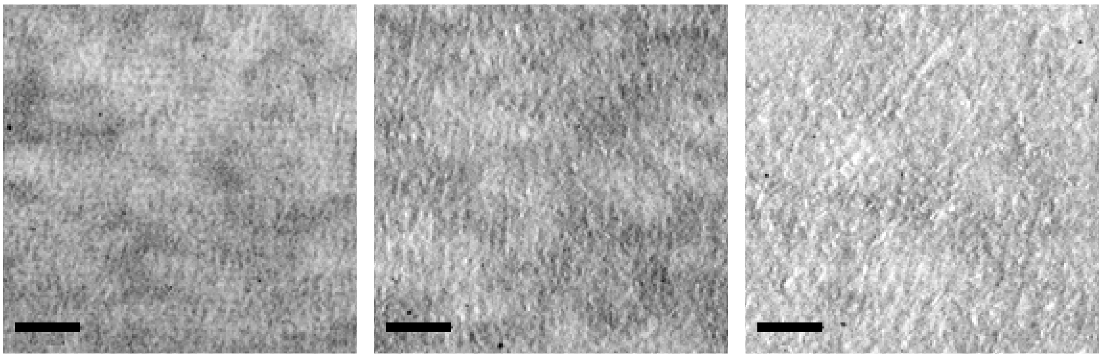

(a) HS sample (Colour 1, 0.1 % FWA). **(b)** HS sample (Colour 2, 0.2 % FWA). **(c)** HS sample (Colour 3, 0.3 % FWA).

Figure 2.33 UV scanner images of blade coated HS samples (19 g/m^2 coat weight) with increasing FWA concentration in the coating color (no FWA in base sheet), scale bar = 2 mm.

Influence of the FWA concentration in the base paper

In commercial coated paper grades the FWA is usually added predominantly into the coating color. Due to the usage of coated broke a small amount of FWA is also contained in the base paper. In the present study, part of the hand sheet samples contained a rather high amount of FWA (1 % Blankophor® PT) in the base paper, resulting in a brightness of 108.38 % compared to 87.85 % for the hand sheets with no FWA. When these hand sheets are coated two contrary mechanisms can occur during UV scanner imaging. On the one hand, the FWA in the coating color generates a signal and on the other hand the excited FWA in the base paper shines through the coating to some extent.

Figure 2.34 shows the coefficient of correlation (R) of UV scanner and burnout test images of the HS samples containing FWA in the base paper. As the correlation is negative in this case and R^2 does not take into account a negative correlation, R has been chosen for visualization of the correlation.

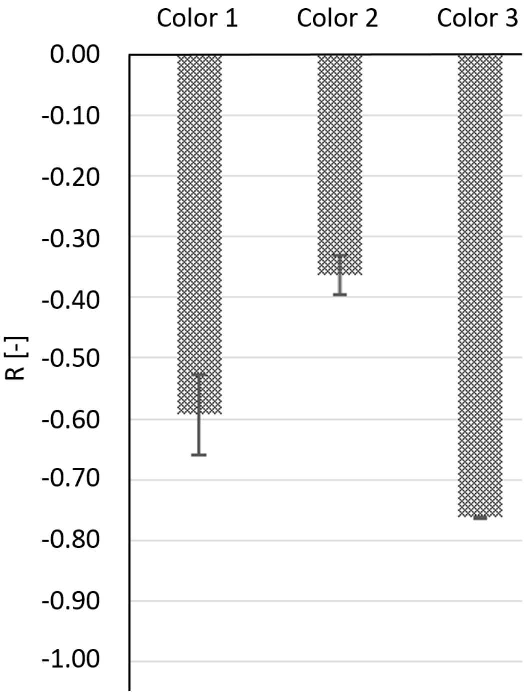

Figure 2.34 *R* of point wise correlation of burnout test - and UV scanner images of HS samples (with 1 % FWA in base paper) coated with Colour 1, Colour 2 and Colour 3.

The negative correlation implies that brighter areas in the UV scanner images correspond to darker areas in the burnout images. The large amount of excited FWA in the base paper seems to shine through the coating layer in regions of lower coat weight. There is no clear trend for the three coating colors with different FWA amounts. In summary it has to be concluded that excessive amounts of FWA in the base paper also has a negative effect on the estimation of the spatial coating layer formation using UV scanner imaging. In order to clarify this observation and to better understand the influence of the FWA content in the base paper, further research has to be carried out.

Evaluation of commercial LWC samples

Four commercial LWC samples were examined and the mean R^2 between UV scanner and burnout test images was 0.77. The coat weight (14 g/m^2) was in the range of the lowest flat-bed rod coated (13 g/m^2). R^2 was lower for the flat-bed rod coated (0.64). One reason for the lower R^2 might origin from the differences between the application and drying (immobilisation) of the industrial coating and the flat-bed rod coater. However, this result demonstrates a high similarity between UV scanner imaging and the burnout test. Therefore, UV scanner imaging seems to be suitable for evaluating the spatial coating layer formation of commercial LWC paper.

Conclusion

A method to capture the spatial coating layer uniformity using UV scanner imaging has been evaluated. It was compared to two reference methods, the widely used burnout test and a direct measurement of local coat weight using β-radiography. The results indicate that this method is only applicable under closely defined conditions regarding applied coat weight and FWA amount in the coating color and the base paper respectively.

For samples with higher coat weights and for samples with high amount of FWA in the coating color or in the base paper, the correlation to the burnout test and the local coat weight maps is poor. For rather high amounts of FWA in the base paper the correlation is even reversed, i.e. brighter regions then indicate lower local coat weight.

A good correlation between UV scanner images, burnout test images and also β-radiography measurements was observed for

- low coat weights ($<19\,\mathrm{g/m^2}$),
- coating colors containing low amounts of FWA and
- base papers containing no to little FWA.

Considering these conditions, UV scanner imaging is an useful tool for a non-destructive and fast evaluation of the coating layer uniformity.

2.9.2 UV LED mounted on IFM

The main reason for introducing another method for assessing the spatial coating layer formation via UV light emission was an inherent drawback of the UV scanner. As described, the fluorescent light source of the UV scanner is located at an angle of about 45° and the detector is located at 90° on the scanning head. Figure 2.35 shows a schematic drawing of the UV scanner light source detector geometry. It is apparent from Figure 2.35 that rough surfaces cause a heavy shadowing artefact. This is due to the topography variations of the sample.

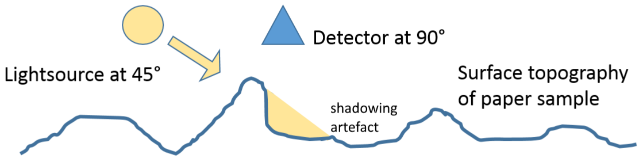

Figure 2.35 Schematic drawing of the UV scanner light source detector geometry.

The impact of this shadowing artefact is depicted in Figure 2.36. One rough office paper sample was scanned in the UV scanner in four different orientations with respect to the motion of the scanning head. The four images were registered, thus, the four areas depicted in Figure 2.36 show exactly the same area of the sample. The fibre orientation of the sample is horizontally in the images. The fibre orientation can be clearly seen when the scanning head moved perpendicular to the fibre orientation (90° and 270°). As a consequence, the obtained data from scanning rough samples is a combination of topography information and FWA information. Due to the presence of the shadowing artefact the complexity of interpreting the results regarding the spatial distribution of FWA increases and thus, rough paper samples should be examined with a different method.

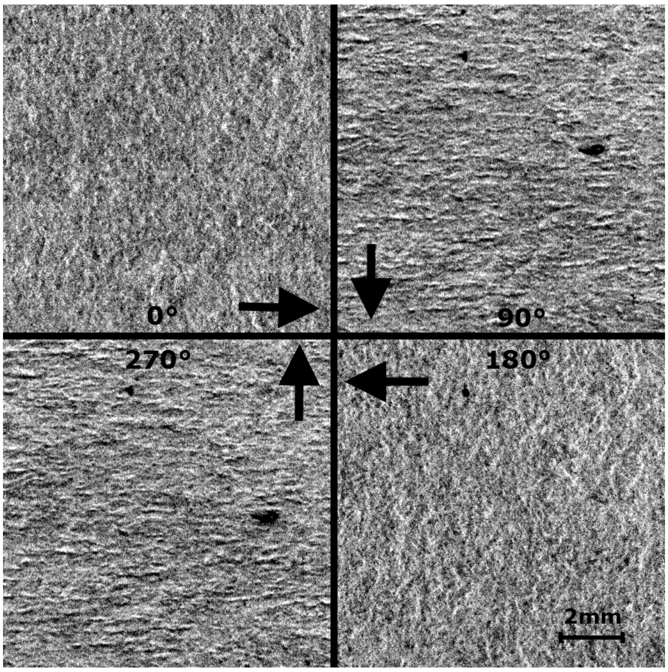

Figure 2.36 UV scanner images of the same rough office paper sample scanned in four different orientations. The arrows indicate the direction of illumination of the scanning head.

Therefore another method for capturing the spatial coating layer formation has been worked out. It is based on the same principle as the UV scanner imaging method. For the novel method eight UV LED were soldered on a round conductor board. The UV LED are emitting light at one peak intensity, 280 nm. The conductor board was subsequently mounted on the 2.5 zoom lens of the IFM. In Figure 2.37 the measuring arrangement for the UV LED mounted on the IFM is shown. The circular configuration of the UV LED acts like a diffuse illumination. The advantages of the UV LED mounted on the IFM are:

- High resolution (depends on the used zoom lens: 3.18 µm/pixel to 25.6 µm/pixel).

- One peak emission at 280 nm.
- No shadowing artefact.

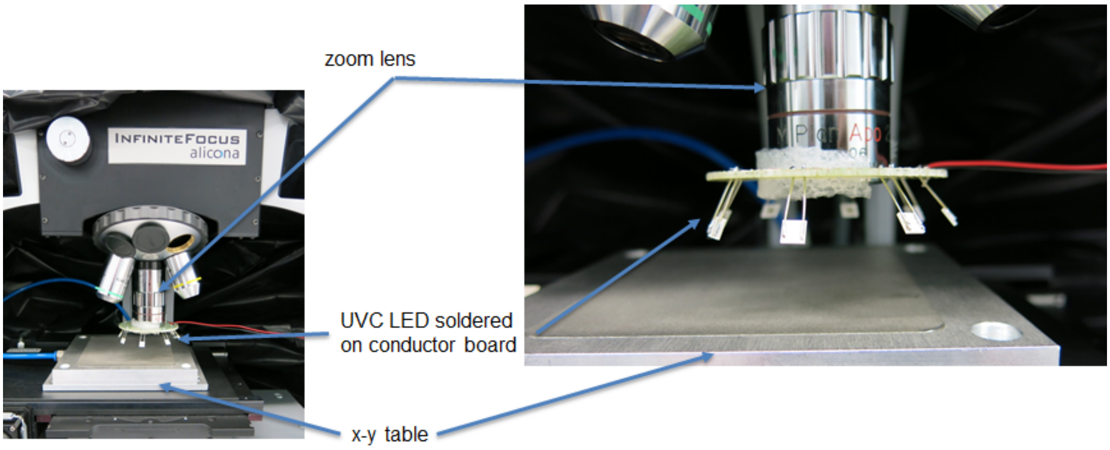

Figure 2.37 Measuring arrangement of the UV LED mounted on the IFM.

The UV LED on IFM method was evaluated in an analogue procedure as the evaluation of the UV scanner imaging method. The reference methods were the burnout test and β-radiography, the absolute measure for coating coverage. The conclusions of the laboratory coating trial were similar to the UV scanner imaging method: the method is highly sensitive to the FWA content in the base paper and the field of application is for coat weights up to 24 g/m^2.

Finally a combined evaluation of the UV scanner imaging method and the UV LED on IFM with the burnout test as a reference method was carried out. The examined samples were commercial samples:

- Coated High Speed Inkjet (HSI) paper: 90 g/m^2 (Coat weight per side: 7 g/m^2)
- LWC paper: 80 g/m^2 (Coat weight per side: 12 g/m^2)
- WFC matte paper: 100 g/m^2 (Coat weight per side: 22 g/m^2)
- WFC reference paper (good print quality): 118 g/m^2 (Coat weight per side: 27 g/m^2)
- WFC reference paper (poor print quality): 170 g/m^2 (Coat weight per side: 37 g/m^2)

The evaluation procedure of three sample per paper grade was the same as explained above, first imaging with the UV methods, performing the burnout test, registration, filtering and subsequently calculation of R^2. The result of the correlation is depicted in Figure 2.38.

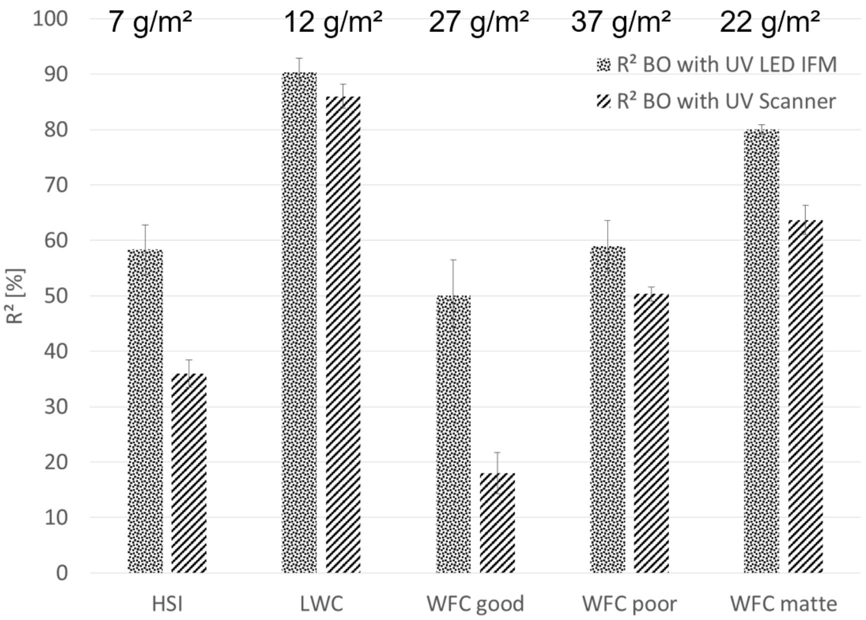

Figure 2.38 R^2 of point wise correlation between UV LED on IFM, UV Scanner with the burnout test. Additionally, the coat weight is displayed on top of the diagram.

It can be seen that the highest correlation between burnout test and the UV methods was achieved by LWC ($R^2 = 90\,\%$). LWC has a low coat weight and usually no FWA in the base paper. When looking at the three WFC grades, the one with the lowest coat weight (i.e. WFC matte) achieved the highest correlation. WFC good and WFC poor are more calendered than compared to WFC matte, however, WFC good is supposed to have good print quality and thus, should exhibit a lower variation in coat weight distribution. This might explain the difference between WFC good and WFC poor.

The HSI sample exhibited the highest roughness and a significantly high amount of FWA in the base paper. The correlation was similar to the correlation found in Section *Influence of FWA concentration in the base paper*. The point wise correlation between UV LED on IFM, UV scanner and burnout test images was negative as can be seen in Figure 2.39. Brighter areas on the burnout test image correspond to darker regions in the UV LED and UV scanner image, see ellipses in Figure 2.39. Thus, the FWA shines through the coating layer and in high coat weight areas the upwards travelling light is hindered. Summarising this evaluation, it can be said that UV LED on IFM tends to better correlate with the burnout test.

Due to the advantages of the method, not only the measurements for the rough paper samples (e.g. pigmented office paper) were conducted with the UV LEDs on the IFM, but for all other paper grades (e.g. WFC paper grades) as well. The chosen pixel size was 25.6 µm/pixel with the 2.5 zoom lens.

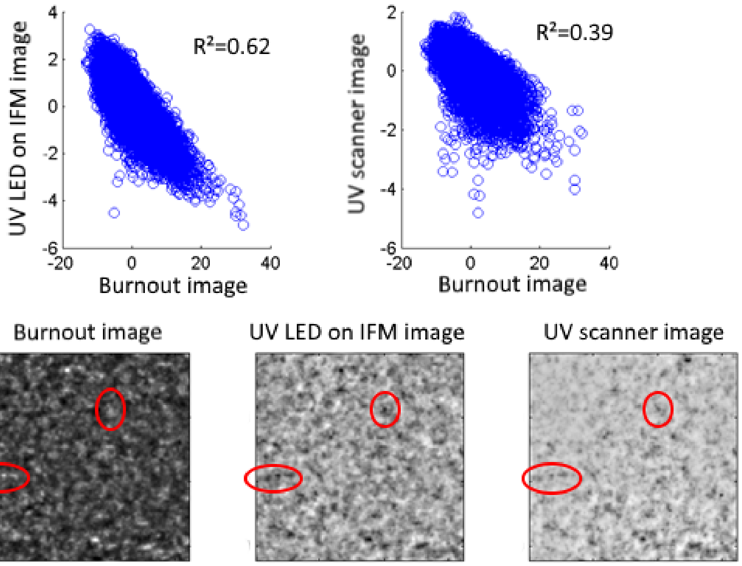

Figure 2.39 Scatter plots of the point wise correlation between burnout test images an UV LED on IFM and UV scanner images of one HSI sample. Images of the measurements are below the scatter plots, size of images 40 mm × 40 mm.

2.10 ATR IR Spectroscopy

Attenuated total reflection infra red (ATR IR) spectroscopy is one of the most commonly used techniques of surface analysis in the field of paper science. The main reason for that is that the sample preparation is very fast and simple (Preston, 2009). Aim of the ATR IR measurements is to analyse the coating surface composition ((Hiorns et al., 2006)) and especially the surface latex uniformity (Chattopadhyay et al., 2012; Halttunen et al., 2003; Kenttä et al., 2000, 2006).

The principle of ATR IR spectroscopy is depicted in Figure 2.40. It is based on the attenuation of the total internal reflection of an incident infra red (IR) beam in the so called ATR crystal (e.g. a Germanium crystal with n_1). According to Snell's law (see Equation 2.32 in Section 2.8 *Polarised Light Reflectometry*) total internal reflection occurs when the incident angle α exceeds the critical angle which depends on the refractive indices of the media (see Equation 2.39).

$$\sin \alpha_{critical} = \frac{n_2}{n_1} \tag{2.39}$$

When the incident IR beam is reflected at the interface of a medium with a lower refractive index (n_2), the amplitude does not immediately decreases to zero beneath the interface. The amplitude rather exponentially decreases to zero while entering the second medium. This decay is also known as evanescent wave. The reversal point of the evanescent wave is defined as the penetration depth d_p and is calculated according to Equation 2.40 (Pedrotti, 2005):

$$d_p = \frac{\lambda_0}{2\pi\sqrt{n_1^2 \sin^2 \alpha - n_2^2}} \tag{2.40}$$

where λ_0 is the wavelength of the incident IR beam, n_1 is the refractive index of the ATR crystal, n_2 is the refractive index of the second medium. Typical penetration depths for coated paper are <2 µm (Hiorns et al., 2006; Kenttä et al., 2006).

Besides the part of the energy of the incident IR beam entering the medium the other part of the wave travels parallel to the surface of the medium with the higher refractive index. After travelling a certain distance the IR beam is finally reflected. The phenomenon of lateral displacement of the incident energy is named after the discoverers Goos-Hänchen (Goos and Hänchen, 1947).

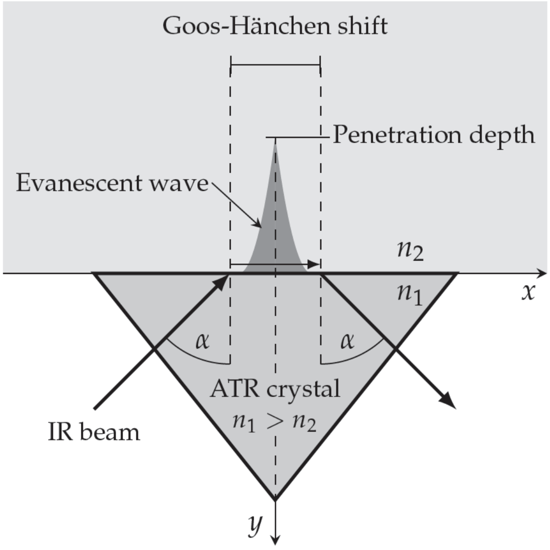

Figure 2.40 Measurement principle of attenuated total reflection infra red (ATR IR) spectroscopy (adopted from Obradovic et al. (2007)).

The ATR IR Spectrometer used for the analysis of binder distribution in this thesis was a Bruker *Tensor 27* (Bruker Corporation, Billerica, MA, USA) with a *Hyperion 3000* FT-IR microscope. The mounted ATR crystal, a Germanium Crystal, was a 20x zoom lens and the detector was a single element mercury cadmium telluride detector. The size of the examined area was 9.60 mm × 7.80 mm. The tip size of the ATR crystal was 200 µm resulting in a pixel size of 200 µm. At this settings the measurement took 866 min (i.e. approximately 15 hours). In Figure 2.41 a 2D latex intensity map of a wood free coated paper sample is depicted. The higher the intensity, the higher is the latex amount in a specific data point.

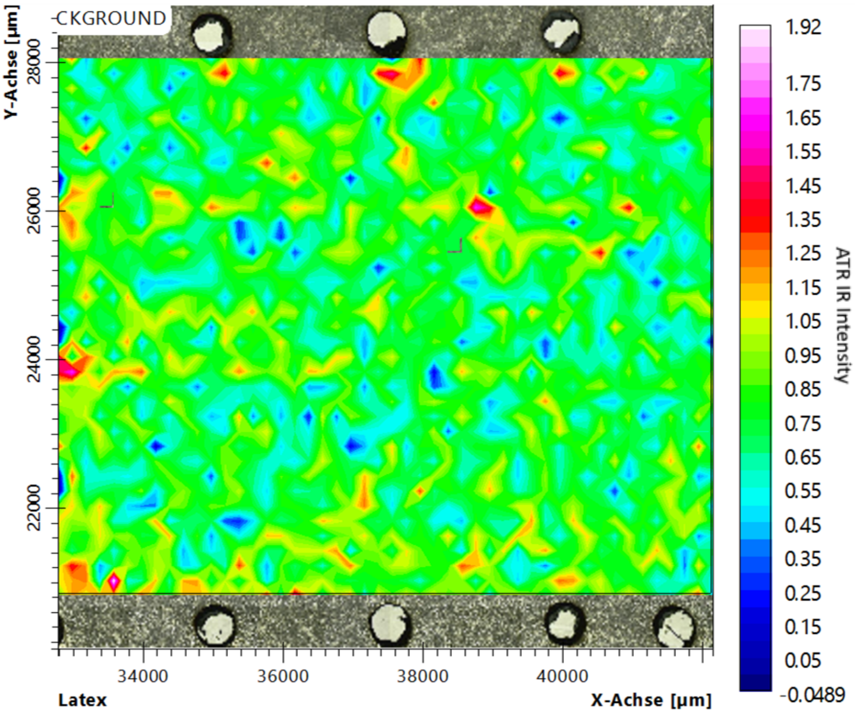

Figure 2.41 Example of an ATR IR map obtained from a wood free coated paper grade.

For examination of latex surface uniformity in the coating layer of paper wavenumber bands from literature were taken as basis. In Table 2.2 the various wavenumber bands from the literature and in the last line the wavenumber bands chosen for the examinations in this thesis are enlisted. The characteristic wavenumber for SB latex was the CH band (wavenumber $3006\,\mathrm{cm}^{-1}$ to $2820\,\mathrm{cm}^{-1}$), for calcium carbonate the CO_3^{2-} band (wavenumber $890\,\mathrm{cm}^{-1}$ to $850\,\mathrm{cm}^{-1}$) and for kaolin the SiO (wavenumber $1055\,\mathrm{cm}^{-1}$ to $980\,\mathrm{cm}^{-1}$) and the OH bands (wavenumber $3725\,\mathrm{cm}^{-1}$ to $3670\,\mathrm{cm}^{-1}$) respectively.

For repeatable results a certain pressure has to be applied to the ATR crystal during the measurement. Nevertheless, the obtained signal depends on the contact area

Table 2.2 Wavenumber bands from literature and the wavenumber bands chosen.

In [cm^{-1}]	SB Latex	Carbonate	Kaolin
Halttunen et al. (2003)	760 & 3025	874 & 1790	3700-3600
Kenttä et al. (2006)	3150-2800	875	3690
Chattopadhyay et al. (2012)	2920	2512	3690
This work	3006-2820	890-850	1055-980 & 3725-3670

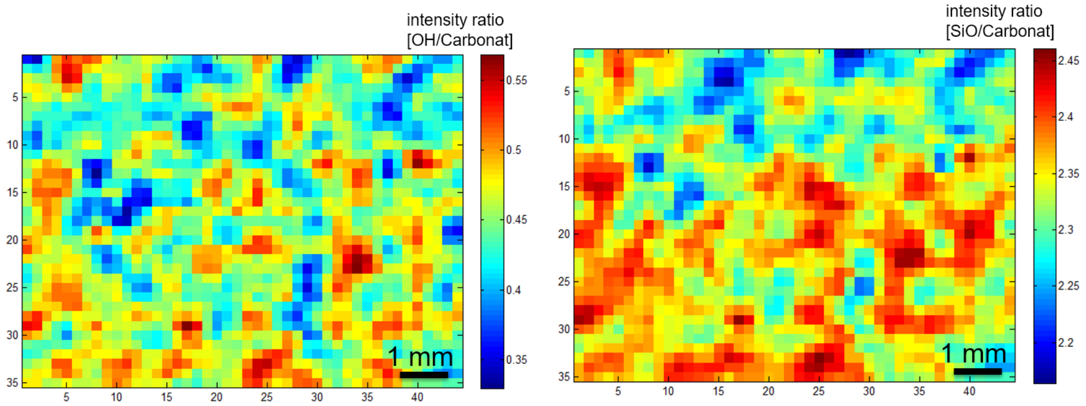

(a) Intensity ratio of OH band to carbonate band.

(b) Intensity ratio of SiO band to carbonate band.

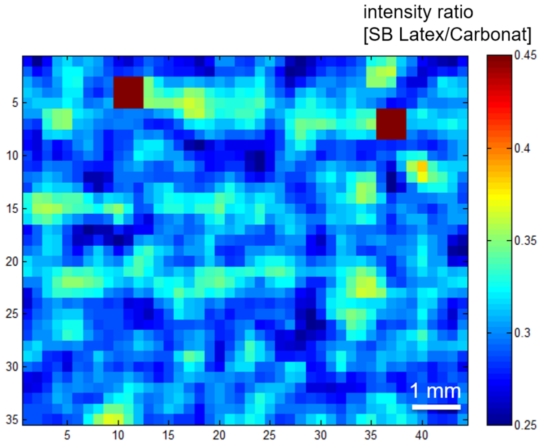

(c) Intensity ratio of SB latex band to carbonate band.

Figure 2.42 2D ATR IR intensity ratio maps of kaolin **(a)** OH band and **(b)** SiO band, respectively and in **(c)** the ratio map of SB latex, denominator was the intensity map of the carbonate band.

(i.e. surface roughness) of the ATR crystal and measured sample. The signal is the product of contact area and absorption intensity, the higher the contact area, the higher is the absorption intensity. Thus, by calculating the ratio of two signals the influence of the contact area can be eliminated (see Eq. 2.41). Within this thesis the calcium carbonate signal was chosen as reference basis to eliminate the influence of the contact area.

$$\frac{\text{Signal 1}}{\text{Signal 2}} = \frac{\text{Absorption intensity 1} * \cancel{\text{Contact area}}}{\text{Absorption intensity 2} * \cancel{\text{contact area}}} \tag{2.41}$$

Figure 2.42a and 2.42b show both the ratio of the kaolin (OH band and SiO band) intensity to the calcium carbonate intensity. It can be seen that both images exhibit similar features and structures. Thus, both intensity ratios give information regarding kaolin distribution on the coated paper.

Figure 2.42c illustrates the ratio of SB latex intensity to the calcium carbonate intensity. The obtained structures are in the millimeter range and indicate a variation in the surface latex content of the sample. The two spots exhibiting a high intensity were identified as dirt specks. These dirt specks act as outliers in the multiple linear regression analysis, thus every sample has to be visually checked before statistical analysis. However, the ATR IR method applied, seemed to give relevant information regarding coating coverage and surface latex distribution.

Chapter 3

Print Unevenness in Xerography

3.1 Xerographic Printing

Xerography, belongs to the group of digital printing technologies and was discovered at the end of the 1930s by Chester Carlson. The first laser printer was developed in the middle of the 1970s.

The xerographic printing process comprises of six main steps (Duke et al., 2002). In Figure 3.1 the six steps are illustrated. First **(1)**, the photoconductive belt or drum (i.e. photoreceptor) is negatively charged. During this step the photoreceptor is evenly charged with a fine tungsten wire operated at high voltage. This is due ionisation of the air in the vicinity of the wire.

The second step **(2)** is the exposure of the photoreceptor. During this step a latent image is formed by a laser or LED. Everywhere the beam strikes the photoreceptor, it is discharged. Usually the discharged areas correspond to the black areas in a monochrome image.

After exposure of the photoreceptor, the image is subsequently developed **(3)**. The development roll carries the so called developer into the vicinity of the photoreceptor. The developer consists of the toner (size: 5 µm to 10 µm) and a carrier (i.e. typically a ferrite with a size of 100 µm). The toner used in xerographic can be divided into two groups: liquid and dry toner. The main components of a toner are enlisted in Table 3.1. The carrier forms a brush and the electrical field moves the developer from the developer roll onto the exposed areas of the photoreceptor.

In the transfer step **(4)** the toned image on the photoreceptor substrate is transferred to the printing substrate (i.e. paper). Within this step the paper is charged with a corotron (i.e. corona discharge unit). It is important that the detachment field overcomes the toner adhesion to the photoreceptor to ensure that the entire toned image is transferred to the paper.

Table 3.1 Components of xerographic toner (e.g. dry toner) (Duke et al., 2002).

Component	Purpose
surface additives	toner flow & charge control
charge control agents	control sign, level and rate of charging
internal waxes	substitions of fuser oil
polymer binder	transport of pigment & fix pigment to substrate
pigments	converts polymer pattern into visible image
magnetite	dirt control & magnetic ink character recognition

In the next step the toner is permanently fixed on the paper in the fuser **(5)**. This is usually performed by applying heat and/or pressure. The heated fuser roll melts the polymer binder in the toner and ensures fixation to the paper. Thus, the toner particles on the surface of the sheet are melted by raising the surface temperature beyond the toner glass transition point. The melting temperature can be around 110 °C to 120 °C. The fuser rolls are sometimes coated with a silicon oil to prevent the paper and the toner from sticking to the rolls.

Finally the photoreceptor has to be cleaned **(6)** before starting a new cycle. Therefore, the photoreceptor is excessively exposed by a suitable light source to neutralise the charge. Subsequently a brush or blade collects the remaining toner for recycling purposes. After this step the photoreceptor is ready for repeated charging.

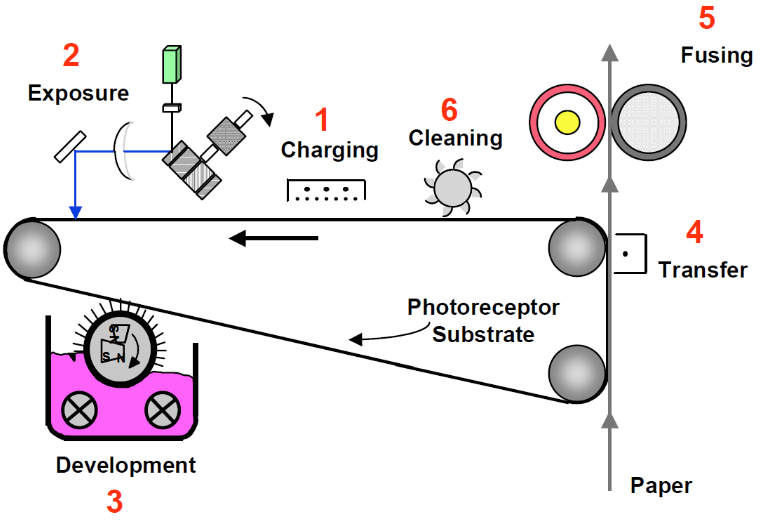

Figure 3.1 Schematic diagram of the six steps of the xerographic printing process (Duke et al., 2002).

3.2 Print Unevenness in Xerography

The first time the paper comes into contact with the toner is in the transfer unit (i.e. **(4)** in Fig. 3.1). During this step, electrically charged toner particles are transferred to the paper by an electrostatic field. Thus, the electrical and dielectric properties of paper are very important for xerographic printing (Alava and Niskanen, 2006; Backfolk et al., 2010). If the conductivity of a paper is to high, loss of image density might occur because of charge leakage. If a paper is too resistive, there might occur handling (i.e. stacking) problems due to static electricity (Green, 1981; Sirvio et al., 2008).

A lot of research has been carried out in order to characterise the electric and dielectric properties of a paper sample (Backfolk et al., 2010; Brodie et al., 1968; Maldzius et al., 2010; Rutar and Scheicher, 2009; Simula et al., 1999; Sirvio et al., 2009). The main outcome of the investigations was that the electrical and dielectric properties of paper depend on the moisture content, the temperature and the composition (e.g. coating colour, filler content, base paper grammage, salt concentration) of the paper as well as the applied electrical field strength. Variation of these properties might cause print unevenness.

Green (1981) concluded that not only electrical properties and moisture content but paper properties such as smoothness, stiffness and porosity might influence the print quality in xerographic printing.

After the transfer unit **(4)**, the toner is fixed to the paper in the fusing section (i.e. **(5)** in Fig. 3.1). The exposure of the paper to a transient thermal pulse might cause curling (i.e. dimensional change of paper, also caused by two sidedness or fibre orientation) and as a consequence lead to paper jams in the printer (Lavrykov et al., 2013). Thus, besides electrical and dielectric properties, the thermal properties such as thermal conductivity, thermal contact resistance and specific heat capacity are important regarding xerographic printing.

It was shown by Gerstner and Gane (2010) that modifying the composition of the coating colour with respect to thermal properties partly influences the toner adhesion and thus, the final print quality (e.g. print mottle). They also showed, that increased fusing roll temperature increases print gloss. Liang et al. (2012) also studied the variation of coating formulation with respect to thermal properties. In their work they found no clear correlation between print unevenness (i.e. evaluated by visial ranking test) and thermal conductivity. However, they concluded that the porosity of the coating is a key parameter for adjusting the thermal conductivity. Accordingly the latex concentration in the coating colour plays a significant role because it determines the porosity of the coating layer. Besides porosity, Sanders et al. (1996) found in their experiments with various sizing agents (i.e. AKD, ASA and starch) and fillers (i.e. clay and calcium carbonate), that the surface energy also plays a role. The higher the surface energy, the better was the toner adhesion.

Lavrykov and Ramarao (2012) examined the thermal paper properties and the results showed that thermal conductivity and specific heat capacity were mainly dependent on the filler content of the paper and the sheet density. In addition, it was found that the thermal contact resistance depends on the surface roughness.

Sirvio and Backfolk (2008) investigated the effect of roughness (i.e. PPS roughness) of light weight coated papers on print mottle in xerography. The samples were coated with three target coat weights: $6\,\mathrm{g/m^2}$, $9\,\mathrm{g/m^2}$ and $12\,\mathrm{g/m^2}$. The samples were printed in a commercial colour printer with four colours (i.e. cyan (C), magenta (M), yellow (Y) and black (K)). Print mottle was analysed for 100 % tone value fields via wavelet analysis. Finally a single print mottle value was calculated by a weighted average of several bandwidths. This weighting was based on the sensitivity of the human visual system to different size defects.

Generally, Sirvio and Backfolk (2008) concluded that increased roughness led to higher print mottle. Samples with lower coat weight exhibited higher roughness, whereas samples with higher coat weight had a lower roughness. Thus, lower coat weight resulted in a higher print mottle and vice versa. In addition to that, the influence of calendering was examined. As expected, calendering reduced the roughness and accordingly calendering of the samples led to lower print mottle.

Finally the effect of transfer voltage was evaluated with a test printer. In the optimum voltage range, the print mottle behaviour was the similar compared to the commercial printer. For too low voltages the toner transfer was insufficient due to too low or no charge density on the paper surface. Too high voltages generated periodical lines due to vibrations or mechanical stress when the sheet was separated from the photoconductor.

Juric et al. (2014) investigated the effect of surface roughness of coated and uncoated paper samples on print mottle in xerographic printing. The paper samples used, had a basis weight of $250\,\mathrm{g/m^2}$ and were printed with four colours (i.e. C: 65 %, M: 50 %, Y: 50 % and K: 50 %). They used texture analysis (see Section 2.1 Registration) for evaluation of print mottle. Conversely to Sirvio et al. (2008) the conclusion was, that the paper samples having a higher roughness (i.e. uncoated samples) exhibited a lower print mottle.

Chen et al. (2012) investigated the effect of various paper properties on print quality attributes (i.e. print mottle and print surface roughness) for ten commercial uncoated paper grades and for three xerographic printers. The basis weight of the samples was in the range of $77\,\mathrm{g/m^2}$ to $121\,\mathrm{g/m^2}$. The measured paper properties were caliper, roughness (i.e. PPS roughness), surface topography (i.e. mechanical stylus profilometry), brightness, opacity, Young's modulus, porosity (i.e. Gurley), Hercules Size Test and gloss. Print mottle was analysed for tone value 100 % black colour. Instead of wavelet analysis as used by Sirvio et al. (2008), a Fast Fourier Transform (FFT) based analysis was chosen for different wavelength bands. Additionally to the FFT analysis, a visual ranking analysis was performed. It was found that print mottle

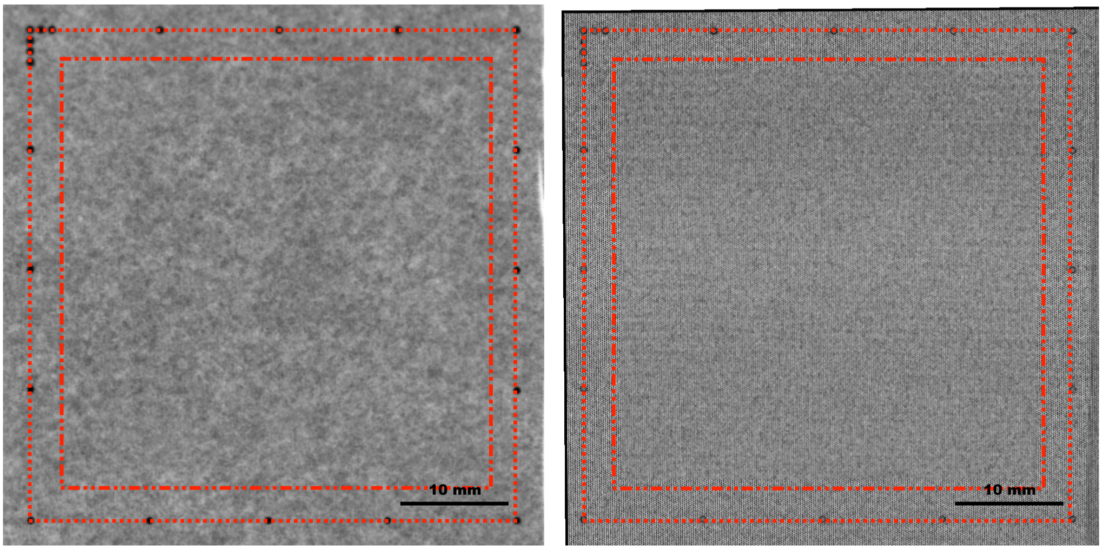

(a) β-radiography image.

(b) Image of xerographic print with tone value 30 %.

Figure 3.2 Exemplary image of a data map obtained from **(a)** β-radiography and **(b)** printed with 30 % tone value black. The outer dashed square indicates the size defined by the laser marks (45 mm × 45 mm) and the inner dashed square defines the size of examined area (40 mm × 40 mm).

in the wavelength band of 0.1 mm to 1 mm highly corresponded to the visual ranking test (R^2 of 0.96). However, this wavelength band is below the standard wavelength band of 2 mm to 8 mm or 1 mm to 16 mm (Johansson, 1993).

Multivariate analysis of the measured paper properties with respect to the visual ranking test revealed that the five most important paper properties were brightness, opacity, basis weight, gloss and PPS roughness.

3.3 Paper Samples and Xerography Printer

For examination of print mottle two commercially available papers were used (i.e. marked as paper grade **A** and **B** respectively). Both paper samples had a basis weight of 80 g/m^2. The paper grades were marked as special xerography printing grades. The samples had a size of 45 mm × 45 mm. Figure 3.2 shows two registered data maps (Fig. 3.2a: β-radiography image and Fig. 3.2b: printed sample with 30 % tone value black). The size of the examined area was 40 mm × 40 mm in order to avoid interfering influences from the laser holes.

For printing of the samples two commercially available xerographic printers were used. The first printer was a four colour Canon C5030i printer (Canon Austria GmbH, Austria) with a printing speed of 30 pages per minute (denoted as **Printer 1**). The second printer was a black colour HP LaserJet P2055x printer (HP Germany GmbH,

Table 3.2 Measured local paper properties for xerography samples.

Paper Property	Unit	Device	Resolution [µm/pixel]
Basis Weight	[g/m^2]	β-radiography	50.00
Gloss	[%]	Imaging Reflectometer	200.00
Macroroughness	[-]	Imaging Reflectometer	200.00
Brightness	[GV image]	IFM (imaging mode)	25.60
Opacity	[%]	IFM (imaging mode)	25.60
Topography	[µm]	IFM	12.80
Thickness Variation	[µm]	IFM	12.80

Germany) with a printing speed of 33 pages per minute (denoted as **Printer 2**). In pre-trials the most critical black monochrome tone values regarding print unevenness were determined, by means of visual ranking analysis. The four tone values most critical were 30 %, 50 %, 75 % and 100 %. In Figure 3.3, the 30 % to 100 % tone value printed with the Canon C5030i are depicted. The pre press settings for the tone values were taken from grey scale values of the printer settings in GIMP 2.8.16 (GIMP, GNU Image Manipulation Program). Thus, the printer settings were identical for all printed paper samples, but the final print density (e.g. measured with a GretagMacbeth Densitometer) was not exactly the same for two different paper grades.

For evaluation of print unevenness three samples were measured and printed for each tone value. The print reflectance was measured with the IFM in the imaging mode with diffuse illumination conditions and a 2.5 zoom objective with a pixel size of 25.6 µm/pixel. The exposure time was adjusted to each tone value. Thus, overexposure and underexposure was avoided. The exposure time for the 30 % tone value: 180 ms, for the 50 % tone value: 350 ms, for the 75 % tone value: 500 ms and for the 100 % tone value: 800 ms.

Before printing all the local paper properties of the paper samples were measured. The properties, the used measurement devices and the obtained pixel size are listed in Table 3.2, the measurement techniques are described in Section 2. After measurement of the local paper properties, the samples were placed on sample holders. The sample holders were A4 paper sheets where a hole with the size of one sample was cut out. The samples were then fixed to the sample holder with adhesive tape (i.e. Scotch Tape^{TM}). Finally the samples were placed in the printer and printed with the particular tone value. The subsequent registration and image handling procedure and the multiple linear regression analysis was in accordance with the procedure explained in Section 2.1 Registration and Section 2.2 Multiple Linear Regression Analysis.

3.4 Results of Print Trials

The result plots shown in this section are all based on the result plots described in Section 2.2 Multiple Linear Regression Analysis. Each result plot represents the

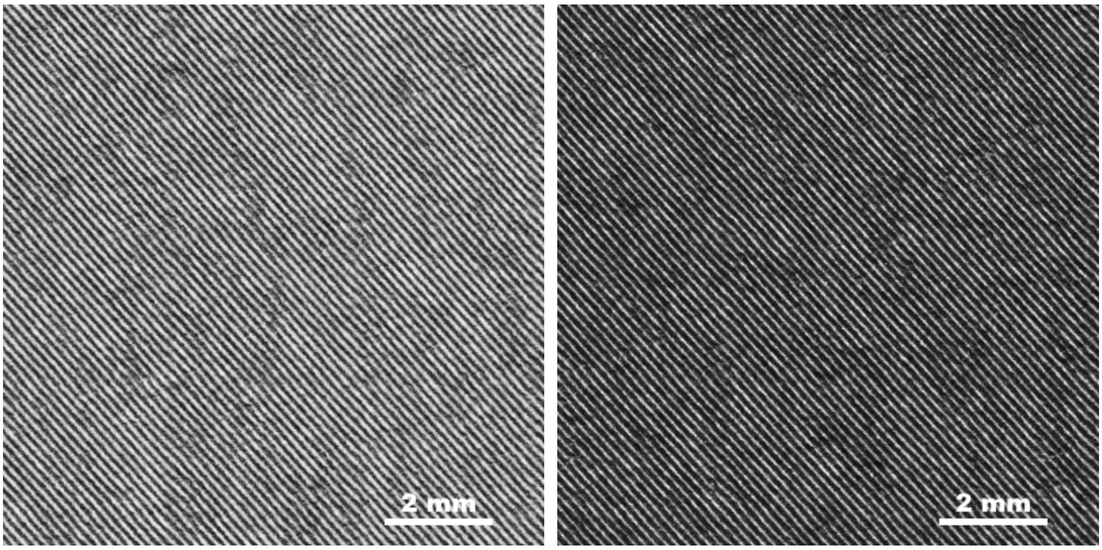

(a) 30 % tone value. **(b)** 50 % tone value.

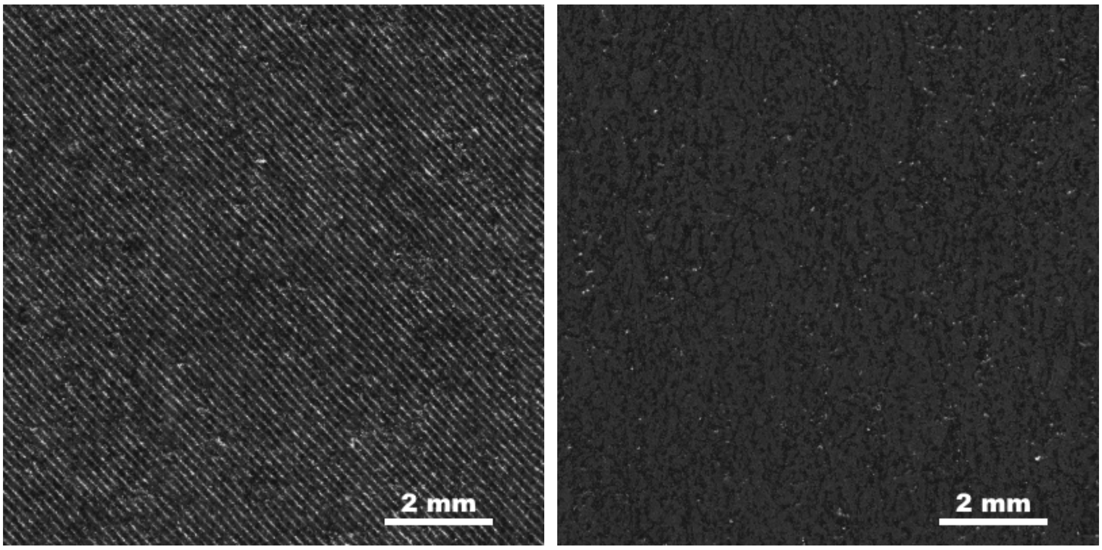

(c) 75 % tone value. **(d)** 100 % tone value.

Figure 3.3 30 % to 100 % tone value printed with the Canon C5030i.

data with respect to the particular tone value. For example Figure 3.4 shows the combined result of the multiple linear regression analysis of the 30 % tone value black for paper grade **A** and **B** as well as for **Printer 1** and **Printer 2**. In Figure 3.4, the first three bars of each of the seven predictors (i.e. basis weight, topography, brightness, gloss, opacity, thickness variation and macroroughness) represent the r^2_{alone} between the predictors and the print reflectance for paper grade **A** printed on **Printer 1**. The next three bars of each predictor represent the r^2_{alone} of the predictors and the print reflectance for paper grade **B** printed on **Printer 1**. The following six bars represent

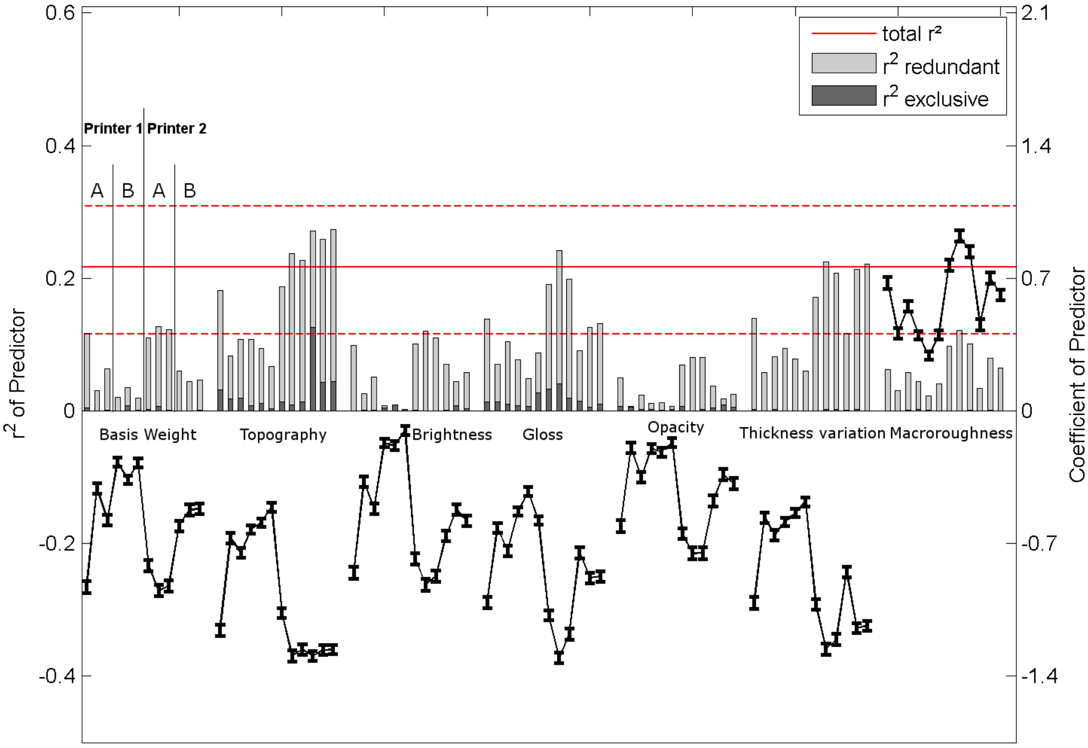

Figure 3.4 Result plot for 30 % tone value black. For each printer and each paper grade three samples were examined. Thus, 12 models with 7 predictors are presented by this plot.

paper grade **A** and **B** printed on **Printer 2**. The error bars in Figure 3.4 represent the coefficients of the predictors b with a confidence interval α of 95 % (right axis of result plots). The detailed description of b and r^2_{alone} is described in Section 2.2.

The solid red line in Figure 3.4 indicates the mean *total* r^2 of all 12 models and the dashed red lines show the minimum and maximum *total* r^2 of the models. Thus, the mean *total* r^2 of the two printers and the two paper samples is 21.73 %, the maximum *total* r^2 is 0.31 (i.e. paper grade **B**, **Printer 2**: last group of bars in Fig. 3.4) and the minimum *total* r^2 was 0.12 (i.e. paper grade **A**, **Printer 1**: second group of bars in Fig. 3.4).

The coefficients of the predictors b in Figure 3.4 show that all predictors except macroroughness are negatively correlated to the print reflectance. Figure 3.5 illustrates the orientation (positive or negative) of b. For example, from Figures 3.5c and 3.4 it is apparent that high values of print reflectance corresponded to low values of brightness. High values of print reflectance represent brighter regions on the printed sample. Similarly high values of brightness represent brighter regions on the sample. The reason for that lies in the analysed 8 bit gray scale images. An 8 bit gray scale image has 256 values where 0 is black and 255 is white. Thus, b shows that brighter

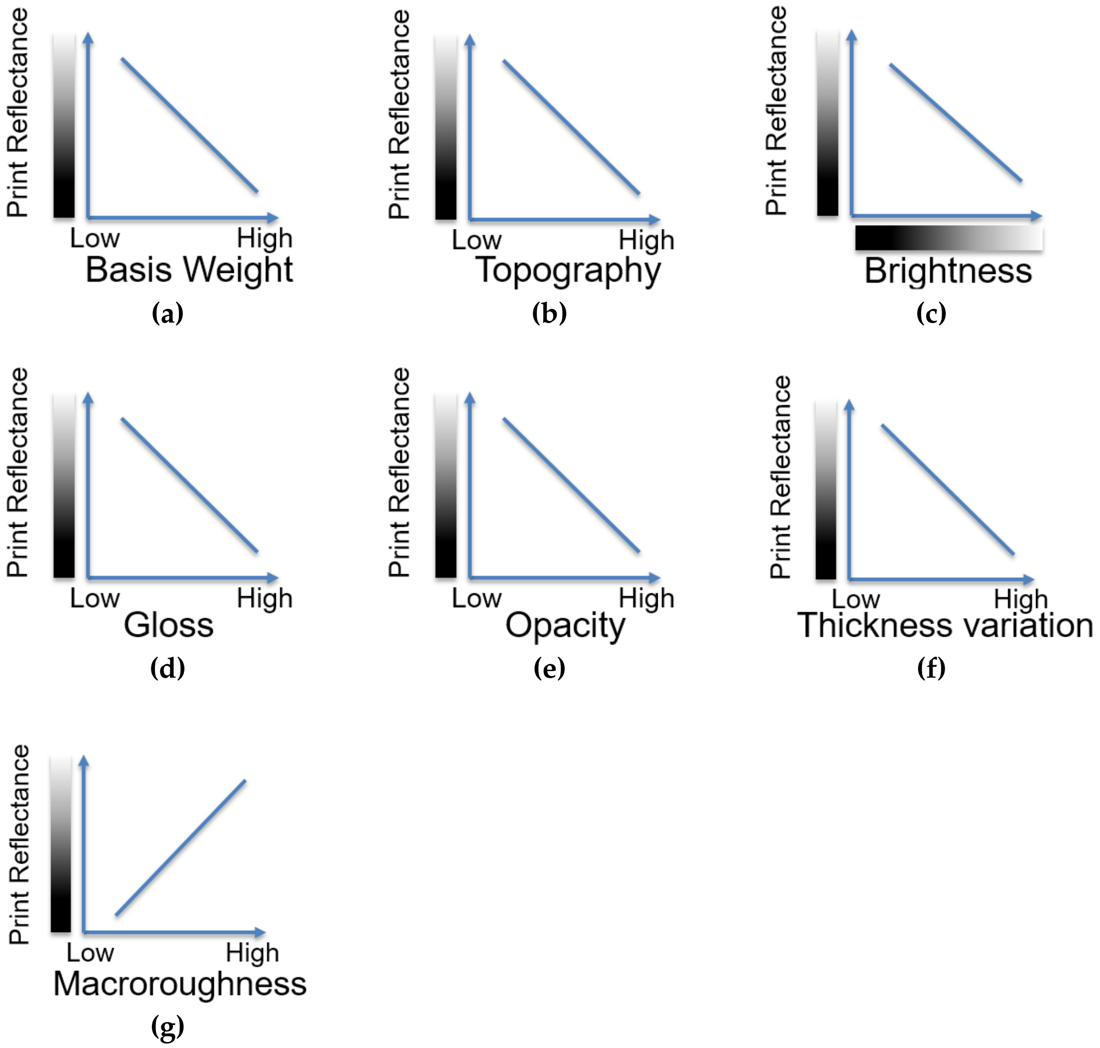

(a) (b) (c) (d) (e) (f) (g)

Figure 3.5 Illustration of the orientation of the coefficient of the predictor between each predictor and print reflectance shown in Figure 3.4.

regions of the sample without print were correlated to darker regions on the print. Another influencing factor is, the optical dot gain also known as the Yule Nielsen effect, which is caused by lateral light scattering in the paper and thus decreases print reflectance and increases print density (Namedanian et al., 2014).

For the predictor basis weight (Fig. 3.5a and first predictor in Fig. 3.4) it can be seen, that regions having a higher basis weight exhibited lower print reflectance than regions of lower basis weight. Similarly, elevated regions (i.e. high values in the topography image) corresponded to lower print reflectance. This might be because elevated regions received more toner than subjacent regions, but print reflectance must not be directly correlated with toner amount (e.g. optical dot gain). However, this result seemed to be plausible, because toner transfer efficiency might be higher on elevated regions and regions of higher basis weight due to better fixation of the toner. Locally higher basis weight and elevated regions corresponded to locally thicker areas. Thus, the orientation of b for thickness variation was the same as for basis weight and topography. An analogue effect arises from gloss and macroroughness. Elevated regions were more calendered and a higher gloss corresponds to lower the macroroughness and lower print reflectance.

When comparing all the predictors, topography, gloss and thickness variation contribute most to the *total* r^2. It can be seen from Figure 3.4, that in the present model topography and gloss also exhibited exclusive information (i.e. indicated by the darker parts of the bars). Accordingly, the amount of redundant information for the other predictors was rather high. Hence, most information provided by one predictor was also present in another predictor. For example the predictor thickness variation comprising the topography of the top side and bottom side of the sample. Thus, thickness variation is highly correlated to the topography. On the other hand it can be observed, that the topography of the bottom side of the sample and furthermore the calculation of thickness variation does not improve the model. As a consequence the fully redundant predictors such as brightness, opacity, thickness variation and macroroughness can be removed from the model without considerable loss of *total* r^2. Local basis weight was not removed from the model, because basis weight as a fundamental paper property is responsible for development of many other paper properties like thickness – and gloss variation and therefore, the influence on final print unevenness is of utmost interest. Still, the direct contribution to the model for tone value 30 % was rather low.

Figure 3.6 depicts the result of the reduced model. Comparison of the mean *total* r^2 in Figure 3.4 and Figure 3.6 reveals, that removal of the four highly redundant predictors did not relevantly decrease the *total* r^2, namely from 0.22 to 0.20. Thus, reduction of the model seems legitimate. By eliminating the redundant predictors, the exclusive amount of the remaining predictors increases. The residual redundancy can be explained with the relationship between basis weight, topography and gloss. Local basis weight distribution is strongly correlated with local topography. Areas of higher basis weight are elevated and also thicker. This exposed regions receive more pressure during calendering and thus, have higher gloss. With respect to print unevenness a lower variation in this three parameters, especially topography will cause a more even printed image.

From Figure 3.6 it can be deduced that local topography explains the print unevenness for **Printer 2** to a higher extend than for **Printer 1**. It can be speculated that there were differences in the transfer section or fusing section between the two printers. If the applied pressure in **Printer 1** was higher, the variation in local topography could have been equalised and thus, diminishing the influence. This applies also for local gloss variations.

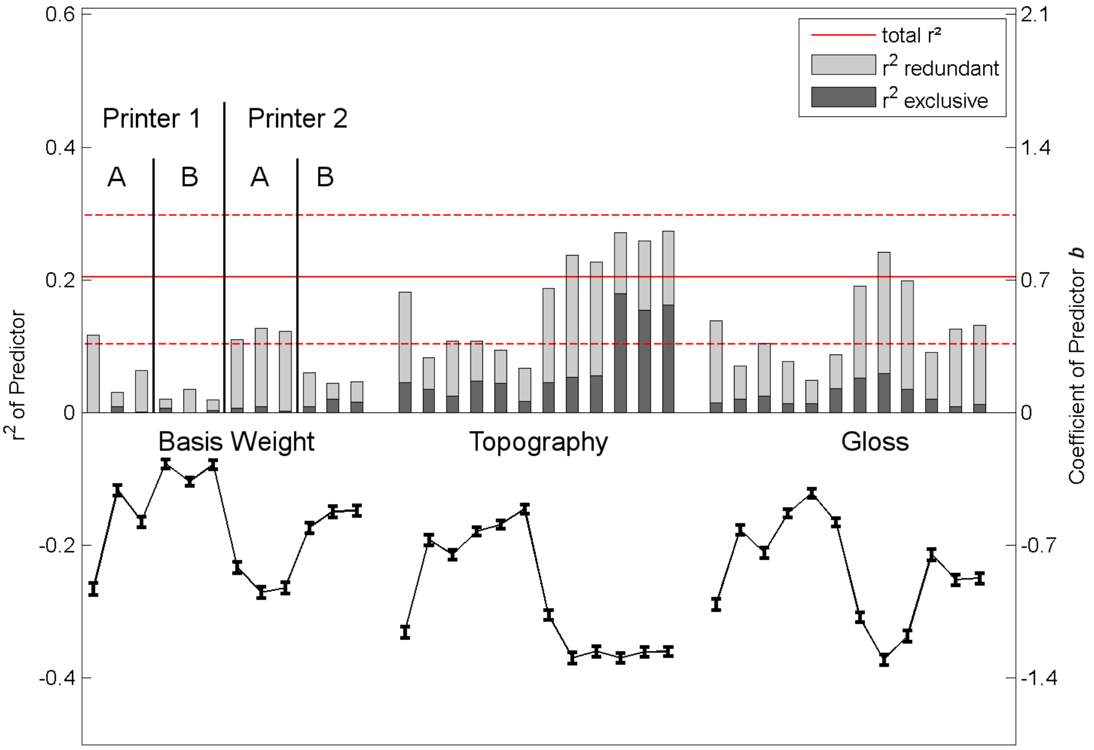

Figure 3.6 Reduced model for tone value 30 %.

Figure 3.7 shows the reduced model plot for tone value 50 %. The mean *total* r^2 (i.e. solid red line) of the two printers and the two paper samples is 0.30, the maximum *total* r^2 is 0.39 (i.e. paper grade **B**, **Printer 1**: fifth bars in Fig. 3.7) and the minimum *total* r^2 is 0.23 (i.e. paper grade **A**, **Printer 2**: ninth bars in Fig. 3.7). In comparison to the mean *total* r^2 of 0.20 of tone value 30 %, the local paper properties explained about 10 % more of the variance in print reflectance in the 50 % tone value. Anyway, the orientation the coefficient of the predictor b is equal to the models of 30 % tone value. Hence, the interpretation of b is analogue to the 30 % tone value.

The contribution of all three predictors was generally higher compared to the 30 % tone value. With higher toner amount on the paper, the variation in surface properties such as topography and gloss became more important for print unevenness. Similarly to the findings of Juric et al. (2014) who found that roughness was a key factor, topography explained most of the variation in print unevenness. Local basis weight remained nearly fully redundant (i.e. no to little $r^2_{exclusive}$), because all the information provided by basis weight was also contained in the two predictors topography and gloss. Figure 3.7 shows, that there is a difference between the paper grades **A** and **B** as well as between the two printers. For example, the contribution of local basis weight for paper grade **B** in **Printer 2** is lower compared to the other paper and printer com-

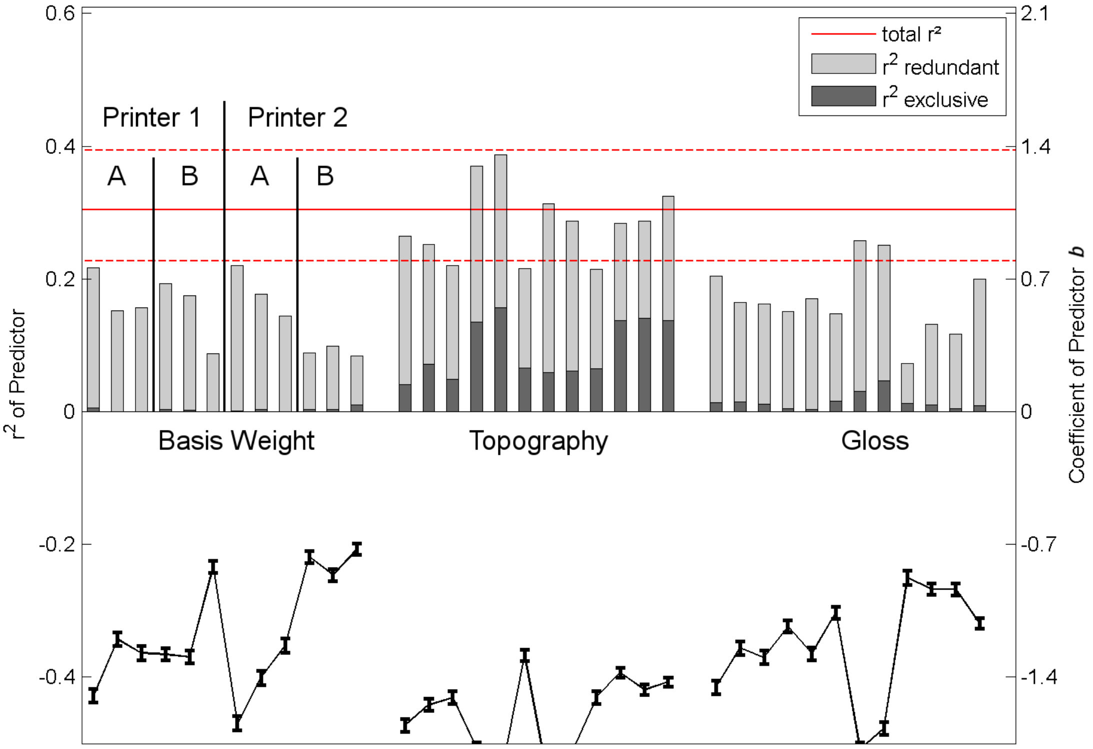

Figure 3.7 Reduced model for tone value 50 %.

binations. This indicates, that the performance of a specific paper grade depends on the printer used.

The mean *total* r^2 (i.e. solid red line) of the twelve models for tone value 75 % presented in Figure 3.8 was 0.25 and thus, inbetween the mean *total* r^2 of tone value 30 % (0.20) and tone value 50 %(0.30). The maximum *total* r^2 (i.e. dashed red line) is 0.41 (i.e. paper grade **B**, **Printer 1**: fifth bars in Fig. 3.8). Hence, 0.41 of the variation in print reflectance are explained by the combined variances of topography and gloss, because the predictor basis weight is almost fully redundant in this model.

However, the contribution of the predictor basis weight was a little more exclusive for **Printer 1** and paper **A**, whereas the exclusive amount of r^2 diminished for topography in this case. When looking at paper **B** printed on **Printer 2** basis weight and gloss added little to no information to the r^2.

The model for tone value 100 % in Figure 3.9 shows a different result compared to the other tone values, although the mean *total* r^2 (i.e. solid red line) of 0.24 is within the range of the other models but the mean value for this model is not of real importance, which can be seen from Figure 3.9. On the one hand the mean r^2 for **Printer 1** is 0.39 and the other hand the r^2 for **Printer 2** is 0.09.

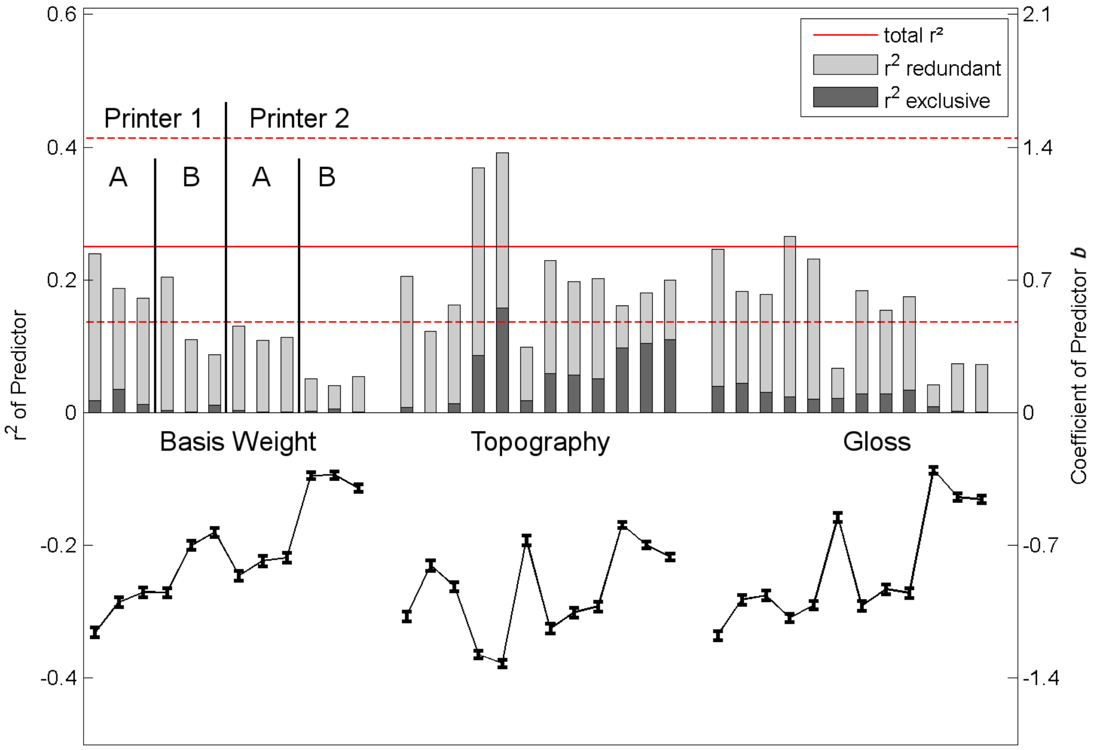

Figure 3.8 Reduced model for tone value 75 %.

The majority of print unevenness for **Printer 1** was explained by the variance in topography with a maximum of 0.59 (i.e. paper grade **B**, **Printer 1**: fifth bars in Fig. 3.9). Conversely, for **Printer 2** little contribution can be found by the measured local paper properties. r^2 is particularly low for paper grade **B** on **Printer 2**. Topography and gloss actually exhibit zero r^2 for one sample (paper grade **B**) printed on **Printer 2**. This is confirmed by b where a crossover of the zero line is observed.

Figure 3.9 clearly illustrates, that **Printer 1** and **Printer 2** differ in either the transfer-, fusing section or toner characteristics, particularly for tone value 100 %. Comparing the results of tone value 100 % to the results of the lower tone values 30 % to 75 %, the influence of the predictor topography seems to change. For **Printer 1** topography is not as important as for **Printer 2** in the lowest tone value. However, with increasing tone value, topography increasingly becomes substantial for **Printer 1**.

Chen et al. (2012) concluded, that the most important overall paper properties for print unevenness (tone value 100 %) were – in ranking order – brightness, opacity, basis weight, gloss and PPS roughness. The result was based on ten different commercial paper samples and three different printers. However, the results observed

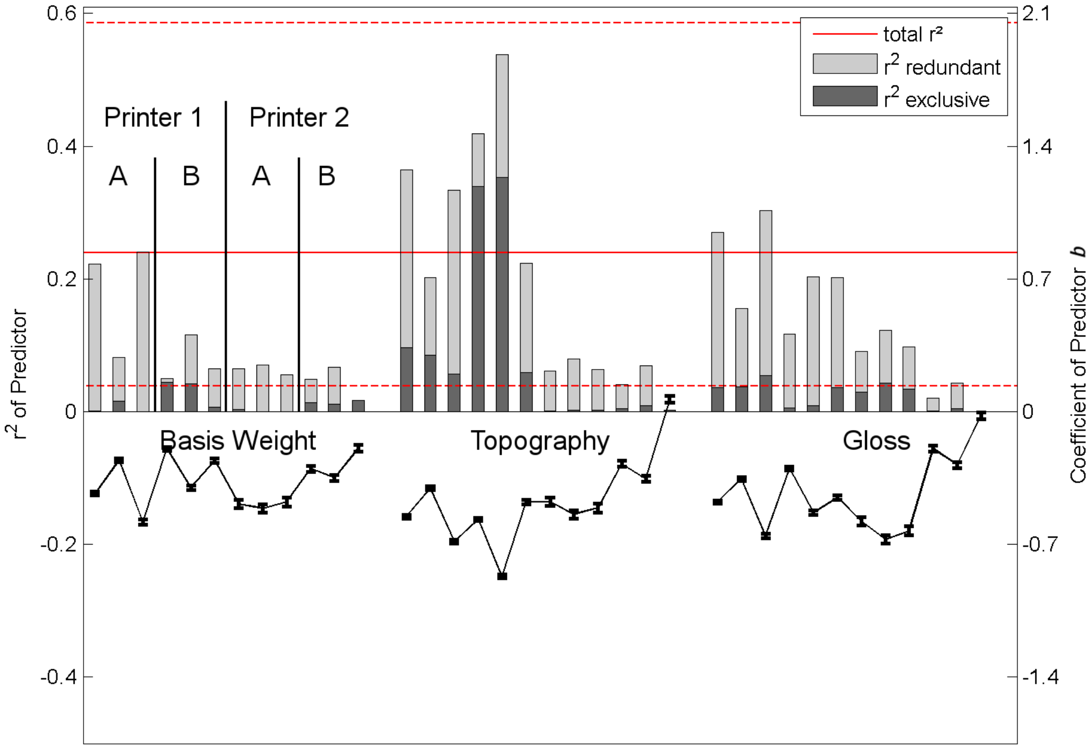

Figure 3.9 Reduced model for tone value 100 %.

within this thesis showed that local brightness and local opacity did not contribute very much to the models.

Further, Sirvio et al. (2008) found that roughness was highly important for tone value 100 %. Although roughness and topography are related, the observed results of tone value 100 % showed that local topography was the driving force.

3.5 Conclusion

Two different paper grades were evaluated on two xerographic printers and for four different tone values ranging from 30 % to 100 %. The printed images were examined in the wavelength band of interest with respect to print mottle (i.e. wavelength band of 2 mm to 8 mm). Seven local paper properties were measured, namely basis weight, topography, brightness, gloss, opacity, thickness variation and macroroughness. Multiple linear regression analysis was performed to identify the most relevant local paper property with regard to print mottle in xerographic printing.

The full models with seven predictors revealed a high redundancy of the paper properties. Therefore, a reduction of the model to three relevant predictors (i.e. basis weight, topography and gloss) was conducted without considerable loss of r^2. Basis

Table 3.3 Summary of total r^2 for all examined tone values.

tone value / total r^2	30 %	50 %	75 %	100 %
maximum	0.30	0.39	0.41	0.59
minimum	0.10	0.23	0.14	0.04
mean	0.20	0.30	0.25	0.24

weight was contributing most in the tone value 50 % and 75 %. Topography had a major impact on print unevenness. However, the extent of contribution varied with printer and tone value. Similarly was the behaviour of the predictor gloss. The mean –, maximum – and minimum total r^2 for the four different tone values is represented in Table 3.3.

The orientation of the correlation (i.e. coefficient of predictor b) was the same for all predictors and all tone values. Locally higher basis weight corresponded to elevated regions and exhibited a higher gloss. These regions were more likely to receive more toner and might therefore have a lower print reflectance and it can be concluded, that topography, gloss and basis weight had a strong effect on print mottle in xerographic printing.

Chapter 4

Print Unevenness in Inkjet Printing

4.1 Inkjet Printing

Inkjet printing is besides xerographic printing the second most common digital printing technology. The basic imaging element in inkjet printing is the ink drop. The principles of droplet generation were already discovered in the late 1800s by Plateau and theoretically described by Rayleigh (1878). These findings formed the basis of the continuous inkjet printing process which was commercialised in the 1960s. In inkjet printing various techniques can be divided into continuous jet (CS) and drop and demand jet (DOD) printing (see Fig. 4.1).

Figure 4.2 shows the droplet formation of a continuous jet. Due to perturbation of a long and thin liquid cylinder it distorts itself in order to lower its surface energy (i.e. Plateau–Raleigh–Instability). The distortion amplifies and the liquid cylinder breaks up into droplets. The droplet formation is dependent on the wavelength of distortion. When the wavelength of the distortion exceeds the perimeter of the liquid cylinder, the droplet forms spontaneously. The droplet size mainly depends on the nozzle size, the viscosity and surface free energy of the liquid and the excitation frequency (Kipphan, 2000).

Continuous inkjet printing can be further divided in binary (Fig. 4.3a) and multiple (Fig. 4.3b) deflected systems. In the binary deflection system the droplet can be either charged or not charged. In the uncharged case, the droplet can travel to the paper, whereas in the charged case, the droplet is deflected and collected in the gutter where the excess ink is recycled. In the multiple deflection system, the uncharged droplets are collected in the gutter, whereas differently charged droplets land on different positions on the paper. Both have in common that the droplets are generated by high frequency oscillations of a piezoelectric crystal. The advantage of CS is the higher printing speed compared to DOD.

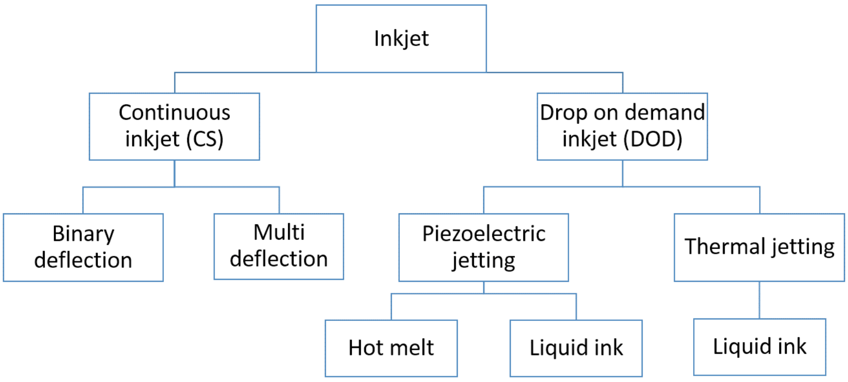

Figure 4.1 Classification of inkjet methods (adopted from Oittinen and Saarelma (1998)).

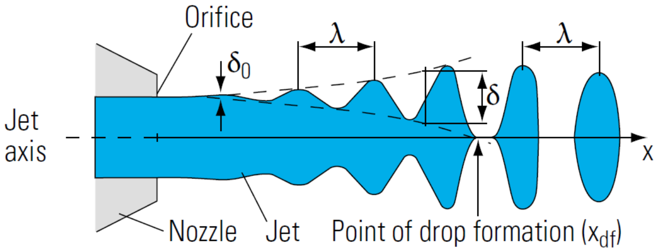

Figure 4.2 Droplet formation in a continuous jet due to constriction of the ink jet (Kipphan, 2000).

The typical droplet volume of an CS inkjet printer with a nozzle diameter of 12 µm is 4 pL with an equivalent spherical diameter of 20 µm. The speed of this droplet is about 40 m/s and the distance between two droplets is around 60 µm (Kipphan, 2000).

The two predominant DOD inkjet technologies are piezoelectric and thermal jetting. The main component of a thermal inkjet printhead (also called bubble jet) is an electric heater which is attached to the ink chamber, see Figure 4.4. The heater is controlled by an electric current pulse. First step of droplet generation is the activation of the current of the heater. Within a few microseconds the ink is superheated to 300 °C (i.e. critical temperature for bubble nucleation of water based inks) and the water vaporises. This water vapour bubble immediately expands and forces the ink out of the nozzle. After the current is turned off, the temperature decreases and the bubble collapses, the droplet breaks and travels towards the paper. Capillary forces causes refilling of the nozzle and a new heating cycle starts (Yang, 2003).

Depending on the placement of the heater, the thermal inkjet printheads are classified in roof – and side shooter. Typical droplet volume for a thermal inkjet printhead is 23 pL with an equivalent spherical diameter of 35 µm.

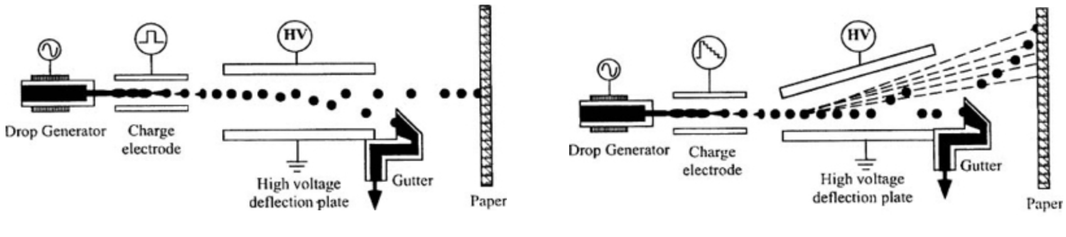

(a) **(b)**

Figure 4.3 Continuous inkjet system with **(a)** binary deflection and **(b)** multiple deflection system (Le, 1998).

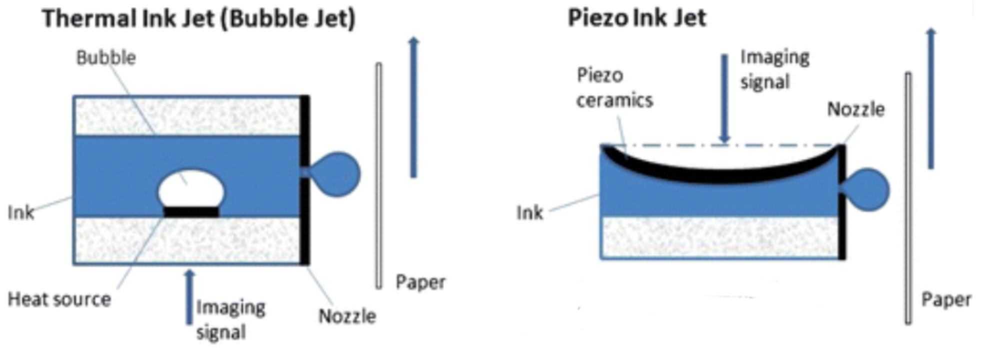

Figure 4.4 Droplet formation in DOD piezoelectric and thermal jetting (Kipphan, 2000).

In comparison to the thermal inkjet technology, the piezoelectric inkjet technology is based on mechanical deformation of the piezoelectric crystal, see Figure 4.4. In a piezoelectric crystal a mechanical deformation creates an electric field and vice versa a temporary electric field in the crystal causes a temporary deformation. Deformation of the ink channel forces the ink out of the nozzle. Depending on the printhead design, the piezoelectric printheads are operated in shear mode, bend mode, push mode or as squeeze tube (Kipphan, 2000).

Each inkjet printing technology, either thermal or piezoelectric has its particular application. The advantages and disadvantages of the technologies are enlisted in Table 4.1 (Hudd, 2010).

Besides the type of inkjet printhead technology and the used substrate, the inkjet ink plays a key role in the printing process. Ink formulations define the drop characteristics (e.g. the droplet size) and thus, they determine the reachable print quality and resolution of the print. For every inkjet printing process there are various inks available.

There are three major groups of inkjet inks: aqueous (i.e. water based), non-aqueous, and hot melt. Inkjet inks generally have a low viscosity in order to create small droplets and enable reliable jetting onto the paper. Low viscosity of the ink

Table 4.1 Advantages and disadvantages of thermal and piezoelectric inkjet printheads.

	Thermal	Piezoelectric
Pro's	more compact high nozzle density inexpensive	various inks longer life time small droplets variable droplet size
Con's	only water based ink shorter life time	more expensive

increases the spreading and the penetration of the droplets. The viscosity of inkjet inks commonly is between 1 mPa s to 30 mPa s. Secondly, the surface tension of inks is very important for droplet generation and contact behaviour on the paper and usually lies between 20 mN/m to 60 mN/m. Table 4.2 shows a detailed description of the ink types, the corresponding drying processes and the particular inkjet technology (Oittinen and Saarelma, 2009). Table 4.3 illustrates a typical composition of an aqueous ink.

Besides aqueous inks, hot melt – and UV inks are commonly used. The solid hot melt ink is liquefied by preheating it in the feed system. On the substrate, the ink solidifies through cooling and the advantage of these inks is that final print quality is rather independent of the substrate used.

UV curable inks usually contain reactive monomers or photo initiators. After printing, the ink is exposed to an UV lamp and the reactive monomers create a rigid film. UV inks are, similarly to hot melt inks, less substrate dependent. The drawbacks are rather high costs and health and safety related issues (Svanholm, 2007).

The colourant in an inkjet ink is either pigment or dye based. The dye is a colourant which is dissolved in the carrier fluid, whereas the pigment is a powder of solid colourant particles suspended in the carrier fluid. The use of dye or pigment based ink depends on the requirement on the final print. Dye based inks provide highly saturated colour, due to low scattering of light. However, they exhibit a rather low lightfastness and a higher tendency for ink penetration (Svanholm, 2007). The pigment based ink on the contrary, has a higher lightfastness and is less affected by environmental influences but provides a lower colour gamut and has a higher tendency to nozzle clogging. Pigments typically have a size of 100 nm to 300 nm.

The wetting, spreading and penetration phenomenon of the ink droplet is described in Section 2.5 Wetting Phenomenon and Ink Penetration. Wetting is typically characterized by contact angle measurements.

Table 4.2 Inkjet ink properties and application areas (Oittinen and Saarelma, 2009).

	Ink Type	Viscosity [mPa s]	Ink layer thickness [µm]	Drop volume [pL]	Drying
Thermal inkjet	Water based	1 - 5	< 0.5	6 - 30	Absorption, evaporation
Piezoelectric inkjet	Water, oil, and solvent based	5 - 20	< 0.5	4 - 30	Absorption, evaporation
	Hot melt	10 - 30	12 - 18	20 - 30	Solidification through cooling
	UV curing	15 - 30	10 - 20	10 - 30	Radiation cross linking
Continuous inkjet	Solvent, water, MEK (methyl ethyl ketone) based	1 - 5	< 0.5	5 - 100	Absorption, evaporation

Table 4.3 Water based inkjet ink composition (Le, 1998).

Component	Function	Concentration [%]
Deionised water	Aqueous carrier medium	60 - 90
Water soluble solvent	Humectant, viscosity control	5 - 30
Dye or pigment	Provides Colour	1 - 10
Surfactant	Wetting, penetration	0.1 - 10
Biocide	Prevents biological growth	0.05 - 1
Buffer	Controls pH of ink	0.1 -0.5
Other additives	Chelating agent, defoamer, ...	> 1

4.2 Print Unevenness in Inkjet Printing

The main print quality requirements for inkjet printing are prints with strong, bright colours (i.e. high print density), evenly printed (i.e. low print mottle) and good edge acuity. Edge acuity comprises low feathering, wicking and colour to colour bleeding (Brander and Thorn, 1997; Holik, 2013). An example for wicking can be seen in Figure 4.5a. In this case, the printing ink travels along fibres and thus generates a ragged edge. The target width was 1 pixel, but due to lateral spreading the real width differs from the digital target. Feathering is defined as the raggedness of the line and diminishes the sharpness of printed images. However, there is no clear distinction between wicking and feathering because both effects are caused by lateral spreading of the ink (Svanholm, 2007).

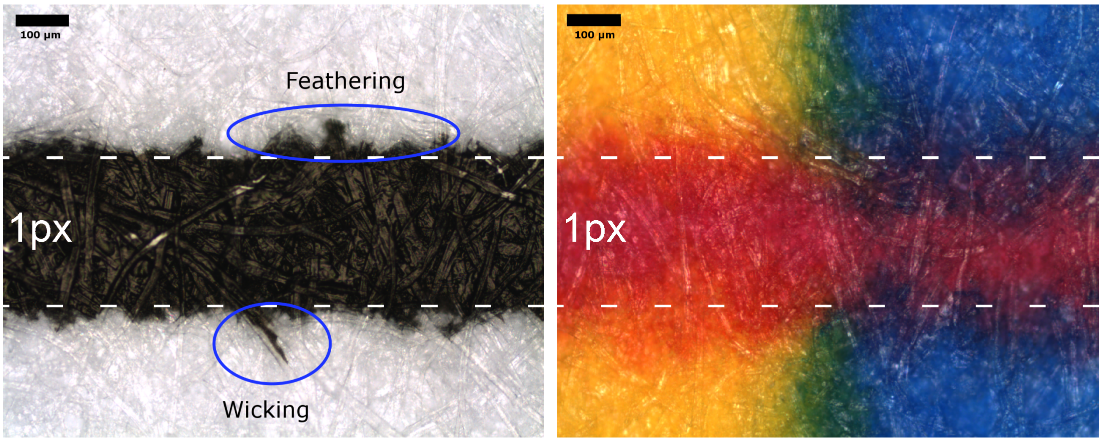

(a) **(b)**

Figure 4.5 Microscopy images (10x magnification) of **(a)** wicking of a black pigment ink and **(b)** bleeding of cyan, magenta and yellow dye on a 80 g/m^2 uncoated paper sheet (Mandlez, 2015).

Bleeding or intercolour bleed is the tendency of the wet ink to bleed into the still wet ink of another colour. Figure 4.5b shows the intercolour bleed of cyan into yellow (green regions), magenta into yellow (orange regions) and cyan into magenta (purple regions). Similarly to wicking and feathering, bleeding diminishes the sharpness and thus the quality of the printed image. A good overview of the standard print quality parameters for inkjet printing is given by Mandlez (2015).

The counteracting effect to lateral distribution of the ink is the vertical movement into the paper (i.e. ink penetration). If the penetration overwhelms, show through and for uneven penetration, variations in optical print density (i.e. print mottle) might occur. Print density is a standard measure for print quality in inkjet printing and is usually measured with a densitometer. The higher the variations in print density, the higher is the print unevenness in the printed image. In order to understand the processes causing print unevenness in inkjet printing a lot of research has been carried out.

Lamminmäki et al. (2009, 2010) investigated the role of binder type in the coating colour regarding inkjet print quality, in particular polyvinyl alcohol (PVOH) and styrene acrylate latex. The conclusion was, that liquid ink absorption (i.e. dye and water based ink) into the porous structure of inkjet paper was confirmed to be capillarity and permeability driven. It was shown that increased amount of PVOH increased the amount of bleeding. With increasing pore size distribution, PVOH was unable to block the larger pores, which determined the colourant transport. Furthermore, a quicker ink penetration speed led to print through in styrene acrylate latex bound coating structures.

Zhang et al. (2015), comparable examined the impact of varying binder composition on inkjet printing parameters such as optical solid density, dot gain and line raggedness. The binders used were a vinyl acetate copolymer (VAC) and a PVOH. It was found, that with a certain mixture (VAE:PVOH = 6:4) a larger solid density, lower dot gain, a lower line raggedness and finally the highest print density was achieved. This might be due to the difference of the pore properties in the coating colour.

Li et al. (2015) studied the penetration of ink into uncoated paper with varying sizing dosage, filler (i.e. PCC) dosage and calendering pressure. Ink penetration was estimated by means of cross sections of paper samples and Confocal Laser Scanning Microscopy. On the whole it was found that the paper surface properties and paper internal structure both had an effect on the resulting ink penetration and this led to varying print quality. For example, filler particles in the paper structure increased the porosity as well as the pore volume resulting in an increased ink penetration. The highest optical density was observed for filled, sized and calendered paper samples.

Pal et al. (2007) evaluated the influence of various levels of refining of the pulp fibres, filler addition, internal sizing and surface sizing on print quality. Changing these parameters leads to changes in the liquid ink absorption and thus to different print qualities, as suggested by Lamminmäki et al. (2009). For example, with increased amount of surface sizing, a higher ink density is achieved.

Rehberger et al. (2010) examined the impact of printing speed of a high speed inkjet printing machine on print mottle on packaging paper. The evaluation of print mottle was according to Johansson (1993) in the wavelength band of interest for print mottle (i.e. 1 mm to 8 mm). Two paper grades were examined and for one, print mottle in the halftone (i.e. 40 %) was clearly affected by the printing speed. At a higher printing speed, print mottle was found to be higher.

4.3 Paper Samples for Inkjet Printing

Within this thesis, two commercially manufactured paper grades were investigated. Both were high speed inkjet papers. The first one was a pigmented paper with a basis weight of $90\,\mathrm{g/m^2}$. The coat weight was $7\,\mathrm{g/m^2}$ each side (i.e. denoted as **P90**) and the pigment was applied within surface sizing (i.e. starch). On the other hand an uncoated surface sized (i.e. starch) paper grade with $60\,\mathrm{g/m^2}$ was selected (i.e. denoted as **U60**). Fluorescent whitening agent (FWA) was applied during the sizing/coating procedure. However both paper grades contained FWA in the base paper due to use of broke. The samples had a size of 45 mm × 45 mm and the finally examined area was 40 mm × 40 mm. Exemplary images of the used sample size and the examination area are shown in Figure 3.2 on page 64.

For printing of the samples a home office desktop inkjet printer (**DT**) and a high speed inkjet printer (**HS**) were used. The desktop printer was an Epson® *Expression*

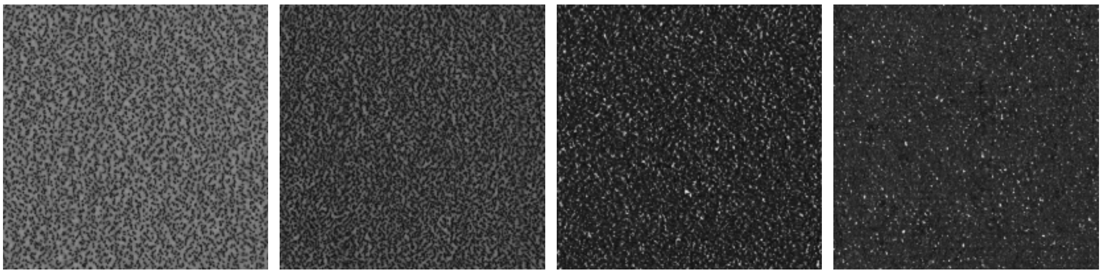

(a) 25 % **(b)** 40 % **(c)** 60 % **(d)** 90 %

Figure 4.6 Exemplary images of the tone values **(a)** 25 %, **(b)** 40 %, **(c)** 60 % and **(d)** 90 % printed with the desktop (DT) printer on the uncoated paper grade (U60), (Size: 5 mm × 5 mm).

Home XP-312. The print head is a drop on demand Epson® micro piezo electric. The variable droplet size lies between 3 pL to 14 pL. The printing speed was about 8.7 A4 pages per minute. A detailed description and evaluation of the desktop printer can be found in Mandlez (2015). The high speed inkjet printing machine used was provided by Océ (Venlo, Netherlands) and was located in Venlo, Netherlands. The print head was also a drop on demand system. Here the printing speed was much higher, at 833 mm/s, which corresponds to approximately 168 A4 sheets per minute. The ink for both inkjet printers was a high speed black pigment ink, also provided by Océ.

In pre-trials (i.e. visual ranking), the most critical black colour tone values regarding print unevenness were determined. For the DT printer, the four tone values were 25 %, 40 %, 75 % and 90 %. Figure 4.6 shows the four tone values printed with the DT printer on the U60. The tone values represent the grey scale values of the printer settings in GIMP 2.8.16 (GIMP, GNU Image Manipulation Program). Thus, the print density values measured for example with a GretagMacBeth Densitometer might not correspond to the given ones. However, it was not essential to exactly reproduce a certain tone value; they should be representative for a range of ink coverage. Hence, for the HS printer, the four tone values were 10 %, 40 %, 60 % and 90 %.

Before printing, all local paper properties listed in Table 4.4 were measured. The detailed description of the measurement methods can be found in Section 2. All local paper properties gave the same information for either the pigmented grade (P90) or the uncoated grade (U60) except the measurement with UV LED. On the one hand UV LED represents the coating coverage for P90 and on the other it is supposed to represent the sizing evenness for the uncoated grade (U60), because for U60 the FWA was applied during surface sizing.

For evaluation of the particular tone values with respect to print unevenness three samples were measured and printed. After measurement of the local paper properties, the samples printed on the DT printer were fixed to A4 paper sheets where a hole with the size of one sample was cut out with adhesive tape (i.e. Scotch Tape™). For

Table 4.4 Measured local paper properties for inkjet samples.

Paper Property	Unit	Device	Resolution [µm/pixel]
Basis Weight	[g/m^2]	β-radiography	50.00
Gloss	[%]	Imaging Reflectometer	200.00
Macroroughness	[-]	Imaging Reflectometer	200.00
UV LED	[GV image]	IFM (imaging mode)	25.60
Penetration Index	[GV image]	IFM (imaging mode)	25.60
Brightness	[GV image]	IFM (imaging mode)	25.60
Opacity	[%]	IFM (imaging mode)	25.60
Topography	[µm]	IFM	12.80

the samples printed on the HS printer holes in the carrier sheet were not necessary because the distance between print head and substrate was adjustable. Subsequently, the samples were placed in the printer and printed with the specific tone values. The exposure time for measuring the print reflection was for tone value 10 % and 25 % 100 ms, for 40 % 150 ms, for 60 % and 75 % 350 ms and for 90 % 700 ms.

The consecutive registration and image handling procedure as well as the multiple linear regression analysis were in accordance with the procedure describe in Section 2.1 Registration and Section 2.2 Multiple Linear Regression Analysis.

4.4 Results of Print Trials

The present results plots are all based on the result plots described in detail in Section 2.2 Multiple Linear Regression Analysis. For each combination of paper (P90, U60) and printer (DT, HS), 3 samples were evaluated, in total 12 samples.

Each result plot (see Fig. 4.7, 4.9, 4.10 and 4.11) represents the result of the multiple linear regression analysis with respect to the filtered printed image of the specific tone value. In case of Figure 4.7 the result of the analysis for tone value 10 % (HS) and 25 % (DT) is depicted. The first three bars of each predictor parcel show the result for tone value 25 % printed with the desktop printer (DT) on the pigmented paper grade (90 g/m^2). The second three bars of each predictor parcel show the result for tone value 10 % printed with the high speed inkjet printer (HS) on the pigmented paper grade (90 g/m^2) in Venlo. The following six samples represent the results for U60 printed on DT and HS.

The solid red line indicates the mean *total* r^2 of all 12 models which is 0.35 and the dashed red lines show the minimum and maximum *total* r^2 of the models (0.19 and 0.49 respectively). The coefficients of the predictors b, on the right axis of the result plot in Figure 4.7 (i.e. the error bars) show the sign of the correlation with a confidence interval α of 95 %. For example b for the predictor brightness represents a positive correlation between print reflectance and brightness.

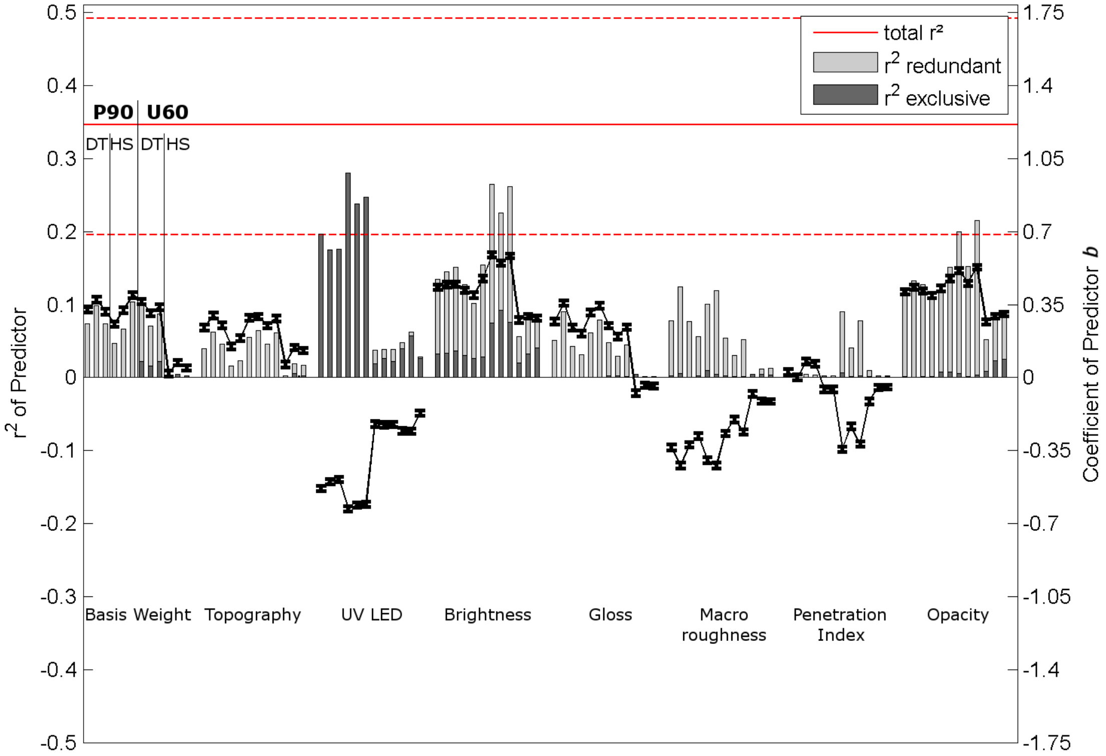

Figure 4.7 Result for tone value 10 % (HS) and 25 % (DT).

Figure 4.7 illustrates that for the lowest tone value printed on P90 the predictors UV LED (i.e. coating coverage), brightness and opacity were the most relevant ones. UV LED exhibits a r^2_{alone} between 0.20 and 0.30. Hence, most of the variation in the print reflectance was explained by the variations in the coating coverage. Furthermore, the exclusiveness of the predictor UV LED is reasonable; there is no redundancy for P90 observable. However, for P90 there was a difference between DT printed and HS printed samples, even though the same paper grade and ink was used for printing. This result indicates that also the printer used played a key role when it comes to the importance of local paper properties for print unevenness.

Although brightness contained more exclusiveness, brightness and opacity have a similar amount of r^2_{alone}. Thus, the relevance of local brightness as a predictor was higher as compared to local opacity. When looking at the other predictors in Figure 4.7 such as basis weight, topography, gloss, macroroughness and penetration index, it can be deduced that these predictors were of minor importance for the P90 grade because their r^2_{alone} hardly reaches 0.10.

The variation in print reflectance on U60 was mainly explained by the variation of local brightness and opacity (see Fig. 4.7). However, for U60 a remarkable difference between the printers HS and DT can be observed. Brightness variations correlate well

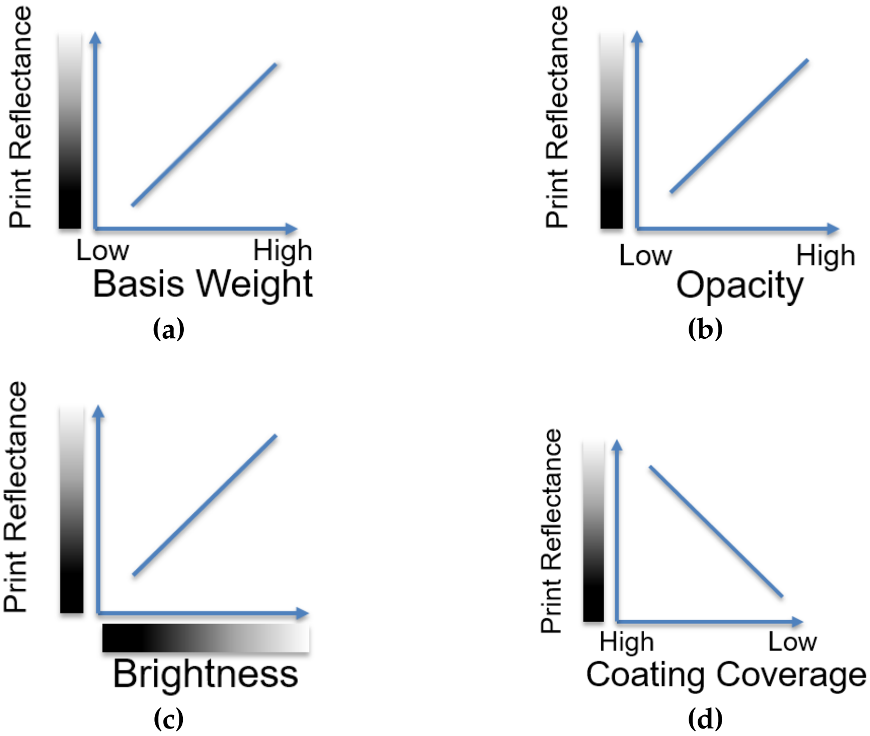

Figure 4.8 Illustration of the orientation of the coefficient of the predictor between print reflectance and the predictors basis weight (**a**), opacity (**b**), brightness (**c**) and coating coverage (**d**) as shown in Figure 4.7.

with print reflectance for DT printer, but not so much for the HS printer. UV LED which is supposed to represent the sizing evenness does not contribute much to the model, although it exhibits a moderate amount of $r^2_{exclusive}$. Comparable to the result for P90, the rest of the predictors is of minor importance for U60.

Figure 4.8 illustrates the orientation of the coefficient of the predictor (b) between print reflectance and four predictors (i.e. basis weight, opacity, brightness and coating coverage). Thus, a positive coefficient of the predictor for basis weight, as shown by the error bars in Figure 4.7 implies that the print reflectance was higher at regions exhibiting higher local basis weight. Similarly, local print reflectance increases with increasing brightness (4.8c) and opacity (Fig. 4.8b). Brighter regions on the sample before printing were also brighter after printing. Areas of higher opacity tended to have a higher print reflectance which might be related to a locally higher light scattering coefficient. This trends applied for both paper grades (P90 and U60).

Coating coverage in Figure 4.8d stands for the predictor UV LED, but only for P90, because U60 is uncoated. For the predictor coating coverage, the coefficient of the predictor was negative (Fig. 4.8d). At regions exhibiting a higher local coating coverage, the print reflectance was higher. High print reflectance in this case can not

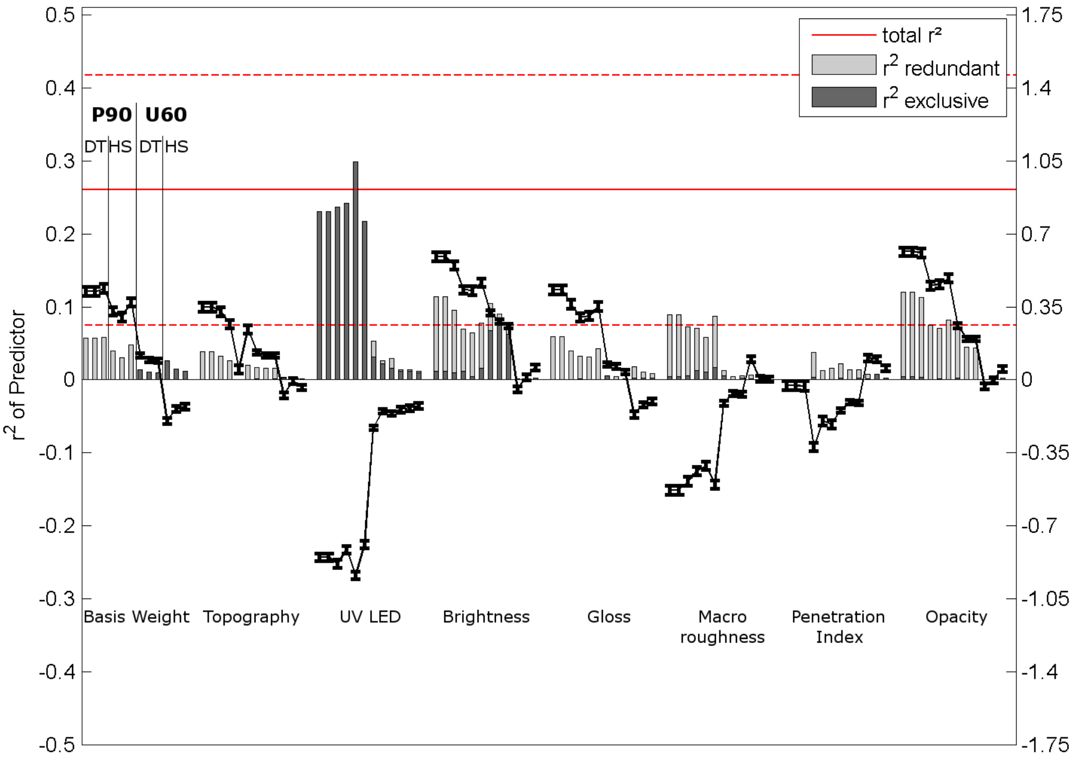

Figure 4.9 Result for tone value 40 %.

be dedicated to higher brightness or opacity, since the contribution of the predictor coating coverage was completely exclusive and thus, the information of coating coverage was not related to brightness, opacity, basis weight or any other predictor in this result plot. This might be due to less spreading of the ink droplets in regions with locally higher coat weight.

When looking at the results for tone value 40 % in Figure 4.9 the predictor UV LED for P90, which represents the coating coverage gained slightly more relevance compared to the lowest tone values whereas the importance of the other predictors such as brightness, opacity and basis weight diminishes. For U60 the contributions of all predictors were rather low. This is also apparent from the mean *total* r^2 (0.26), the maximum *total* r^2 (0.42) and the minimum *total* r^2 (0.08).

The results for tone value 60 % (HS) and 75 % (DT) presented in Figure 4.10 emphasize the trend of decreasing relevance of the measured local paper properties. Furthermore, the contribution of coating coverage, the most relevant predictor for P90 in tone value 10 %, 25 % and 40 % decreased. Except this predictor, none of the measured local paper properties exhibited a r^2_{alone} greater than 0.10. It seems that for tone value 60 % (HS) and 75 % (DT) other mechanisms, not covered by the local paper properties measured in this work determine the print unevenness.

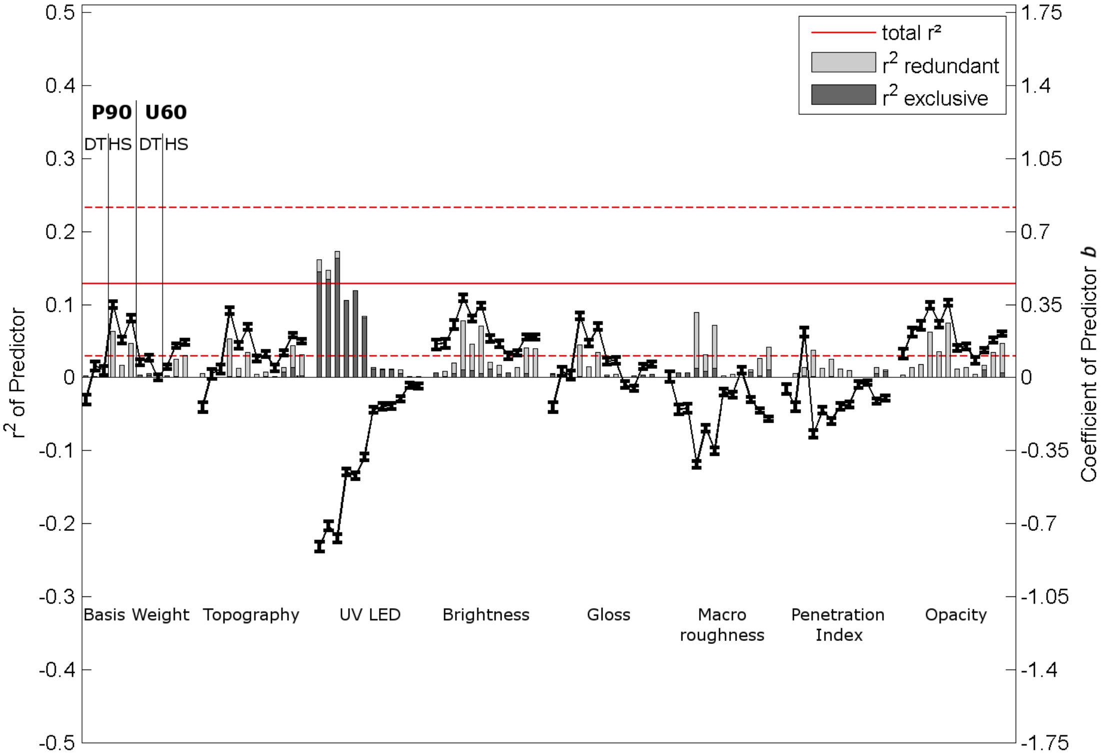

Figure 4.10 Result for tone value 60 % (HS) and 75 % (DT).

A further increase in tone value to 90 % revealed a completely different result as displayed in Figure 4.11. For the pigmented grade (P90) gloss, ink penetration and to a small extent basis weight and macroroughness became relevant. However, remarkable differences between the DT and HS printed samples were observed. Furthermore, coating coverage has vanished as a contributing predictor. This might be explained by the decreasing influence of the optical dot gain for high tone values. Optical dot gain is high especially in tone values up to 60 %.

Ink penetration becomes usually more important at higher tone values or at full coverage, because variations in ink penetration are more pronounced due to a higher ink load (i.e. measurement method). For P90 the ink penetration had a noticeable exclusive contribution and was positively correlated to print reflectance (see error bars in Fig. 4.11). Hence, in regions where the ink penetrates to a higher extent, print reflectance is higher which means these regions are brighter. The second important predictor for P90 was gloss which also showed a relevant amount of $r^2_{exclusive}$. Areas of higher gloss were correlated to lower print reflectance. A reason for this might be that glossier areas are more densified and therefore ink penetration was lower.

For U60 printed on the HS printer it is apparent from Figure 4.11 that the predictors basis weight, topography, brightness, macroroughness and opacity were relevant.

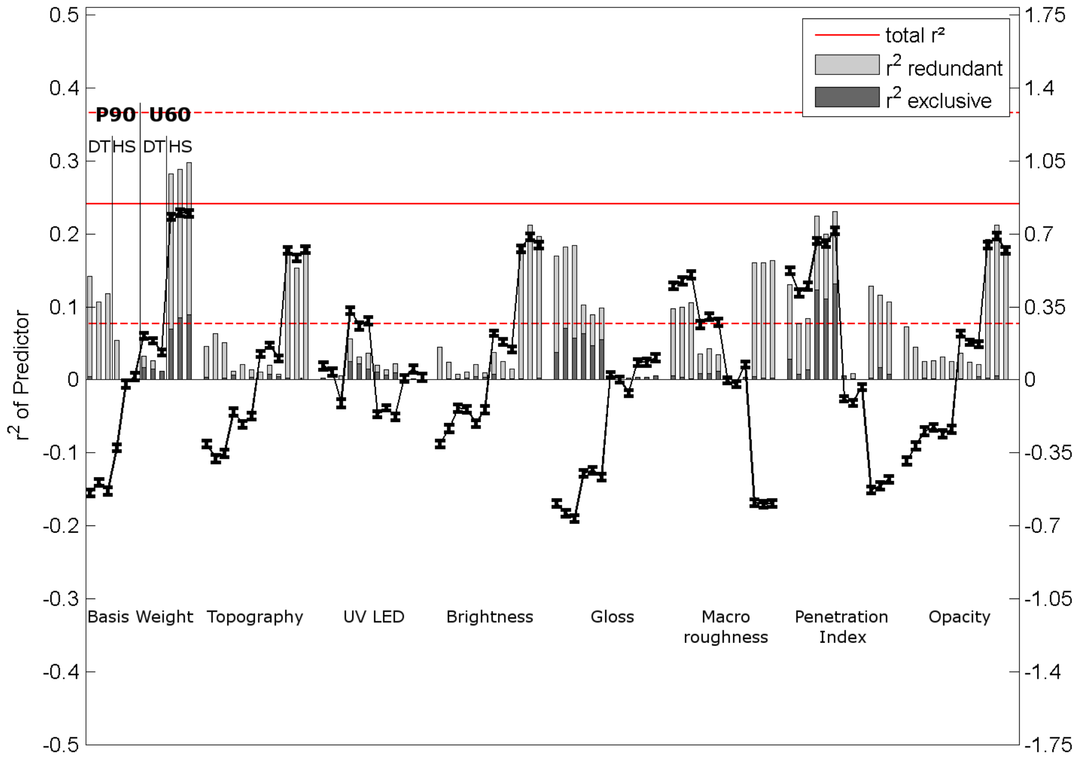

Figure 4.11 Result for tone value 90 %.

Variations in basis weight explained nearly 0.30 of the variation in print unevenness and thereof 0.10 exclusively. Although the explanatory power of basis weight for the HS printed sample was rather high, the results for U60 DT printed exhibited little contribution to the model. Similarly, the other predictors did not relevantly contributed to the model. One explanation for these results could be provided by the findings of Rehberger et al. (2010) who stated that increased printing speed causes higher print mottle. The printing speed for HS was significantly higher than DT and thus a higher print unevenness could be explained by variations in local paper properties to a higher extent.

The relevance of the measured local paper properties for all tone values and for both paper grades is finally summed up and condensed in Table 4.5 and Table 4.6. +++ stands for very important (high contribution, high $r^2_{exclusive}$), ++ stands for relevant and 0 means that the local paper property was not relevant in order to explain the variance in print unevenness.

From Table 4.5 it can be seen that for all tone values except the highest one, variations in coating coverage contributed most to the multiple linear regression model compared to the other paper properties. In the lower tone values optical properties such as brightness variations and opacity variations additionally exhibited informa-

Table 4.5 Relevance of measured local paper properties for specific tone value for the pigmented paper grade (P90).

tone value	25 %	10 %	40 %		75 %	60 %	90 %	
property	DT	HS	DT	HS	DT	HS	DT	HS
Basis Weight	+	+	0	0	0	0	+	0
Topography	0	0	0	0	0	0	0	0
Coating Coverage	++	+++	+++	+++	++	+	0	0
Brightness	++	++	++	+	0	0	0	0
Gloss	0	0	0	0	0	0	+++	++
Macroroughness	+	+	+	+	0	+	+	0
Penetration Index	0	0	0	0	0	0	++	+++
Opacity	++	++	++	+	0	0	0	0

Table 4.6 Relevance of measured local paper properties for specific tone value for the uncoated paper grade (U60).

tone value	25 %	10 %	40 %		75 %	60 %	90 %	
property	DT	HS	DT	HS	DT	HS	DT	HS
Basis Weight	+	0	0	0	0	0	0	+++
Topography	0	0	0	0	0	0	0	+
Sizing	+	+	0	0	0	0	0	0
Brightness	+++	++	++	0	0	0	0	++
Gloss	0	0	0	0	0	0	0	0
Macroroughness	0	0	0	0	0	0	0	+
Penetration Index	0	0	0	0	0	0	0	+
Opacity	++	+	+	0	0	0	0	+

tion. For the highest tone value local gloss and local ink penetration became important.

For the uncoated paper grade U60 (Tab. 4.6), local variations in optical properties played a key role in order to explain print unevenness. However, the measured paper properties could not explain the variation for tone values 75 % and 60 % sufficiently. In the highest tone value only variations in the high speed inkjet printed samples could be explained by variations in basis weight, brightness and to some extent by macroroughness, ink penetration and opacity.

4.5 Conclusion

Two different paper grades were evaluated on two different inkjet printers (i.e. desktop printer DT and high speed inkjet printer HS) and for four different tone values ranging from 10 % to 90 % all printed with the same ink. The printed images were examined in the wavelength band of interest with respect to print mottle (i.e. wavelength band of 2 mm to 8 mm). Eight local paper properties were measured, namely basis weight, topography, UV LED (i.e. coating coverage for P90 and sizing evenness for U60), brightness, gloss, macroroughness, ink penetration and opacity. Multiple linear regression analysis was performed to identify the most relevant local paper property with regard to print mottle in inkjet printing.

The models presented (Fig. 4.7, 4.9, 4.10 and 4.11) for the four different tone values showed a varying explanatory power of the measured local paper properties. The relevance of the paper properties was further illustrated by Table 4.5 and Table 4.6. Variations in local optical properties such as brightness and opacity played a key role in explaining print unevenness for both paper grades except for tone value 75 % and 60 %. Furthermore, an inhomogeneous coating coverage was able to explain local print reflectance for pigmented paper, whereas variations in basis weight were important for HS samples in tone value 90 %. At higher ink loads also local ink penetration became a relevant predictor. Finally, differences between DT and HS printed samples, which revealed the influence of the printer and printing speed, were observed.

Chapter 5

Print Unevenness in Offset Printing

5.1 Sheet Fed Offset Printing

Together with web offset (i.e. heatset or coldset) printing, sheet fed offset printing belongs to the group of offset printing techniques, which are apart from other conventional printing techniques such as flexography and rotogravure, today's most important printing techniques (Kipphan, 2000). Offset printing is an indirect lithographic process where an inked image is transferred from a printing plate to the rubber blanket and hereafter to the printing substrate (i.e. offset). It is based on the repulsion of oil and water. The image area on the printing plate is hydrophobic and oleophilic, whereas the non-image areas are hydrophilic and oleophobic.

The principle of ink application to the substrate is illustrated in Figure 5.1, where one printing unit is depicted. First (see magnified area), the dampening unit transfers the fountain solution to the printing plate to prevent the subsequently applied ink to move to the non-image areas (i.e. ink-repellent area). The printing plate on the plate cylinder then transfers the ink and the fountain solution to the blanket cylinder (i.e. a rubber blanket). Finally, the ink and fountain solution is transmitted to the substrate (i.e. sheet or web), which is pressed against the blanket cylinder by the impression cylinder.

A standard sheet fed offset printing machine with four colours and a reversing unit is shown in Figure 5.2. The single printing units are all based on the principle described above. The colour sequence of the depicted printing machine is, beginning from the right side, black followed by a reversing unit and then black, cyan, magenta and yellow. At a typical printing speed of 15000 sheets per hour one sheet has a speed of 2.75 m/s.

The complexity of the offset printing process is rather high and depends on a variety of physical and chemical parameters such as

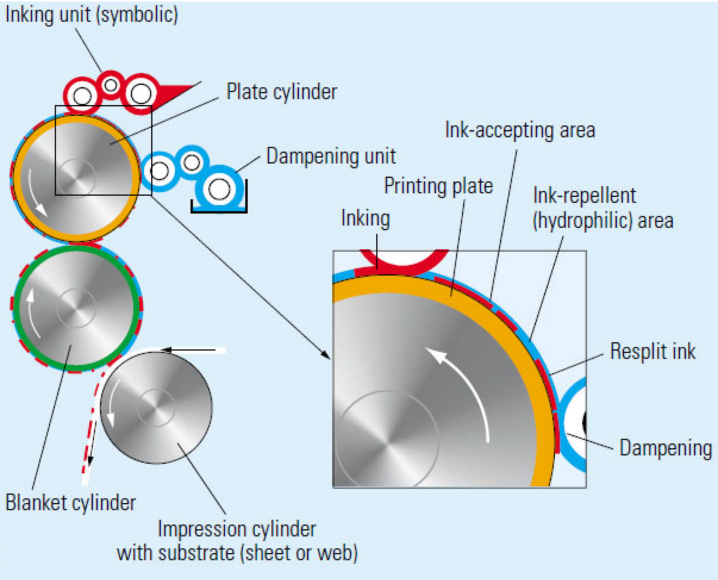

Figure 5.1 Schematic illustration of one offset printing unit (Kipphan, 2000).

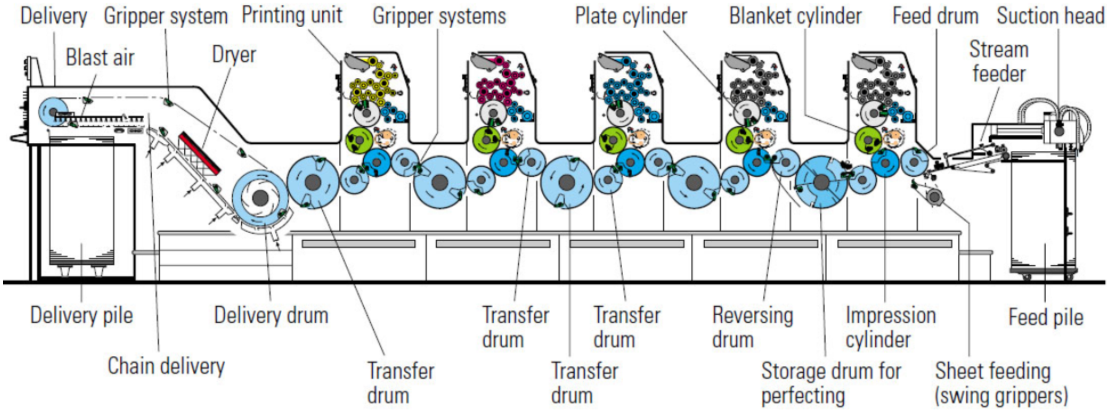

Figure 5.2 Schematic illustration of a typical offset printing machine with four colours and a reversing unit. (Kipphan, 2000).

- printing plates (e.g. surface tension, manufacturing process of plates)
- inking unit (e.g. materials used, roughness of cylinders, viscoelasticity)
- printing ink (e.g. surface tension, rheology, temperature)
- fountain solution (e.g. pH, surface tension)
- substrate (e.g. paper)
- printing machine (e.g. runability, temperature).

Table 5.1 Components of a typical sheet fed offset printing ink (Kipphan, 2000).

Component	Function	[%]
Pigment	Colour	10-30
Hard resin	Binder for pigments	20-50
Alkyd resin	Binder for pigments, carrier	< 20
Mineral oil	Carrier	< 30
Vegetable oil	Carrier, binder	< 20
Additives	Drying catalyst, – inhibitor	< 10

Thus, there are many components which have to be taken into account in order to successfully run an offset printing machine (Kipphan, 2000). A short description of the specific components follows hereafter.

The printing plates are usually 0.3 mm thick and made of aluminium or polyester. The plates are either positive or negative working, which describes the two types of photochemical reactions when developing the printing plates. In negative plate making, the light sensitive layer area is hardened by illumination and in positive plate making, the light sensitive areas are decomposed during illumination.

The inks used for sheet fed offset printing are rather viscous and consist of pigments, binders, carriers and some additives. An example for the composition of a sheet fed offset ink is illustrated in Table 5.1. Pigments, which have a size between 0.01 µm to 0.5 µm, provide the colour to the ink. These pigments and the binder need to be carried by either a mineral oil and/or a vegetable oil (e.g. linseed –, soya bean –, coconut oil). The ink, as one of the most important components need to have certain rheological properties like dynamic viscosity, thixotropy or shear thinning behaviour). Besides this, the ink tack, which generally describes the force needed to split the ink film is also an important property (Aspler, 2006).

The fountain solution plays a key role in offset printing since its main purpose is to prevent ink from adhering to the non-image areas, to keep the non-image areas clean and to reduce the temperature. The fountain solution must have a proper compatibility with the ink. Thus, the surface tension, especially the dynamic surface tension, of the fountain solution is of high importance. The fountain solution typically consists of water, pH controlling chemicals, wetting agents (e.g. isopropyl alcohol), cleaning agents, corrosion protection, fungicides and defoaming agents. The dynamic surface tension is mainly controlled by means of the isopropyl alcohol.

The transfer of the ink from the rubber blanket to the substrate (i.e. paper) in one printing unit takes place in the print nip, where the impression cylinder presses the paper to the blanket cylinder. The transfer comprises of three phases: contact between the ink and the paper, penetration of ink into paper and splitting of the ink into two layers (i.e. one on the rubber blanket and one remaining on the paper). The amount of

Table 5.2 Ink drying mechanisms (Kipphan, 2000).

	Absorption	Evaporation	Polymerisation
Sheet fed offset	✓	–	✓
Heatset web offset	(✓)	✓	(–)
Coldset web offset	✓	–	–

ink transferred in the print nip depends therefore on the relative contact area, surface roughness of the blanket and penetration rate into the paper. One commonly (e.g. (Kajanto, 1989b)) applied equation to calculate the ink transfer, which takes into take the mentioned factors is the Walker-Fetsko ink transfer equation (refer Eq. 5.1)(Walker and Fetsko, 1955).

$$Y = A\big(bB + f(X - bB)\big) \tag{5.1}$$

$$A = 1 - \exp(-kx) \tag{5.2}$$

$$B = 1 - \exp(-\frac{x}{b}) \tag{5.3}$$

where Y is the amount of ink transferred, X the initial amount of ink applied to the printing plate, f the film split fraction, which depends on the paper surface characteristics such as the capacity b to immobilise a fraction of the ink in contact with the paper. The surface smoothness of the paper is taken into account by the parameter k. A describes the coverage function and B expresses the immobilisation function. However, this approach has been criticised (e.g. Aspler (2006)) and has also been modified (e.g. Zang (1993)).

In sheet fed offset printing the transferred amount of ink usually dries within two steps: First the ink is physically dried (i.e. absorption, penetration into the paper) and subsequently it dries through oxidation and polymerisation of the drying oils and used resins. The oxidation and polymerisation lasts longer than physical drying and thus, the final drying is controlled by oxidation and polymerisation. Sometimes an additional drying unit is installed. Furthermore, the ink drying mechanisms depend on the offset process (i.e. sheet fed, heatset web, coldset web) used, see Tab. 5.2.

5.2 Print Unevenness in Sheet Fed Offset Printing

Dependending on its origin, print unevenness or print mottle in sheet fed offset printing is generally categorised into three accepted types: back-trap mottle, water interference mottle and ink-trap mottle (Sadovnikov et al., 2008). Furthermore, there are optically induced mottle effects such as halftone mottle (e.g. Yule-Nielsen effects) or gloss mottle. Apart from this, Mangin and Dubé (2006) mentioned that the term print mottle comprises fine –, coarse –, wet trap –, colour –, print through – and black mottle and thus, print mottle can have manifold manifestations. Since this thesis focused on coated paper grades in sheet fed offset printing, the subsequent discussion about print unevenness will concentrate on the interrelation between print mottle and coated paper.

Back-trap mottle for example can only occur on multicolour offset printing machines because it is generated by the subsequent printing unit. For a given colour sequence, e.g. CMYK, Cyan is trapped three times, in the subsequent magenta –, yellow – and black printing unit. If for any reason cyan is back-trapped unevenly in one or more of the following printing units, the final cyan print appears uneven.

Water interference mottle also occurs only in multicolour offset printing. When the fountain solution of the Cyan printing unit (i.e. printing sequence CMYK) is not evenly applied or it is not evenly absorbed by the substrate then the ink transfer from the subsequent printing units is negatively affected.

Ink-trap mottle is caused by an inconsistent or incorrect trapping of the ink because of incorrect ink tack grading, wrong ink sequence or variations in paper absorbency.

In order to examine the paper related reasons for the different types of print mottle, especially back-trap – and water interference mottle, a lot of research has been carried out. Engström et al. (1989) for example studied the influence of the various factors in the blade coating process with respect to the coating mass distribution and its effect on print mottle. Print mottle was expressed as the variance in print density in the wavelength band of 2 mm to 4 mm. The correlation between print mottle and variations of coating mass distribution was rather high and thus, the conclusion was that narrow mass distribution of the coating layer generates a more even print. Later, Engström and Rigdahl (1991) examined light weight coated paper and two types of woodfree paper samples. For all examined samples a positive correlation between SB latex variations and print mottle was found, which means that higher variation in SB latex content led to higher print mottle. However, they also mentioned, that variations in SB latex content on the surface of the samples were not solely accountable for print mottle. Afterwards, Engström and Rigdahl (1992) presented a litererature review about binder migration and its effect on printability and print quality. Furthermore, Engström (1994) published a profound overview regarding print mottle and coated paper, especially the formation and consolidation of the coating layer. He summarised the review, that the evenness of the coating layer is governed by the process of coating layer formation and consolidation and thus, the interaction between the liquid phase of the coating colour and the base paper during the formation and consolidation. This hypothesis is closely connected to the research work related to coating layer characterisation which has been discussed in Section 2.9.

Chinga and Helle (2003); Preston et al. (2008); Ström et al. (2010) investigated the hypothesis that the non-uniformity of the surface porosity of coated paper might cause print mottle. Chinga and Helle (2003) tested commercially manufactured light weight coated paper and Preston et al. (2008) used pilot coated (coat weight: $14\,\mathrm{g/m^2}$ per side) samples. Comparable, Ström et al. (2010) examined pilot coated sample (coat weight: $12\,\mathrm{g/m^2}$ and $8\,\mathrm{g/m^2}$ per side). Preston et al. (2008) and Ström et al. (2010) measured the surface porosity by means of imaging reflectometry (see Section 2.8: Polarised Light Reflectometry). The overall conclusion was, that in the region of interest for print mottle (i.e. wavelength band of 1 mm to 8 mm), variations in surface porosity cause print mottle and that these variations need to be minimised.

Similarly, Vyörykkä et al. (2004), who used confocal Raman technique and Ozaki et al. (2008), who used confocal laser scanning microscopy for coated paper grades with tendency for back-trap mottle, confirmed that variations in physical properties of the coating layer are more likely to generate back-trap mottle, rather than chemical variations.

Porostiy variations in the coating layer, besides variations in binder concentration, which was also examined by Groves et al. (2001), may have other causes as well. Firstly, non-uniform shrinkage of the coating layer during consolidation of the coating layer (Ragnarsson et al., 2013) and secondly, non-uniform compression during calendering (Chinga and Helle, 2003). Wikström et al. (1997) examined the calendering effects of a conventional – and an extended soft nip calender woodfree coated paper and concluded, that print mottle on extended soft nip calendered samples decreased compared to uncalendered samples. However, print mottle for conventional soft nip calendered samples was higher compared to uncalendered and extended soft nip calendered. Differences in coating layer uniformity and variations in surface porosity are also effected by variations in base paper topography, e.g. Zou et al. (2001).

Tomimasu et al. (1990) demonstrated, that the basis weight distribution controls the base paper surface roughness and furthermore the coat weight distribution, surface topography and finally porosity. The effect of surface topography and – roughness on print mottle was examined by Kasajova and Gigac (2013) by means of PPS roughness and photoclinometric measurements. Six commercial wood free coated samples were evaluated with respect to back-trap mottle. Both, surface roughness and topography could explain the print mottle to a certain amount. The same samples were analysed with regard to ink setting time, surface pore content and surface latex content (Gigac et al., 2013). Likewise, a correlation between ink setting and surface pore content and latex content was found.

Accordingly, porosity variations result in variations in the ink setting during printing and thus, variations in viscosity and furthermore in ink tack are caused. When the fluid phase of the ink penetrates into the porous structure differently (e.g. due to porosity variations) the tack locally changes. Higher tack, for example leads to higher resistance against film splitting within the ink layer and thus, areas of higher print density. In order to measure the ink tack development, most often the so called ink surface interaction tester (i.e. ISIT) is utilised (Alm et al., 2015; Ridgway and Gane,

Table 5.3 Description of sheet fed offset samples.

	Basis Weight [g/m^2]	Coat Weight [g/m^2]	Denotation
Positive ref. sample	118	27 each side	PS
Negative ref. sample	170	37 each side	NS
Matte sample	100	22 each side	MS

2004; Ström et al., 2010; Ström and Preston, 2013). Xiang et al. (1999) used another device (i.e. Micro-Tackmeter) and examined the tack development over time for various paper grades with low to high tendency to back-trap mottle in the cyan colour field. They found out, that local variations in the tack are very likely to cause back-trap mottle.

Recently Engström (2016) freshly reviewed the causes of back-trap mottle in offset printing. Emphasis was put in the areas of 1) coating layer formation, 2) binder migration, 3) binder distribution, 4) drying profiles, and 5) shrinkage and the porosity distribution. The conclusion was, that these properties influence back-trap mottle to the highest extent.

5.3 Paper Samples for Sheet Fed Offset Printing

Three different commercial woodfree coated paper samples were investigated with respect to print mottle in sheet fed offset printing. The sample names, basis weight and the coat weights are shown in Table 5.3. Positive reference (denoted as **PS**) means, that this paper sample exhibits good print quality regarding print mottle and vice versa for the negative reference samples (denoted **NS**). The difference between the two glossy grades **NS**, **PS** and the matte sample (i.e. denoted as **MS**), is that **MS** was less calendered and accordingly showed a rougher surface.

Table 5.4 shows the local paper properties measured on the samples before printing. The sample size was 40 mm × 40 mm and the finally examined area was 38 mm × 38 mm. The sample size for those samples examined with the PST and the ATR IR (i.e. bottom in Tab. 5.4) was 10 mm × 9 mm, because of limited size of the measurement devices (see Section 2.6 and 2.10 in Measurement of Local Paper Properties). Thus, these two measurements are not included in the full result plots like the rest of the local paper properties, but they are discussed separately.

Figure 5.3 shows exemplary raw data and filtered images (see Section 2.1) of basis weight, topography and coating coverage of one matte paper sample. For the basis weight images, bright areas are indicating regions of higher basis weight. Comparable, bright regions in the topography images are elevated and for the coating coverage image, brighter regions correspond to higher local coat weight. After measuring the local paper properties, all paper samples were printed on a 6 colour Heidelberg SM

Table 5.4 Measured local paper properties for sheet fed offset samples samples.

Paper Property	Unit	Device	Res. [µm/pixel]
Basis Weight	[g/m^2]	β-radiography	50.00
Refractive Index	[%]	Imaging Reflectometer	200.00
Gloss 2°	[%]	Imaging Reflectometer	200.00
Gloss 20°	[%]	Imaging Reflectometer	200.00
Macroroughness	[-]	Imaging Reflectometer	200.00
Microroughness	[-]	Imaging Reflectometer	200.00
Brightness	[GV image]	IFM (imaging mode)	25.60
Coating Coverage	[GV image]	IFM (imaging mode)	25.60
Topography	[µm]	IFM	12.80
Thickness Variation	[µm]	IFM	12.80
Topography u. Load	[GV image]	PST	17.00
ATR IR	[%]	Spectrophotometer	200.00

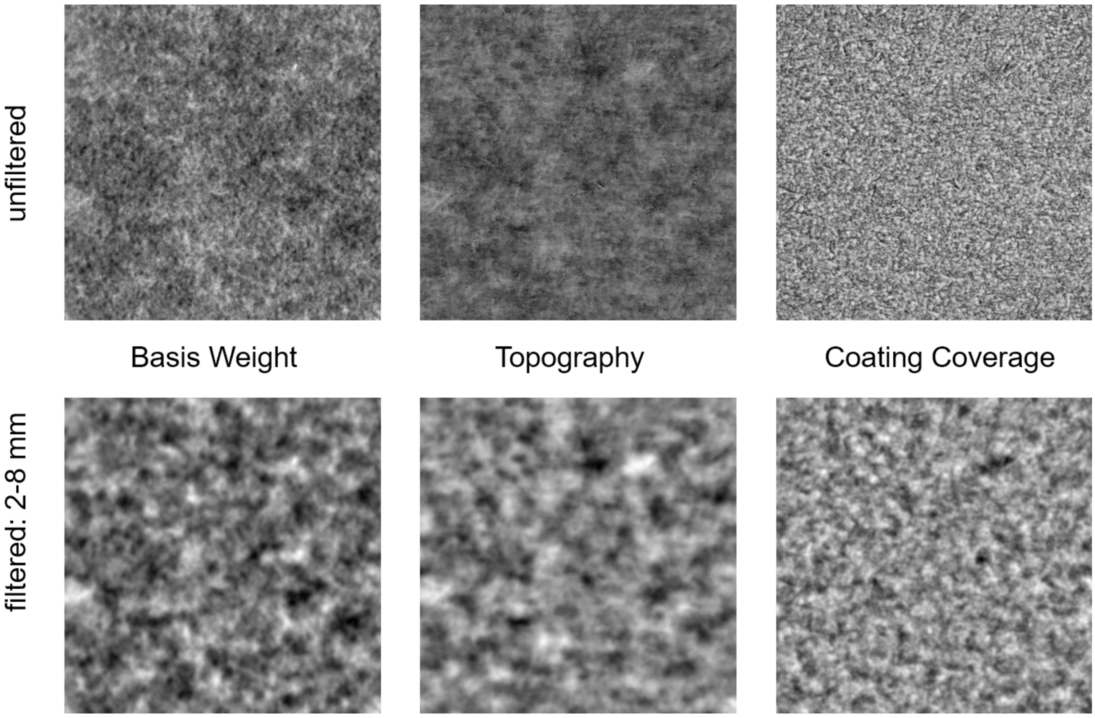

Figure 5.3 Illustration of registered raw and filtered images of one matte paper sample (size of images: 38 mm × 38 mm).

XL 8 sheet fed offset press with a printing speed of 10000 sheets per hour. The printing plates used were AGFA Amigo. The ink used for the print trial was a NOVAVIT® Supreme Bio and the rubber blanket was a Continental® SP Evolution. The colour

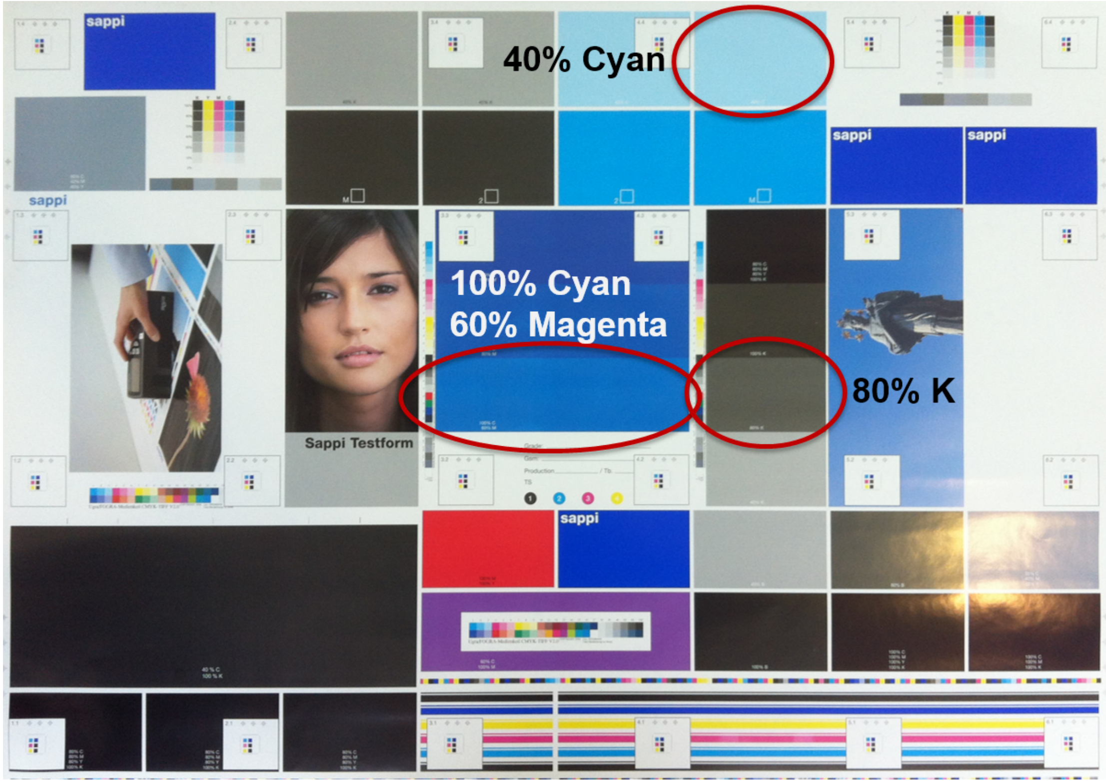

Figure 5.4 Print layout for sheet fed offset printing. The three examined colour fields are marked by the ellipses.

sequence was key black (K), cyan (C), magenta (M), yellow (Y), pantone blue (P) and last black (B).

Three colour fields were examined: The mixed field 100 % C with 60 % M, 40 % C and 80 % K. For the print trials of the ATR IR spectroscopy samples, one colour field (i.e. mixed field 100 % C with 60 % M) and for the print trials of the topography under load samples two colour fields were examined (i.e. 100 % C with 60 % M, 80 % K). The print layout is depicted in Figure 5.4 and additionally the examined colour fields are highlighted. Figure 5.5 shows magnifications of the three colour fields. The scans are parallel to the edge of one printing sheet and one can see the screen angle for C, B and M in order to avoid Moiré patterns.

The previously measured and marked samples were placed on top of the related sheets (e.g. matte sample on matte sheet) and fixed with an adhesive tape before printing. Subsequently the sheets were distributed in a stack of sheets in order to avoid influences from the previous samples such as the memory effect. After printing, the samples were allowed to dry in the stack for one hour and then the sample were conditioned in the climate room for 24 hours. Finally the print reflectance was measured with the IFM. The following descreening, filtering and modelling was according to the procedure described in Section 2.2 Multiple Linear Regression Analysis.

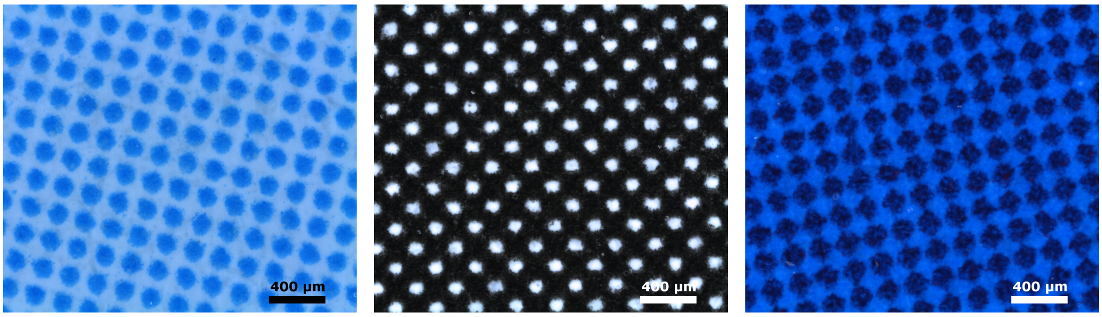

(a) 40 % cyan. **(b)** 80 % black. **(c)** 100 % cyan & 60 % magenta.

Figure 5.5 Magnification of the marked colour fields in Figure 5.4.

5.4 Results of Print Trials

The result plots presented in this chapter are all based on the result plots described and explained in Section 2.2 Multiple Linear Regression Analysis. Each result plot represents the data with respect to the particular colour field. The result plot shown in Figure 5.6 shows the combined result of the multiple linear regression analysis for the 40 % cyan colour field. Three paper grades were examined: positive reference (**PS**), negative reference (**NS**) and matte sample (**MS**). The first three bars of each predictor represent the modelling results (i.e. the r^2_{alone}) for **PS**. The second three bars represent the modelling results of the three **NS** and accordingly the last three bars belong to **MS**. The error bars correspond to the coefficients of the predictors b with a confidence interval α of 95 %. The detailed explanation of b and r^2_{alone} can be found in Section 2.2.

The solid red line in Figure 5.6 indicates the mean *total* r^2 of all 9 models (i.e. 3 samples for 3 paper grades) and the dashed red lines show the minimum and maximum *total* r^2 of the models. The mean *total* r^2 for the three grades **PS**, **NS** and **MS** was 0.41. The maximum *total* r^2 was 0.57, which was observed for the second model of the **NS** block. The lowest *total* r^2 of 0.16 was observed for the third model of the PS block.

Figure 5.6 clearly shows a difference between the three paper grades **PS**, **NS** and **MS**. The mean *total* r^2 of the positive samples **PS** was 0.20, of the matte samples **MS** 0.50, whereas for the negative samples **NS** the mean *total* r^2 was 0.53. The difference between **NS** and **PS** might stem from two reasons. On the one hand, it could be possible that none of the variation in print reflectance was explained by the measured local paper properties for **PS**. On the other hand, it is more likely that the variation

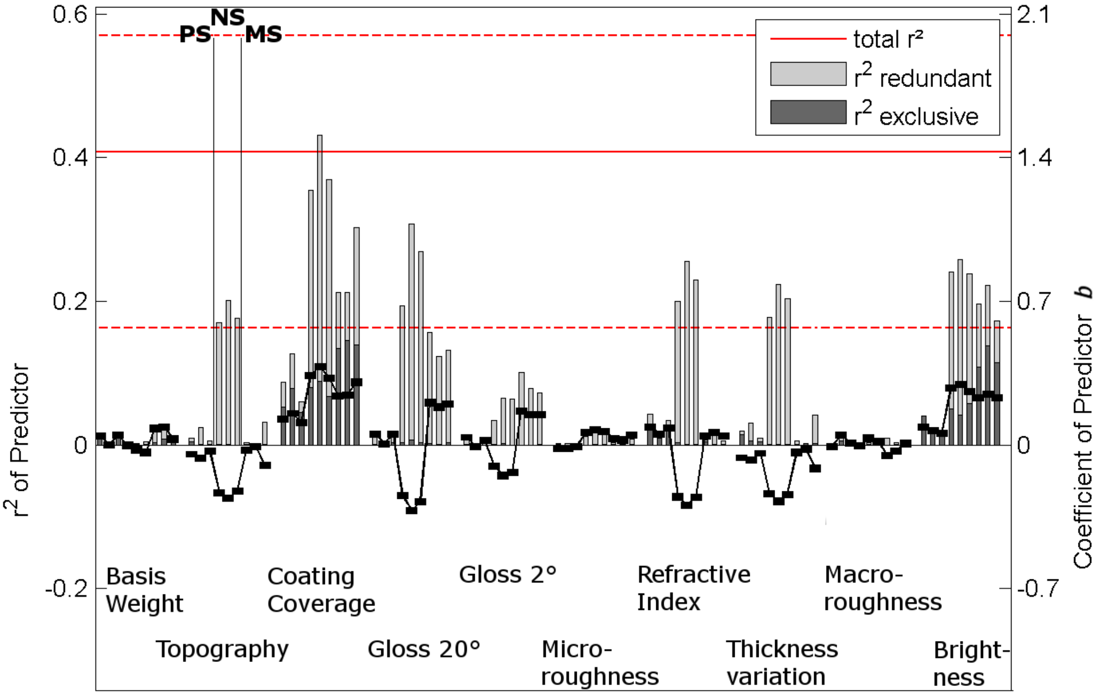

Figure 5.6 Result plot for the colour field 40 % cyan. Three paper grades were examined: positive reference (**PS**), negative reference (**NS**) and matte sample (**MS**). For each grade three samples were printed, thus 9 models (i.e. 9 bars) for each of the 10 predictors are shown in this plot.

of **PS**, which was exhibiting good print quality, was rather low. Therefore, variation in the predictors might also be low. This leads to lower signal to noise ratio which means that the random error term in the multiple linear regression analysis (see 2.2 Multiple Linear Regression Analysis) is stronger than the predictor. The error might be introduced by the printing machine. Thus, a lower variation in the target was hardly explained by a lower varying predictors.

Conversely, when looking at **NS**, which was exhibiting poor print quality, the measured paper properties were able to explain up to 0.57 of the variation in print reflectance. Thus, the hypothesis was, that a certain variation in print reflectance as well as in the local paper properties is beneficial in order to gain information about the paper related reasons for print unevenness. **MS** lies between **PS** and **NS** regarding variations in print reflectance.

In Figure 5.6 it can be seen, that for **NS** the most contributing predictors in descending order were: coating coverage, brightness, gloss 20°, refractive index, thickness variation and topography. Coating coverage and brightness also exhibit a reasonable amount of $r^2_{exclusive}$ which means that a certain amount of their contribution was not contained in any other paper property. However, gloss 20°, refractive index, thickness variation and topography were almost redundant. Thus, there is a clear interrelationship between these paper properties.

Nevertheless, this result is in accordance with the literature (e.g. Engström (2016)), where the coating layer distribution is attributed highest importance. The added value, besides the knowledge that higher variance in coating layer distribution leads to a higher variation in print reflectance, is the information about the redundancy of the predictor as well as the orientation (i.e. the coefficient of the predictor, b) of the correlation. b for the predictor coating coverage in Figure 5.6 shows that areas of higher coat weight exhibited a higher print reflectance. Similarly, higher print reflectance corresponded to higher brightness. Gloss, the refractive index and thickness as well as thickness variation showed a negative correlation with print reflectance.

The orientation of b corresponds well to the redundancy of the predictors. Elevated regions usually exhibit lower coat weight (i.e. in blade coating) and these elevated regions are therefore calendered to a higher extend, which means that surface porosity (i.e. represented by the effective refractive index) is lower and gloss is higher.

The differences between the two types of gloss for **NS** might result from the glossy surface of this paper grade. The incident angle of the light was 75° and due to a more specular reflection more variation might be detected in the 20° acceptance angle measurement rather than in the 2° acceptance angle. Thus, the variation and explanatory power of gloss 2° was lower.

For the matte paper grade **MS** in Figure 5.6 it was observed that coating coverage, brightness and gloss 20° could explain a certain amount of variation in print reflectance, whereby only coating coverage and gloss exhibited $r^2_{exclusive}$. **MS** was less calendered than **NS**, thus, variances in coating coverage were less pronounced and variances in surface porosity might be lower, therefore, not contributing. However, when looking at the b of gloss 20°, the correlation was positive. Since b was consistent for all three **MS**, a measurement mistake can be excluded. This means, that for **MS** areas of higher gloss, exhibited a higher print reflectance even though for **NS** it was the opposite. The reason for this has not been found yet.

Generally, the absolute level of gloss of a matte paper grade, such as **MS**, measured with a gloss meter, is lower as compared to a glossy grade, such as **NS** or **PS**. However, from the results shown in Figure 5.6, it can be derived, that the variation in the paper property is decisive for the variation in print unevenness, rather than the absolute level, because variation in print reflectance in **MS** is explained by the local paper properties to a lower extent.

The result of the second examined colour field (80 % black) are depicted in Figure 5.7. For this result plot the same partition was applied as for the colour field 40 % cyan. The first three bars are the three models for **PS**, the second ones for **NS** and the last three for **MS**. The mean *total* r^2 was 0.37, the minimum *total* r^2 was 0.27, and the maximum *total* r^2 was 0.57. The three models for **PS** show similar results as for the

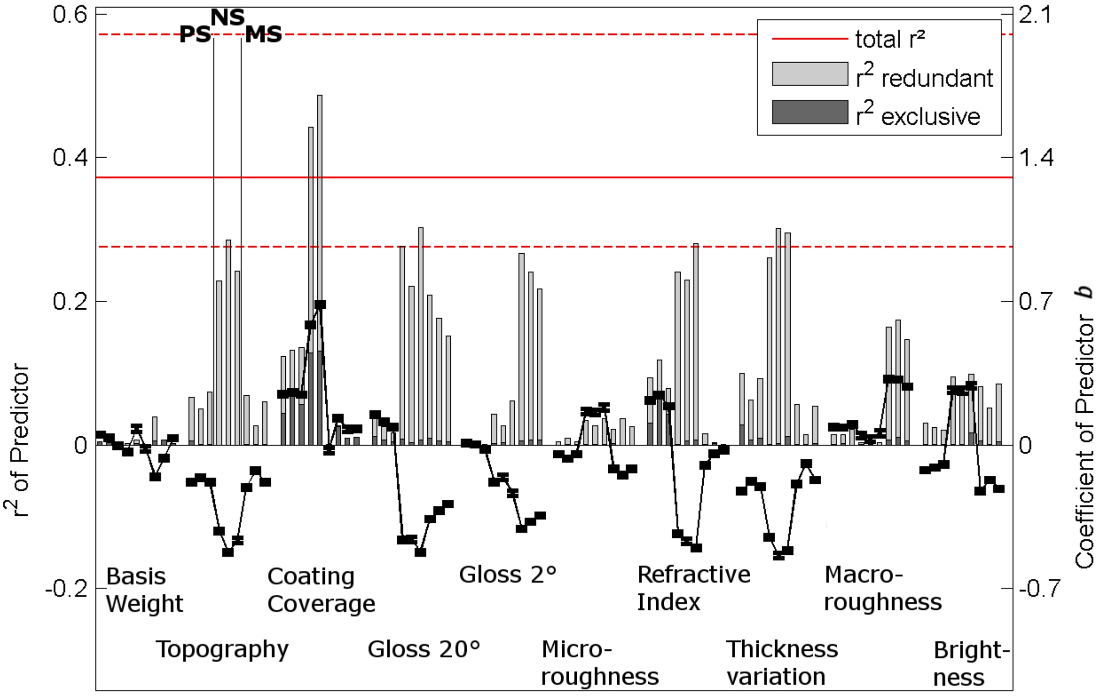

Figure 5.7 Result plot for the colour field 80 % black.

colour field 40 % cyan. The signal to noise ratio was rather low which leads to a low explanation of the variations in print reflectance by the local paper properties.

In case of **PS**, Figure 5.7 shows that at coating coverage, the refractive index as a measure for surface porosity and thickness variation contributed to the model. Coating coverage and refractive index additionally exhibited some amount of exclusive information. This means that some of the information was not contained in any of the other measured paper properties. However, the coefficient of the predictor refractive index was positively correlated to print reflectance, whereas for **NS** it was negatively correlated. For **NS**, areas of higher print reflectance exhibited a higher porosity and vice versa for **PS**. One explanation could be that there exists a critical pore size distribution, where the correlation changes, which might origin from differences in the coating colour of the two different paper grades (e.g. different used pigments such as kaolin or PCC).

When looking at the results for 80 % black **NS**, the predictor with the highest contribution was, similarly to the results for the colour field 40 % cyan, coating coverage. The third bar of the **NS** predictor coating coverage was zero because the of an defective measurement. However, the other predictors for the **NS** model such as gloss 20°, refractive index, thickness variation contributed similarly like at the 40 % cyan colour field. Brightness did not add much value to the model. This might be due to a diminished influence of the optical dot gain. Except for coating coverage, all paper properties exhibited strong redundancy. The redundancy of topography and thickness variation for example is obvious, because thickness variation comprises of topography measured on the top – and bottom side of the sample. Even though the addition of the latter has a slightly higher r^2 compared to topography alone.

The results for the matte paper grade **MS** depicted in Figure 5.7 were a slightly different to the ones for the 40 % cyan colour field. For example r^2 for the predictor coating coverage was negligible, whereas r^2 for gloss 20° had a similar level. However, the predictors gloss 2° and macroroughness gained importance.

b for gloss 2° and macroroughness were consistent. With increasing gloss 2°, the print reflectance decreased. Accordingly, increasing macroroughness resulted in increasing print reflectance. Macroroughness is connected to roughness of the base paper (see 2.8 Polarised Light Microscopy) and since **MS** was less calendered, base paper roughness might influence the final print reflectance to a higher extent. The influence of calendering would be seen in the predictor refractive index for **NS**, because of surface porosity variations.

However, *b* for gloss and brightness for **MS** changed the orientation when comparing the results for the 40 % cyan and 80 % black colour field. It might result from the printing sequence because cyan was printed in the second unit after black, the fist unit and unprinted areas in the first unit were dampened with fountain solution, which could have affected the paper properties. However, further research is necessary to clarify this.

The last colour field examined was the 100 % cyan and 60 % magenta field. There were two main differences between this colour field and the 40 % cyan and the 80 % black field. Firstly, this colour field was printed with two colours (i.e. cyan and magenta) and secondly it was printed with a mixture of full and halftone, whereas the other colour fields where printed in halftone.

The results for this colour field is depicted in Figure 5.8. For this plot the same partition applies as for the two other colour fields. The first three bars are the three models for **PS**, the second ones for **NS** and the last three for **MS**. The mean *total* r^2 was 0.46, the minimum *total* r^2 was 0.33, and the maximum *total* r^2 was 0.55.

Compared to the other two colour fields, variations in print reflectance for the paper grade **PS** could be explained up to 0.38. This might be due to a higher signal to noise ratio particularly for this colour field. The predictors coating coverage, with a high amount of exclusive information, refractive index and brightness were important for this paper grade and colour field.

For **NS** it can be seen that variations in coating coverage explained more than 0.50 of the variation in print reflectance. Additionally, r^2_{alone} for **NS** was nearly the same as the total r^2, which means the information was mostly provided by the predictor. Gloss 20°, refractive index and thickness variation as well as topography showed relevant correlations. However, these predictors were nearly fully redundant.

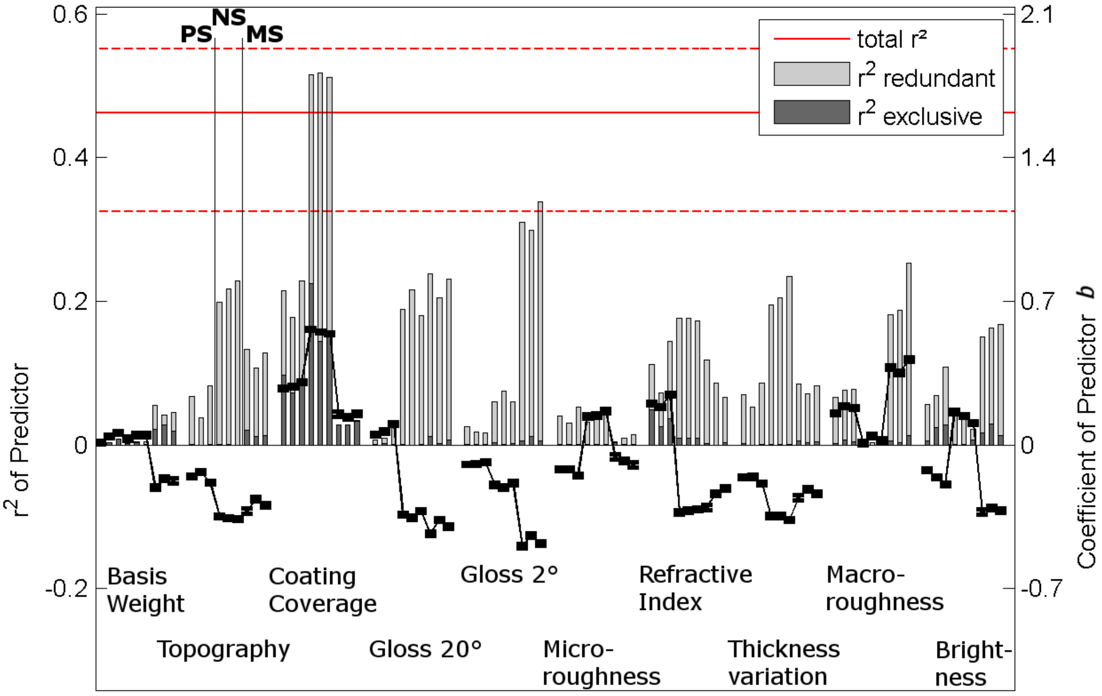

Figure 5.8 Result plot for the colour field 100 % cyan and 60 % magenta.

Compared to the other two colour fields, here, brightness diminished as a valuable predictor. This might be due to the full coverage (i.e. 100 % cyan) of the surface. Therefore, it is likely that variations in brightness did not affect print reflectance.

The results for **MS** differed a little from the results of the other two colour fields. From Figure 5.8 it is apparent that the important predictors were gloss 20° and 2° as well as topography, macroroughness and brightness. r^2_{alone} for coating coverage was completely exclusive, however, the contribution was rather low, similarly to the r^2_{alone} of basis weight.

Gloss 20° and 2° exhibited a similar r^2_{alone}. This might be dedicated to the diffuse reflection (i.e. non specular) from the surface of the matte paper samples. The b for the two gloss measurements was consistent, the higher the gloss, the lower the print reflectance. Similarly for topography, the refractive index and brightness. Elevated –, higher porous – and brighter areas resulted in lower print reflectance (i.e. areas which appeared darker on the printed colour field). Comparing these results to the results in Figures 5.6 (i.e. 40 % cyan) and 5.7 (i.e. 80 % black) it can be seen, that the orientation of the coefficients of the predictor was equivalent to the b of the colour field 80 % black, but contrary to the b of 40 % cyan.

In addition, the printing sequence may also affect the results obtained from the three colour fields. The black colour field (i.e. first printed) for example is trapped back five times, whereas the cyan and the mixed colour field are trapped back four and three times respectively. The surface properties of the paper may also vary from printing unit to printing unit, because non printing areas in the first printing unit are dampened by the fountain solution.

Combining all observations from this print trial, the following line of argument can be set up: At lower tone values, local brightness which is mainly determined by local light scattering, might contribute due to a higher optical dot gain and thus, the samples brightness was more important. At higher tone values print reflectance could reflect the amount of ink on the sample and hence, higher print reflectance might reflect lower amount of ink because the influence of optical dot gain diminishes. However, local brightness is assumed to be strongly influenced by local light scattering, which means that print reflectance and ink amount must not be directly related.

Regarding glossy paper (i.e. **NS**), higher print reflectance was closely related to locally higher coat weight, lower gloss (which corresponds to higher macroroughness), higher surface porosity, lower thickness and brightness. It can be speculated, that elevated regions exhibiting higher coat weight are more calendered, which leads to lower surface porosity and thus lower print reflectance. Lower surface porosity could be related to smaller pores and Ridgway and Gane (2004) showed that faster ink setting was found for smaller pores. However, at a certain point (e.g. the case of **PS**), lower surface porosity leads to slower ink setting (Resch et al., 2010) and therefore, higher print reflectance might be explained by a lower amount of ink on the surface of paper sample.

Regarding matte paper, the densification due to calendering is less pronounced. Thus, the influence of thickness variation and surface porosity variations is rather low. Alternatively, local gloss variations are the leading factor.

5.4.1 ATR IR Spectroscopy in Sheet Fed Offset Printing

The chemical surface analysis was performed by ATR IR Spectroscopy according to the description in Section 2.10 ATR IR Spectroscopy. The size of the scanned area was 9.60 mm × 7.80 mm. The scanning resolution was 200 µm resulting in a pixel size of 200 µm. The final modelling size was 7 mm × 7 mm.

For this sample size, the spectral filtering in the region of interest for print mottle was not possible because structures located in the wavelength band of 2 mm to 8 mm would not be recognised. Descreening via FFT filtering (i.e. removal of half tone pattern caused by printing) was also not applicable due to the small sample size. Thus, a Gaussian blur with a standard deviation of 600 µm was applied. Examples of the blurred images are depicted in Figure 5.9. Figure 5.9a shows the Gaussian blurred 100 % cyan and 60 % magenta printed image of a **PS**. Figures 5.9b–5.9d show the intensity ratios of latex (CH band), kaolin (OH band) and kaolin (SiO band) to calcium carbonate (CO_3^{2-} band) of the same paper region. The intensity ratio

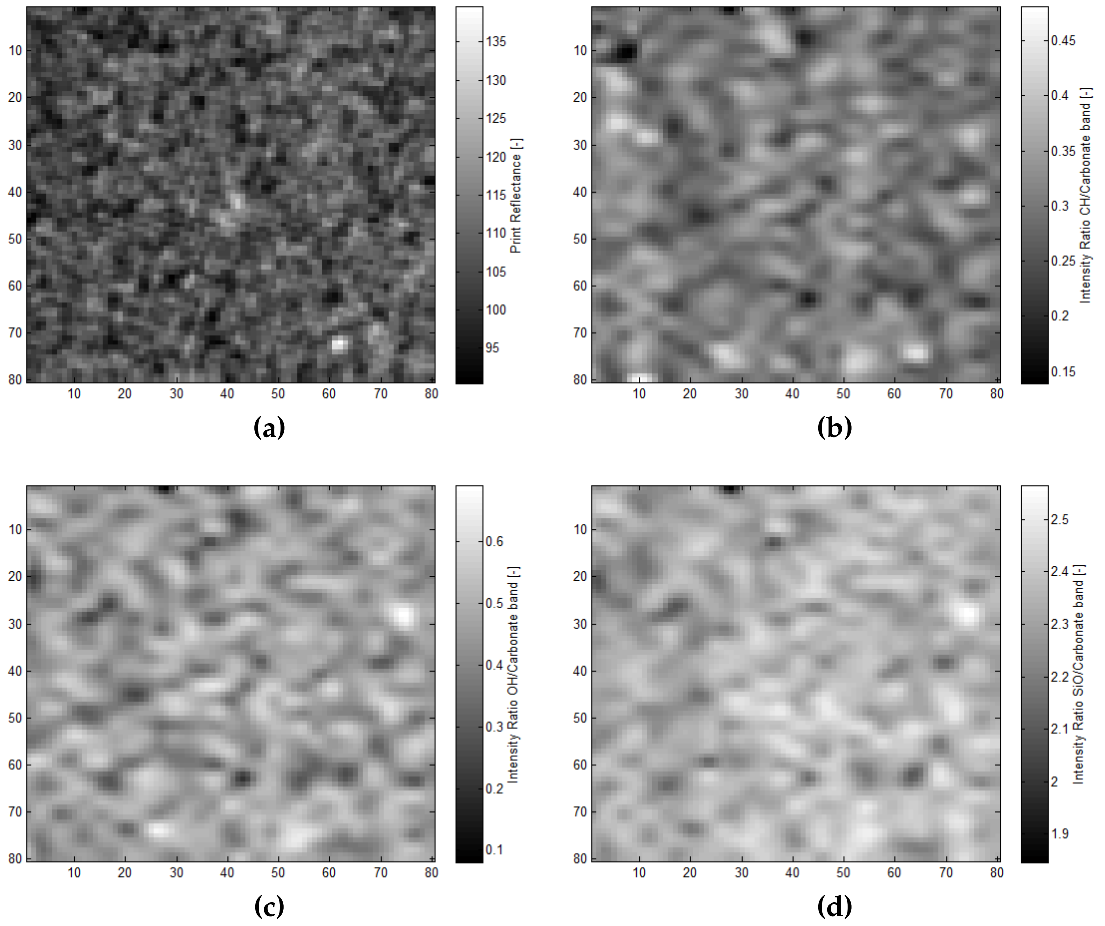

(a) **(b)** **(c)** **(d)**

Figure 5.9 Images of the Gaussian blurred samples of **(a)** the printed sample (i.e. 100 % cyan and 60 % magenta, **(b)** the ratio of latex (i.e. CH band) to calcium carbonate (i.e. CO_3^{2-} band) intensity images, **(c)** the ratio of kaolin (i.e. OH band) to carbonate and **(d)** the ratio of kaolin (i.e. SiO band) to carbonate (size of images: 7 mm × 7 mm).

of latex to calcium carbonate was supposed to give information about the binder concentration on the coating layer, whereas the ratio of kaolin to calcium carbonate give information about the surface distribution of kaolin in the coating layer.

The intensity ratios of latex/carbonate **(b)** and kaolin/carbonate **(c)** indicate that the variance in those images was lower than compared to the kaolin/carbonate ratio in **(d)** (see scale bars in Figures 5.9b–5.9d). It can be seen that specific features were similar in the ratios, which means that they are correlated to each other. However, it can be observed from Figure 5.9 that there seems to be low accordance between the printed image and the intensity ratios.

Figure 5.10 depicts the result plot for the multiple linear regression analysis for the colour field 100 % cyan and 60 % magenta. Two samples of each reference sample

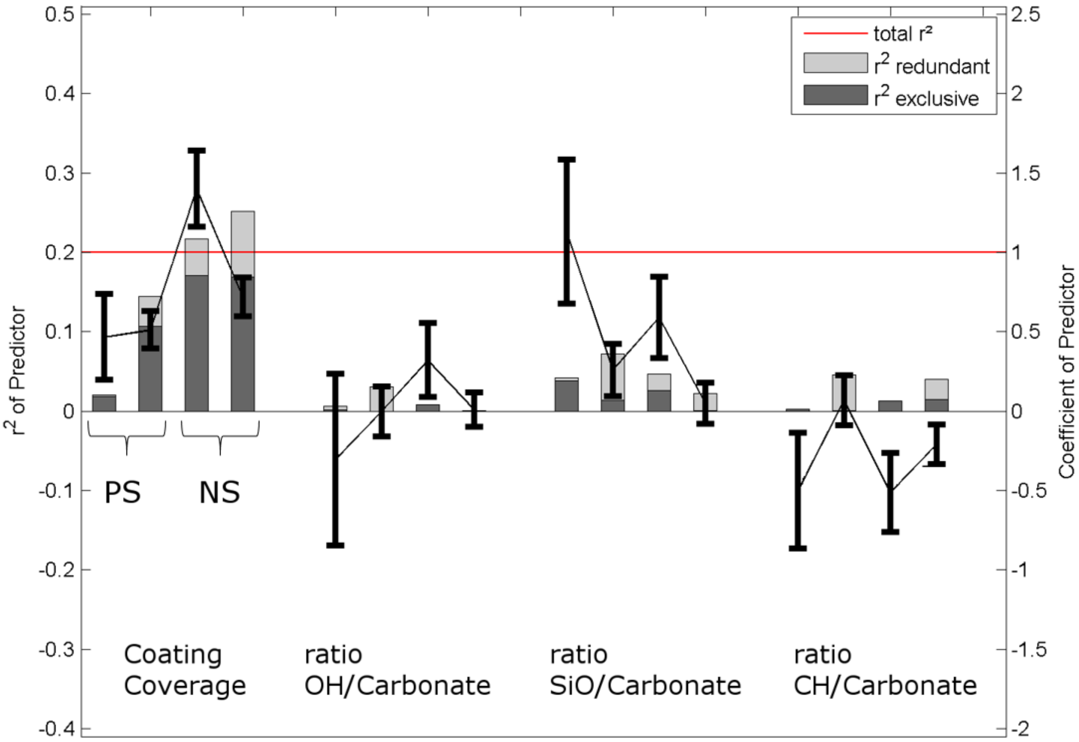

Figure 5.10 Result of the ATR IR spectroscopy for colour field 100 % cyan and 60 % magenta.

(**PS** and **NS**) are in the model and four paper properties were used as predictors. The three intensity ratios as exemplary shown in the images above and the coating coverage measured in the same way as described for the large samples. The first two bars of each predictor are the r^2_{alone} values for the positive reference sample **PS**. The second two bars are the r^2_{alone} values for **NS**. The red line shows a mean *total* r^2 for all four models of 0.20.

The results illustrated in Figure 5.10 indicate that print reflectance was explained by the intensity ratios to a low extent (r^2<0.10). As b is changing signs, the predictor is not reliable, which means that the correlation was more likely to be a coincidence. At least one modelling result in each intensity ratio exhibited a non reliable correlation.

Coating coverage was taken as a reference for the reliability of the modelling results. When comparing the **PS** and **NS** results for colour field 100 % cyan and 60 % magenta in Figure 5.10 to the results in Figure 5.8, a difference in the r^2_{alone} can be observed. r^2_{alone} for **NS** in Figure 5.8 for the predictor coating coverage was around 0.50, but in Figure 5.10 r^2_{alone} for **NS** was between 0.20 and 0.25. Similarly the r^2_{alone} for **PS** were comparable lower. This difference reveals that the sample size heavily affects the obtained results. It might possibly be, that the examined 7 mm × 7 mm area was located on a paper property feature of similar size and therefore, no valuable information could be obtained.

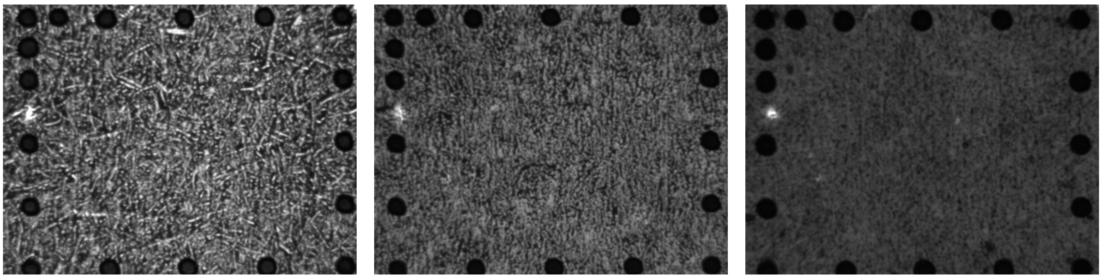

(a) MS **(b) PS** **(c) NS**

Figure 5.11 Images obtained from PST measurements of **(a)** one matte sample, **(b)** one positive reference sample and **(c)** one negative reference sample (size of image: 10 mm × 9 mm).

As a consequence the result shown, do not provide a conclusive result. On the one hand, the variation of the intensity ratios of latex and/or kaolin really do not explain the variations in print reflectance as stated by Kenttä et al. (2006). On the other hand, the coating coverage indicates that the sample size could have hidden the correlation.

5.4.2 Topography under Load in Sheet Fed Offset Printing

The topography under load was examined with the Print Simulation Tester (PST) introduced by Boström (2012). The measurements were performed according to the principle shown in Section 2.6 Topography under Load. The nip load was 1.9 MPa and the dwell time was 5 ms. The size of the captured image by the PST was 10 mm × 9 mm and the pixel size was 17 µm per pixel. The finally evaluated sample size was 7 mm × 7 mm. Figure 5.11 shows three samples of PST measurements. Brighter areas in the image represent compressed, elevated areas. The laser marks are black due to no contact. It is apparent that the low calendered sample (i.e. Fig. 5.11a **MS**) exhibits more pronounced fibrous features compared to **PS** and **NS**. The reason for that is, that calendering evens out the surface and the elevated structures disappear.

Before performing the PST measurements, the local paper properties basis weight, coating coverage and macroroughness were measured for reliability reasons. The print trial set up was the same as for the previous described print trials for sheet fed offset printing. The samples were printed with two colour fields. On the one hand the 100 % cyan and 60 % magenta and on the other hand the 80 % black colour field. After printing the obtained images were registered and subsequently post processed by a Gaussian blur in the same way as described for the ATR IR samples (see Section 5.4.1).

Figures 5.12 and 5.13 depict the results of the multiple linear regression analysis for the samples. For each paper grade (i.e. **MS**, **PS** and **NS**) three samples were

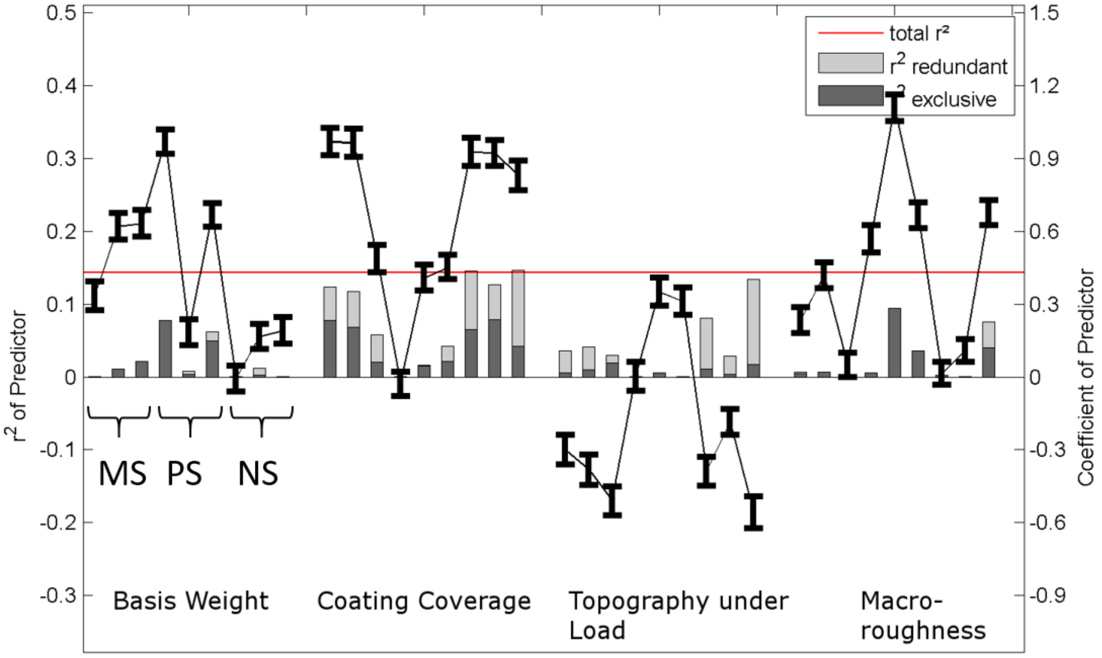

Figure 5.12 Result plot for the colour field 100 % cyan and 60 % magenta.

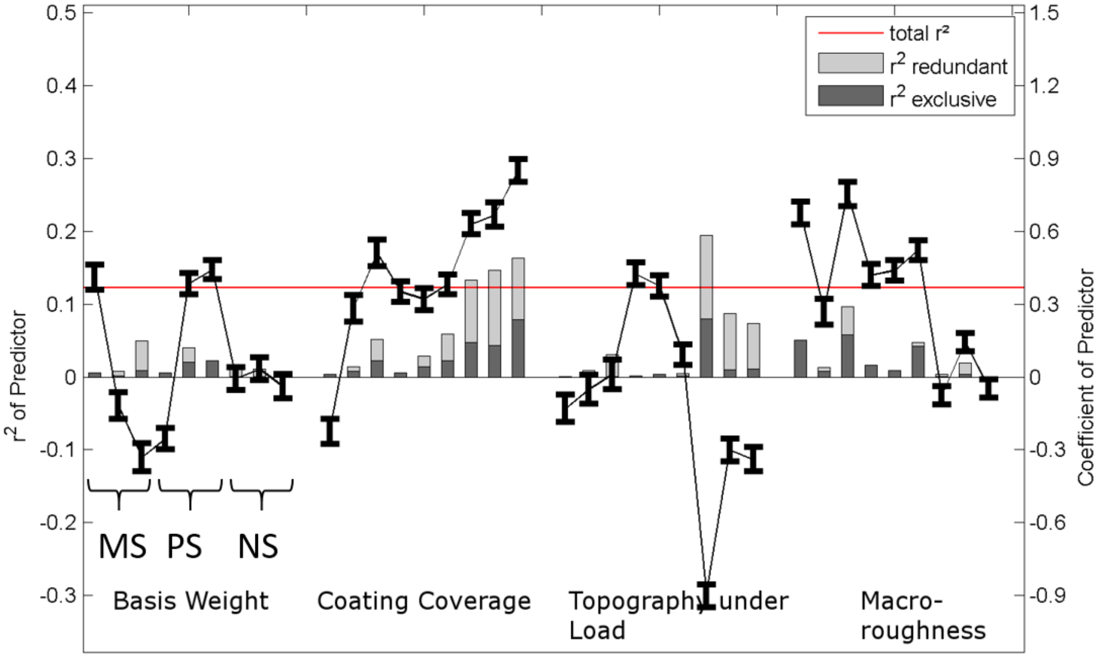

Figure 5.13 Result plot for the colour field 80 % black.

measured. The first three bars represent the r^2_{alone} for **MS**, the second three, the r^2_{alone} for **PS** and the last three, the r^2_{alone} for **NS**.

Both result plots show, that variations in topography under load explained the variations in print reflectance to a rather low and redundant extent. Except for **NS** the contribution was negligible. Still, for **NS** this means that only 0.04–0.20 of the variation in print reflectance could be explained by variations in topography under load. The coefficient of the predictor b was negative, which indicates, that more compressed areas (i.e. areas brighter in the PST image) were correlated to regions with low print reflectance. This information fits with the results of the bigger examined samples in Section 5.4 where elevated regions corresponded to regions of low print reflectance.

When looking at the paper properties measured for reliability reasons it is obvious, that the contribution was lower than compared to the r^2 in result plots calculated for the bigger samples (see Figures 5.8 and 5.7). This was especially the case for coating coverage which explained around 0.50 of the print reflectance variation for **NS**. Therefore, the small sample size available for the PST measurements was not as representative as compared to the big sample size (i.e. 38 mm × 38 mm compared to 7 mm × 7 mm).

5.5 Conclusion

Print mottle in sheet fed offset printing was examined for three different paper grades (matte **MS** and gloss **PS**, **NS**) on three different colour fields (40 % cyan, 80 %, black and the mixed field 100 % cyan and 60 % magenta). Twelve paper properties were locally measured before printing (see Tab. 5.4). In order to in explain print mottle, a band pass filter was applied in the region of interest for print mottle (i.e. wavelength band of 2 mm to 8 mm). However, filtering was not applicable for the smaller samples, which were used for the ATR IR and PST measurements.

Intensity ratios of latex/carbonate and kaolin/carbonate were examined on the smaller samples for **NS** and **PS**. The multiple linear regression analysis lead to ambiguous results. Either the sample size was too small or the binder distribution did not cause print mottle. Similarly, topography under load explained the variation in print reflectance only to a very low extent. Furthermore, taking into account the reference measurements, the analysis of the relationship between topography under load and print mottle confirmed, that the sample size influences the results.

For the larger samples and for low tone values, it was shown that brightness plays a role, due to optical dot gain. This effect decreased with increasing tone value. Calendering diminishes surface porosity at elevated areas and thus, variations in coating coverage and refractive index as well as thickness variations are more emphasised. The results showed, that areas of lower surface porosity, lower coat weight, higher gloss, elevated and thus, thicker exhibited higher amounts of ink.

Furthermore, it was shown that for **NS**, 0.55 of the variation in print mottle was explained by the measured local paper properties. The leading predictors were, in descending order, coating coverage, gloss, thickness variation, refractive index and brightness. Although, the basis weight of paper is interrelated with the measured paper properties it was not observed in the obtained results. In addition, the results revealed the magnitude of exclusive information contributed by the paper properties.

Chapter 6

Memory Effect

The main part of this chapter consists of the publication Fuchs et al. (2015a), where the phenomenon of the so called memory effect was introduced and described. The basic idea of this survey was to study back-trap mottle and its relationship to the previous printed sheet. The hypothesis was that the local paper properties of the previous printed sheet would influence the print mottle on the consecutive sheet. This was not observed. Instead, it was found, that the print mottle of the consecutively printed sheets is correlated.

6.1 Background

Mottling as mentioned in Section 1 is defined as an undesired unevenness in perceived print colour, print density or print gloss. An evenly printed image is assumed to be generated due to a perfect interaction of the three main components involved during the printing process, namely the printing press, the printing ink and the substrate (i.e. paper). Print mottle is the result of an imperfect interaction between any of the three components which leads to uneven transmission or absorption of the printing ink and thus to print mottle.

Depending on the phenomena causing the imperfect interaction, there are three common types of mottle: back-trap mottle, water interference mottle and ink-trap mottle (Sadovnikov et al., 2008). Besides this definition, Fahlcrantz (2005) divided print mottle into two components: a systematic and a stochastic component. The stochastic component of print mottle describes the randomly distributed noise in the final print. This random pattern is often accompanied by a systematic component. The systematic mottle component is perceived as a structured pattern, it can be caused by vibrations of the printing machine (Krzyzkowski and Pyryev, 2011) or by periodic structural patterns in the paper like wire marks (MacGregor and Conners, 1987).

In the study of Fuchs et al. (2015a) a new type of mottle was investigated: Time stable, stochastic mottling patterns which occur repeatedly over a long series of printed sheets. This was called memory effect in print mottle, because some mottle structures seem to be remembered over time. As an example refer to Figure 6.4 where two consecutively printed sheets show identical mottle features in the exact same location of the printed colour field. The key point was, that a time stable mottle pattern at fixed positions occurring in consecutively printed sheets indicated that the printing press is also involved in the development of the print mottle. It can be speculated that this type of mottle might result from some local modifications of the rubber blanket or the printing plate that systematically change the ink transfer in certain positions. A a stochastic variation during the printing process, such as random ink-surface adhesion failure, can be ruled out, because of the systematic occurrence of the patterns (Alm et al., 2015). The work did not focus on finding the reasons for such location and time stable mottle patterns but introduced a method capable to capture and quantify this memory effect, i.e. the similarity between the mottling patterns in consecutively printed sheets.

6.2 Paper Samples

The examined paper samples were commercial glossy wood free coated (WFC) paper grades. The samples were divided into three groups: a standard WFC paper ($135\,\mathrm{g/m^2}$), coat weight per side $31\,\mathrm{g/m^2}$ and two reference samples (also WFC: $115\,\mathrm{g/m^2}$, coat weight each side $24\,\mathrm{g/m^2}$). The first reference sample was referred to be of good print quality, denoted as WFC+ and the second reference sample was referred to be of bad print quality, denoted WFC-.

6.3 Printing and Sample Handling

For evaluation of the memory effect two print trials (denoted as A and B) were performed. All paper samples were printed on a 6 colour Heidelberg SM XL 8 sheet fed offset press with a printing speed of 8000 sheets per hour. The printing plates used were AGFA Amigo. The ink used for the print trial was a NOVAVIT® Supreme Bio and the rubber blanket was a Continental® SP Evolution. The colour sequence was key black (K), cyan (C), magenta (M), yellow (Y), pantone blue (P) and last black (B).

Print Trial A

In this trial only one type of WFC paper (i.e. the standard WFC paper) was printed. First 1000 sheets of standard WFC paper ($135\,\mathrm{g/m^2}$) were printed with 6 colours. The printing machine was stopped and the last printing unit (B) was lifted off. Afterwards 100 sheets with 5 colours were printed. The same procedure was performed for the remaining printing units. As a result, a stack of 1500 sheets consisting

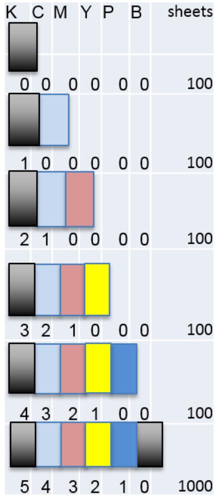

Figure 6.1 Print trial A. The stack of printed sheets obtained from the trial. The numbers below the colours represent the amount of back-traps of one colour.

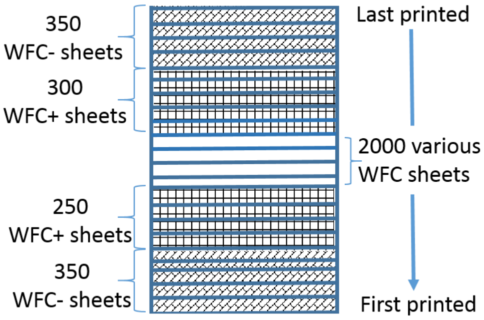

Figure 6.2 The stack of sheets obtained from print trial B.

of 100 sheets (K), 100 (K+C), 100 (K+C+M), 100 (K+C+M+Y), 100 (K+C+M+Y+P) and 1000 sheets with all six colours was obtained. Figure 6.1 shows the obtained stack and the numbers underneath the colour represent the amount of back-traps of one colour.

After printing the paper sheets were scanned and the mottle patterns were analysed. From the first 1000 sheets (printed with all 6 colours, i.e. the bottom part of the stack in Figure 6.1), 3 sheets every 50th sheet (1,2,3,51,52,53,101,102,103 . . .) were selected. From the sheets printed with 1 to 5 colours (Figure 6.1, upper part of the stack), 3 sheets every 15th sheet (1,2,3,15,16,17,30,31,32, . . .) were selected. From each selected sheet five different colour fields were scanned: 40 % tone value C, 100 % C, 80 % K, 80 % B and the mixed colour field 100 % C/60 % M. A flatbed scanner (Epson Perfection 4990®) at 1200 dpi (i.e. 21.17 µm/pixel) resolution was used for image acquisition.

Print Trial B

Within this trial one grade with good print quality (WFC+) and one grade with poor print quality (WFC-) was printed on the same printing machine (i.e. Heidelberg SM XL 8). These papers were printed with 6 colours at 8000 sheets per hour. First 350 sheets of WFC- and then 250 WFC+ sheets were printed. Subsequently 2000 sheets of various other WFC papers which were not examined, were printed. Finally, again 300 WFC+ sheets and 350 WFC- sheets were printed (see Figure 6.2).

After printing, the paper sheets were scanned and the mottle patterns were analysed. From each printed WFC- and WFC+ stack the 10 first printed sheets and 10 last printed sheets were selected (e.g. for the first printed WFC- stack: 1,2, . . . 9,10,341,342,

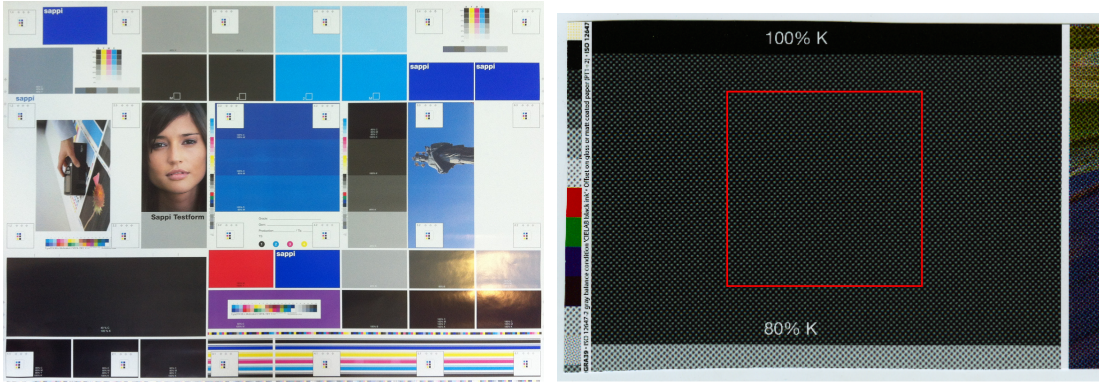

(a) Test print form.

(b) Colour field 80 % K from the print test form with extracted image region (size of red square: 50 mm × 50 mm).

Figure 6.3 Illustration of the test print form **(a)**. From each sheet a defined part from a colour field is extracted, here the 80 % K colour field **(b)**.

. . . 349,350 and for the first printed WFC+ stack: 1,2, . . . 9,10,241,242, . . . 249,250). From each selected sheet the same colour fields were scanned and examined as for print trial A.

6.4 Image Analysis

An example of the print form containing all colour fields used for this work is shown in Figure 6.3a. Figure 6.3b depicts an 80 % K colour field which shows the size of the finally examined area (50 mm × 50 mm; red square).

For image analysis, first the exact same region of a scanned colour field was extracted from consecutive sheets using image registration. Image registration was according to the description in Section 2.1 and Hirn et al. (2008). The images were registered by applying a shape preserving coordinate transform where the edge points of the colour fields were used as registration marks, because they precisely indicate a constant position on the blanket and the printing plate.

After registration, a set of images showing exactly the same regions in the colour fields for all printed sheets was available. Figure 6.3b shows one image of a registered 80 % K colour field. From these images, a sub-image was extracted from every sheet resulting in a set of sub-images, which was then used for analysis. The final size of the analysed sub-images was 50 mm × 50 mm (i.e. the size of the square in Figure 6.3b).

After extraction, the sub-images of all samples were descreened and then post processed in two different ways. On the one hand, spectral filtering (i.e. a FFT pass band filter) was performed by a pass band filter in the wavelength band of 1 mm to 16 mm. The region of interest for visual perception of print mottle is located in the

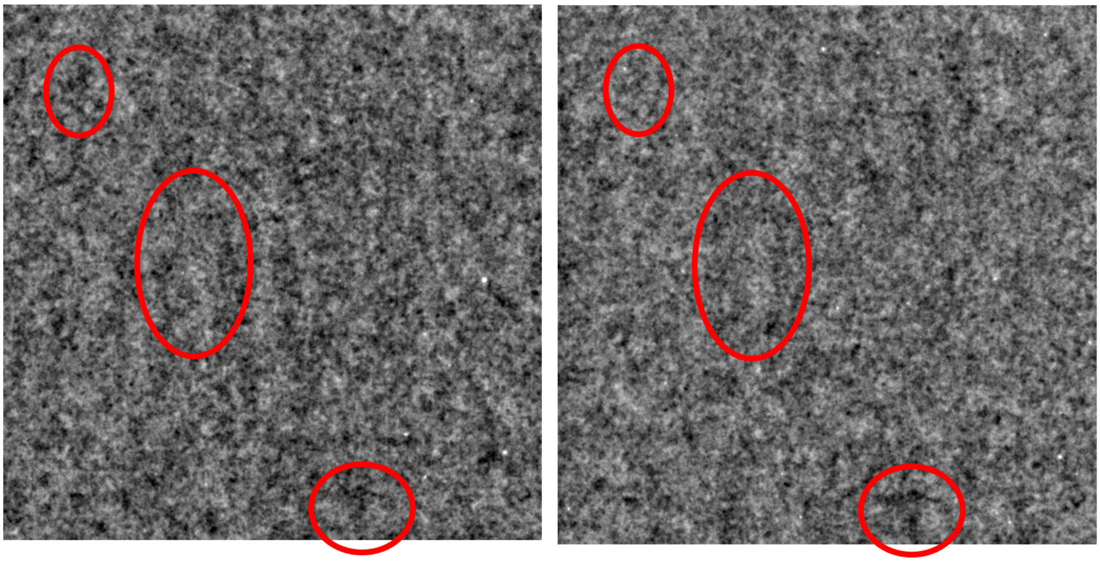

(a) Extracted image region from sheet #1000. **(b)** Extracted image region from sheet #1001.

Figure 6.4 Example of two contrast enhanced images extracted from two 80 % K regions of consecutively printed sheets (print test A). The images were spectral filtered (wavelength band 1 mm to 16 mm). Some mottling features occurring in exactly the same location in both prints are highlighted by ellipses (size of images: 50 mm × 50 mm).

wavelength band of 1 mm to 16 mm, which also contains the 2 mm to 8 mm wavelength band. This type of filtering produces images where only the structures most relevant for print mottle are preserved.

On the other hand, the images were rescaled to a pixel size of 250 µm. That is the size of structures, which the human eye can resolve under good illumination at a viewing distance of 30 cm (Olzak and Thomas, 1986). Hence, at a pixel size of 250 µm all structures perceived by the human eye are preserved. The final result of scanning, filtering and rescaling can be seen in Figure 6.4. It shows two images 80 % K fields from consecutively printed sheets which were spectral filtered in the relevant region for print mottle, the images were extracted as described above and indicated in Figure 6.3b. The images are contrast enhanced for better visibility.

In order to evaluate the location and time stability of the mottle pattern, the similarity between the extracted images was quantified. Point wise correlation of the registered images (compare Section 2.1), where the coefficient of determination (R^2) was the resulting measure of similarity between the images, was applied. The coefficient of determination explains how much of the variance in one data set is explained by another (or several other) data set(s) (Neter et al., 1996). A value of $R^2 = 1$ between two images indicates that the mottle pattern in these prints was exactly the same, a value of $R^2 = 0$ indicates that there was no similarity at all. Analysis of R^2

$$\begin{bmatrix} R^2{}_{11} & R^2{}_{12} & R^2{}_{13} & \dots & R^2{}_{1n} \\ R^2{}_{21} & R^2{}_{22} & R^2{}_{23} & \dots & R^2{}_{2n} \\ R^2{}_{31} & R^2{}_{32} & R^2{}_{33} & \dots & R^2{}_{3n} \\ \dots & \dots & \dots & \dots & \dots \\ R^2{}_{m1} & R^2{}_{m2} & R^2{}_{m3} & \dots & R^2{}_{mn} \end{bmatrix}$$

(a) Structure of the R^2 matrix.

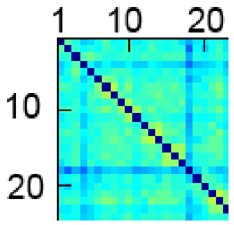

(b) Example of the upper left part of a R^2 matrix.

Figure 6.5 Structure **(a)** and an example of a section **(b)** of an R^2 matrix.

was performed for both types of images, i.e. the pass band filtered and the rescaled images.

The similarity between the images is displayed in R^2 matrices for each colour field. The structure of the matrix is shown in Figure 6.5a. The indices m and n, which indicate the images correlated to each other, are in accordance with the order of the selected stack of printed sheets from bottom (first printed) to top (last printed). For example in print trial A, indices 1 to 3 represent the images of the first three printed sheets in the stack. The consecutive three indices (i.e. 4-6) represent the 51st to 53rd printed sheet, because 50 sheets are skipped in between (see description of print trial A). As a consequence, the last three indices (i.e. n-2, n-1 and n) represent the last three printed sheets (i.e. the top of the stack in Figure 6.1). Thus, R^2_{12} represents the correlation between the image of the first and the second printed sheet. The square matrix (m = n) is symmetric since R^2_{12} and R^2_{21} are identical because the similarity is equal in both directions. An example of a section of a R^2 matrix is displayed in Figure 6.5. The main diagonal represents R^2 values between one and the same image (e.g. R^2_{11} or R^2_{22}). As this is the similarity between one and the same image, R^2 is 1 for the main diagonal, it was set to 0 for better visibility.

For print trial B the structure of the R^2 matrix is similar. Since sampling was a little different compared to print trial A, the first 10 indices (n = 1-10) represent the images of the first 10 printed sheets of WFC- (i.e. at the bottom of the whole stack in Figure 6.2, sheet 1-10) and the next 10 indices (n = 11-20) the images of the 10 last printed sheets of WFC- (i.e. at the top of the bottom WFC- stack in Figure 6.2, sheet 341-350). This allocation applies also for the other WFC+ and WFC- samples of the stack obtained from print trial B.

The variance (i.e. squared standard deviation) of each image was also calculated and depicted on top of the R^2 matrices (Figure 6.6 to Figure 6.10) and is a measure for the print unevenness in the image. A lower variance indicates lower print unevenness, whereas a higher variance indicates a higher print unevenness. Thus, not only the similarity between the print mottle patterns in the images can be quantified, but also the development of print unevenness over time is captured.

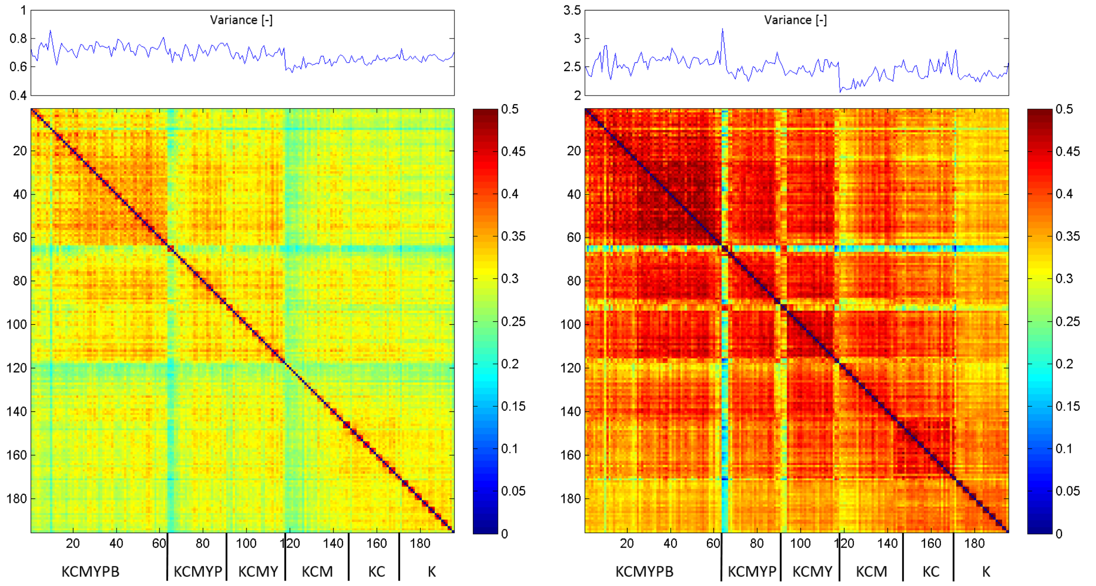

(a) Colour field 80 % K, 1-16 mm.

(b) Colour field 80 % K, 250 µm.

Figure 6.6 R^2 matrices of colour field 80 % K. In **(a)** images were spectrally filtered (wavelength band 1-16 mm) and in **(b)** the images were rescaled to a pixel size of 250 µm. The line plot with the variance on top of the similarity matrices shows the print unevenness (i.e. the variance) for each of the printed sheets.

6.5 Results Print Trial A

In this print trial the printing units were lifted off one after the other. In Figure 6.6a and 6.6b the R^2 matrices for the colour field 80 % K are depicted. Figure 6.6a shows the matrix where all images were spectrally filtered within the wavelength band 1 mm to 16 mm, whereas the images in 6.6b were rescaled to a pixel size of 250 µm. Above the R^2 matrices the variance of each image is plotted. Below the matrix, the printing units which were active are shown. The sequence is the same as the order in Figure 6.1 (bottom to top implies first printed to the last printed). Thus, KCMYPB means that all printing units were active and K means only the K unit was active.

Figure 6.6 reveals that the print mottle of one sheet is related to the print mottle of other sheets. It shows further that the print mottle is persistent for a rather long period of printed sheets. The correlation drops after a printing unit has been lifted, especially after lifting B and Y. However, when restarting printing after lifting off, the similarity of the print mottle again rises, which means that after a brief interruption due to the lifting of a printing unit some part of the earlier mottling structure reappears in the print. This systematic re-occurrence of mottling patterns over a large amount of printed sheets was termed memory effect.

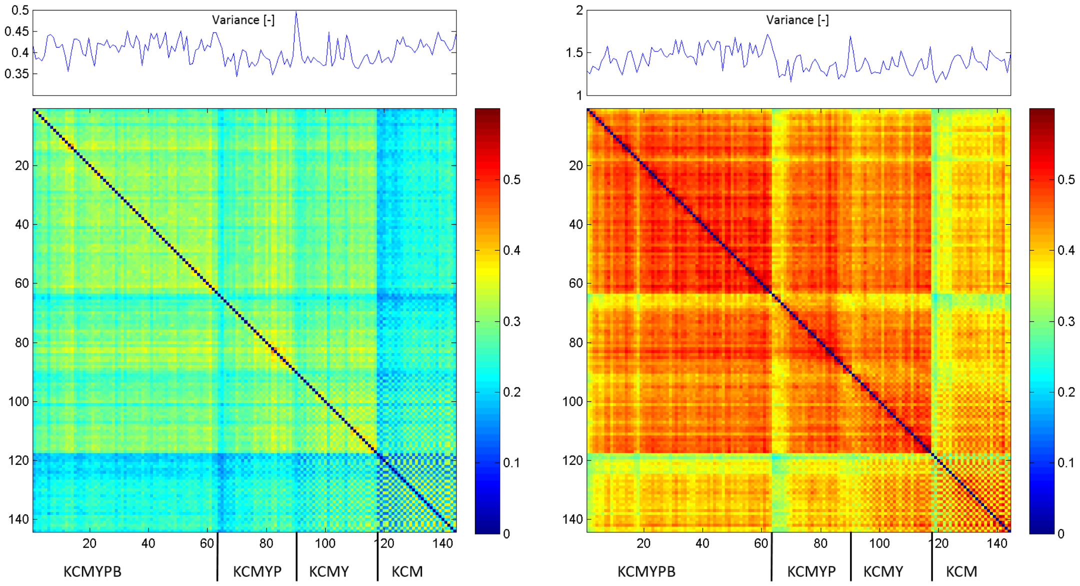

(a) Colour field 100 % C/60 % M, 1-16 mm. **(b)** Colour field 100 % C/60 % M, 250 µm.

Figure 6.7 R^2 matrices of colour field 100 % C/60 %. In **(a)** images were spectrally filtered (wavelength band 1-16 mm) and in **(b)** the images were rescaled to a pixel size of 250 µm.

The correlation between two images is higher when they are located close to each other, i.e. when they have been printed shortly one after another. In the R^2 matrices, R^2 values of images printed close to each other in time, are located in the plot region surrounding the main diagonal. The highest correlations were found in the R^2 matrix with the rescaled images (Figure 6.6b). There, R^2 is close to 0.50. R^2 is lower in the region of interest for print mottle (1-16 mm wavelength band, Figure 6.6a). However, even after 1000 sheets the R^2 between the print mottle of the first and the last sheet is still close to 0.35. It seems, that there is an inherent print mottle which is continuously re-occurring.

Furthermore, Figure 6.6 shows that the variance (i.e. print unevenness) decreases after lifting of the printing units, especially after lifting B and Y. This agrees with the common notion that print unevenness decreases with decreasing number of back-traps.

Figure 6.7 shows similar results for the mixed colour field 100 % C/60 % M. R^2 is stable for a rather long period of time. It is up to 0.55 when looking at the rescaled images (Figure 6.7b). For the regions of interest for print mottle (Figure 6.7a, 1-16 mm wavelength band), R^2 is up to 0.40. The correlation decreases after lifting the B, P and Y printing units and increases again with further printing. When printing KCM, an alternating pattern seems to occur which is shown by the alternating, checkerboard pattern, R^2 in the KCM part of the matrix in Figure 6.7a and 6.7b. This means that the

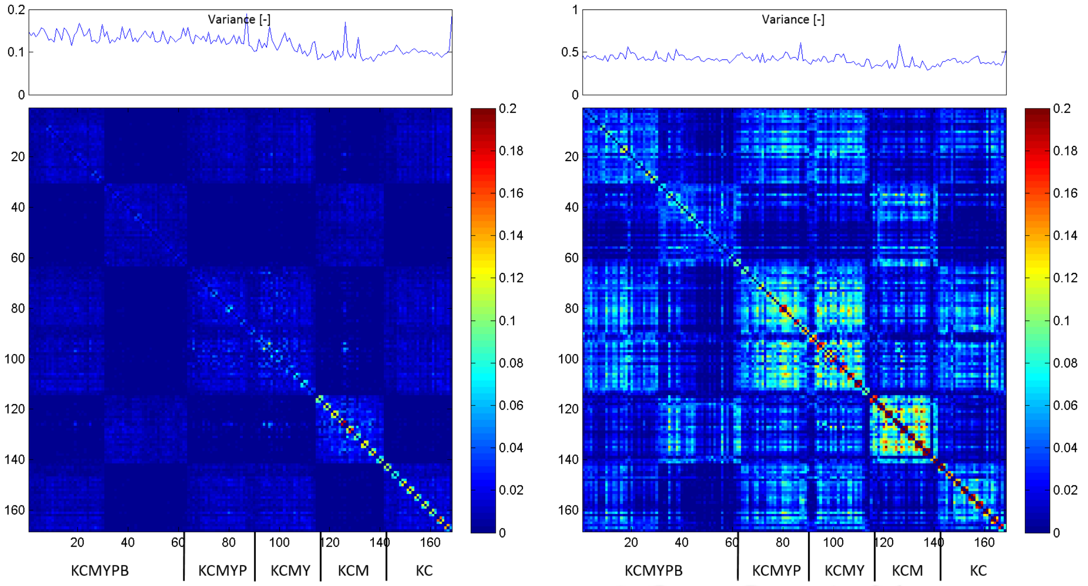

(a) Colour field 100 % C, 1-16 mm.

(b) Colour field 100 % C, 250 µm.

Figure 6.8 R^2 matrices of colour field 100 % C. In **(a)** images were spectrally filtered (wavelength band 1-16 mm) and in **(b)** the images were rescaled to a pixel size of 250 µm.

similar print mottle does not occur on every consecutive sheet, but on every second or third sheet, suggesting that the phenomenon is either unstable or related to a patterning on the original paper tambour.

The print unevenness decreases when lifting B, but increases when lifting Y. Usually print unevenness is expected to decrease with decreasing amounts of backtraps, but in Figure 6.7a the variance has the same level when comparing KCM and KCMYPB. The reason for this is unclear.

The results for 40 % C and 80 % B reveal findings similar to the 80 % K and 100 % C/60 % M fields and are not shown here. In contrast, however, the R^2 matrices of the full tone 100 % C present different results (see Figure 6.8a and 6.8b). There is little to no correlation (only up to 0.15) between the images. Furthermore, the low correlation is only stable for about 3 printed sheets in a row. This suggests, that the time stable and re-occurring print mottle is not a problem for full tone printing.

6.6 Results Print Trial B

In print trial B stacks of WFC+ and WFC- samples were distributed in an entire stack (compare Figure 6.2). Below the matrices in Figure 6.9a and 6.9b the order of the distributed samples in the printed stack is described. Firstly, the R^2 of the 10 first and 10 last printed WFC- samples, immediately afterwards R^2 of the WFC+ samples and

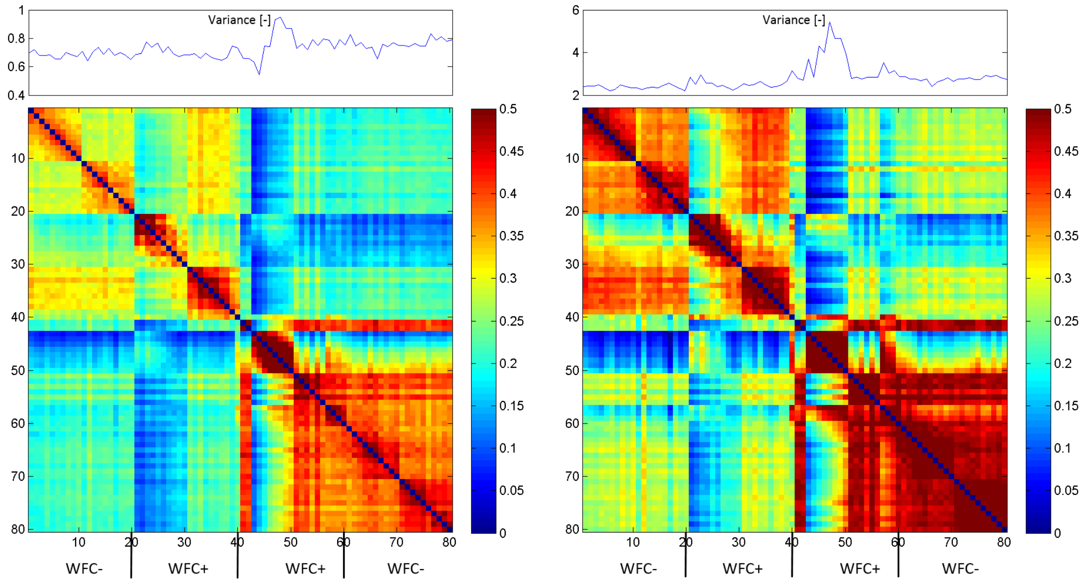

(a) Colour field 80 % K, 1-16 mm.

(b) Colour field 80 % K, 250 µm.

Figure 6.9 R^2 matrices of colour field 80 % K. In **(a)** images were spectrally filtered (wavelength band 1-16 mm) and in **(b)** the images were rescaled to a pixel size of 250 µm.

secondly the R^2 of the WFC+ and WFC- samples again. As shown in Figure 6.2, there were approximately 2000 sheets of various WFC grades (Figure 6.9a and 6.9b between number 40 and 41) between the two WFC+ stacks.

The print mottle pattern for the first 10 WFC- sheets (see Figure 6.9a and 6.9b, numbers 1-10) show values of an R^2 up to 0.45 and similarly for the last 10 sheets printed in the first stack (see Figure 6.9a and 6.9b, numbers 11-20). Since there were 350 WFC- sheets printed, this tells us that R^2 decreases from the beginning to the end of the stack which can be seen in the R^2 matrix where the images of numbers 11-20 are correlated to numbers 1-10. These findings are similar to those of the second stack (WFC+). Within 10 sheets the correlation is higher, and subsequently decreasing when reaching the end of the stack. However, there is also a correlation between the print mottle observed in the WFC- and WFC+ images (up to 0.37).

At the beginning of the second WFC+ stack there seems to appear a print defect. It can be seen as a sharp rise in variance at number 43 in the similarity matrix. The 3rd to 10th image (in the second WFC+ stack) are highly correlated to each other, but not to the rest of the stack. It can also be seen in the variance of the images. The variance is higher as compared to the rest of the images. After disappearance of the print defect, the R^2 between the 10 last images of the WFC+ stack and the images of the WFC- stack is very stable. There is even a correlation between the sheets printed at the beginning and after 3000 sheets which is shown by the upper right part of the R^2 matrices (Figure 6.9a: 0.20, and Figure 6.9b: 0.25). R^2 is higher for the rescaled

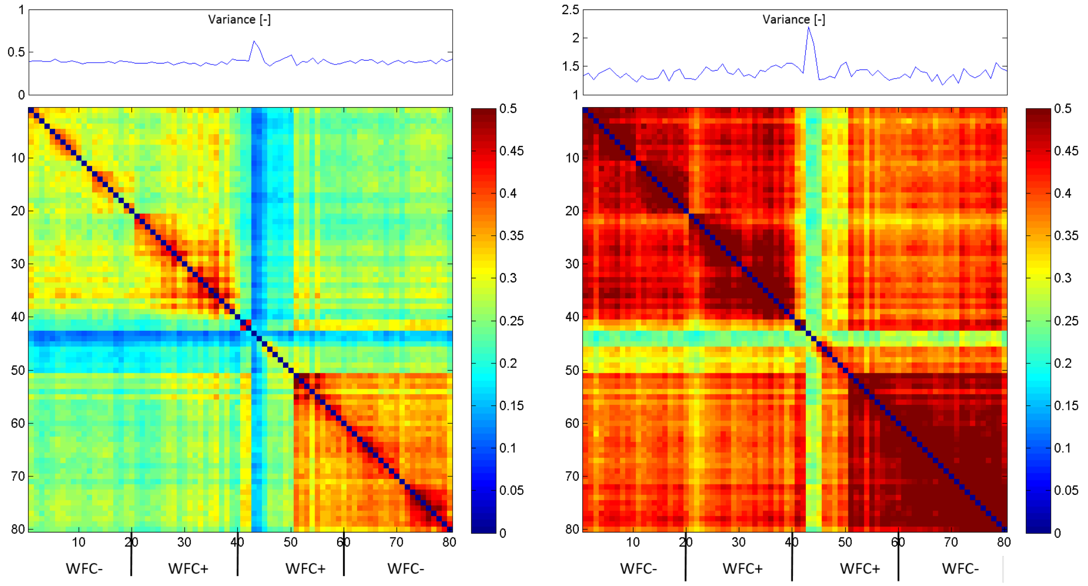

(a) Colour field 100 % C/60 % M, 1-16 mm. **(b)** Colour field 100 % C/60 % M, 250 µm.

Figure 6.10 R^2 matrices of colour field 100 % C/60 %. In **(a)** images were spectrally filtered (wavelength band 1-16 mm) and in **(b)** the images were rescaled to a pixel size of 250 µm.

filtered images (Figure 6.9b, 250 µm) and is a little lower in the relevant wavelength for print mottle (Figure 6.9a, wavelength band 1-16 mm).

Figure 6.10 shows the R^2 matrices for 100 % C/60 % M. For the first stack of WFC- and WFC+ the correlation is higher for the images of the sheets printed close to each other in time. R^2 is lower for the images which are printed with hundreds of sheets in between, but it is stable. These R^2 matrices again show the print defect at element 43 in the second WFC+ stack. The variance in Figure 6.10a and 6.10a is higher where the print defect occurs. However, the print defect disappears, because the images printed afterwards correlate with the first printed ones again. It is apparent from Figure 6.10 that R^2 is higher than 0.50 for the rescaled images (Figure 6.10a, 250 µm) and up to 0.50 for the print mottle wavelength band (Figure 6.10a, wavelength band 1-16 mm).

The results for the other colour fields (80 % B and 40 % C) are similar to those presented above. Also, like in the previous print trial A, the 100 % C field shows little to no correlation, similar to Figure 6.8. These findings suggest that the print mottle of these images is not only time stable and re-occurring within one paper grade, but is also stable over various paper grades. So far, the origin of this time stable and re-occurring effect (i.e. the memory effect) con only be suspected to have its origin in the rubber blanket or the printing plate of the sheet fed offset machine.

6.7 Conclusion

A method that quantifies the degree of similarity between the mottling patterns in consecutively printed sheet fed offset sheets was introduced. The similarity between the prints was measured using point wise correlations, it was collected and displayed in R^2 matrices. The similarity of the print mottle patterns in five different colour fields was investigated. The images were examined in the relevant region for print mottle (i.e. wavelength band 1-16 mm) and in the region where all structures are perceived by the human eye (>250 µm).

The results showed that there exists a re-occurring print mottle which can be found over a large number of printed sheets. This print mottle memory effect was observed over more than 3000 copies, even when different paper grades were printed. In one printing trial the R^2 for a 100 % C/60 % M colour field was up to R^2 = 0.50 in the wavelength band which corresponds best with the human perception of print mottle. That means that up to 50 % of the mottling structure visible in this colour field was a re-occurring mottling pattern. In another trial, the correlations between the different images in the 100 % C/60 % M colour field was considerably lower with R^2 = 0.30.

The re-occurring print mottle patterns were only observed for halftone colour fields, 40 % tone value C, 80 % K, 80 % B and the mixed colour field 100 % C/60 % M, but not for the full tone colour fields.

The discussed method detects re-occurring mottle patterns appearing at fixed positions, thus it can be speculated that this mottle was related to modifications of the rubber blanket in the printing press. The remaining mottle should be related either to variations in local paper properties that lead to local variations in ink transfer and light absorption or assigned to stochastic interactions in the sheet fed offset printing process.

Chapter 7

Conclusion and Outlook

Multiple linear regression analysis was applied to evaluate print unevenness and local paper properties. This approach enabled statistical analysis and revealed the relevance and redundancy of the local paper properties. The printing techniques examined in this work were xerography –, inkjet – and sheet fed offset printing. All examined paper samples were printed on commercial printing machines. Moreover, the influence of a sheet fed offset printing machine was investigated.

Two commercial paper samples were examined and printed on two xerographic printers. The results for xerography printing revealed that variations in topography were governing the print mottle. It exhibited the highest $r^2_{exclusive}$ of all predictors. This might be attributed to the xerographic printing process. Basis weight and gloss were also capable of explaining some variations in print reflectance. It was found that elevated regions showing a higher basis weight and gloss, lead to lower print reflectance and vice versa.

For inkjet printing, pigmented and uncoated commercial paper samples were examined and printed on a high speed inkjet printing machine and an office printer. Differences between high speed – and office printing as well as the difference between pigmented and uncoated samples was shown. The results for the pigmented samples revealed the importance of variations in coating coverage (i.e. completely exclusive), brightness and opacity regarding print mottle. At higher tone values gloss and the ink penetration gained importance. For uncoated samples, variations in brightness and opacity led to print mottle in lower tone values, whereas at higher tone values, variations in basis weight explained print mottle.

In sheet fed offset printing a high impact of coating coverage on print mottle was revealed for glossy paper grades. Besides the uniformity of coating layer distribution, gloss and refractive index (i.e. surface porosity) variations helped to explain the variations in print reflectance. However, for matte samples it was shown that variations in coating coverage are not as important compared to variations in gloss and macroroughness, because of lower surface densification.

The analysis of surface binder distribution (i.e. SB latex) in case of sheet fed offset printing led to ambiguous results. There might be effects from the small sample size, or surface binder concentration was not able to explain print mottle.

Finally, by investigating the influence of the printing machine on print mottle, a method that quantifies the similarities of print mottle patterns on consecutively printed sheets was introduced. Application of this method on different colour fields demonstrated a high similarity of the print mottle patterns between half tone colour fields over more than 3000 printed sheets. Full tone colour fields were not affected by this so called memory effect. The obtained results indicated the importance of a well adjusted printing machine.

Outlook

Measurement of the present local paper properties revealed their relevance and redundancy for print unevenness. Some paper properties, mentioned hereafter, which might also be important for print unevenness, were not accessible by mapping of high resolution measurements yet.

For inkjet paper grades, it would be of interest to map the contact angle and the surface free energy in order to elucidate the influence of the hydrophilic or hydrophobic behaviour with respect to print unevenness. Mapping of contact angle measurement faces some problems, such as deformation of paper during the measurement which complicates tracking of the contact angle.

For xerographic paper grades, the measurement of local electric properties such as conductivity or impedance is not available at the moment. Due to the importance of the electric properties during the toner transfer step in the printer, it would be of utmost importance to develop such a high resolution measurement.

Furthermore, it would be of interest to examine the influence of the local surface coating colour composition on print unevenness. Attenuated Total Reflection (ATR) IR spectroscopy offers a possibility to access this, however, there are limitations regarding sample size. Another possibility to examine the local IR spectrum would be line IR cameras which permit increased sample size.

Bibliography

Alava, M. and Niskanen, K. (2006). The physics of paper. *Reports on Progress in Physics*, 69(3):669–723.

Allem, R. (1998). Characterization of paper coatings by scanning electron microscopy and image analysis. *Journal of Pulp and Paper Science*, 24(10):329–336.

Allem, R. and Uesaka, T. (1999). Characterization of Paper Microstructure: A New Tool for Assessing the Effects of Base Sheet Structure on Paper Properties. In *Tappi Coating Fundamentals Symposium*.

Alm, H., Ström, G., Schoelkopf, J., and Gane, P. (2015). Ink-lift-off during offset printing: A novel mechanism behind ink-paper coating adhesion failure. *Journal of Adhesion Science and Technology*, 29(5):370–391.

Aspler, J. (2006). Ink-water-paper interactions in printing: An updated review. volume 2006, pages 106–135.

Azimi, Y., Kortschot, M., and Farnood, R. (2009). A non-destructive method for obtaining a local coat weight map using X-ray imaging. *Journal of Pulp and Paper Science*, 35(1):11–16.

Backfolk, K., Sidaravicius, J., Sirvio, P., Maldzius, R., Lozovski, T., and Rosenholm, J. L. B. (2010). Effect of base paper grammage and electrolyte content on electrical and dielectric properties of coated papers. *Nordic Pulp and Paper Research Journal*, 25(3):319–327.

Backhaus, K., Erichson, B., Plinke, W., and Weiber, R. (2003). *Multivariate Analysemethoden*. Springer Verlag, 10th edition.

Bernié, J., Pande, H., and Gratton, R. (2004). A new wavelet-based instrumental method for measuring print mottle. *Pulp and Paper Canada*, 105(9):24–26.

Bernie, J.-P. and Douglas, M. (1996). Local grammage distribution and formation of paper by light transmission image analysis. *Tappi Journal*, 79(1):193–202.

Bliesner, W. (1970). Dynamic Smoothness and Compressibility Measurements on Coated Papers. *Tappi Journal*, 53(10):1871–1881.

Boström, B. (2012). Dynamic surface smoothness inside a printing nip. In *8th International Paper and Coatings Chemistry Symposium*.

Brander, J. and Thorn, I., editors (1997). *Surface Application of Paper Chemicals*. Blackie Academic and Professional, London, 1st edition.

Brodie, I., Dahlquis, J., and Sher, A. (1968). Measurement of Charge Transfer in electrographic Processes. *Journal of Applied Physics*, 39(3):1618–1622.

Carlsson, J., Reimers, O., and Eckl, J. (2004). Improving print quality of coated paperboard. *Wochenblatt fuer Papierfabrikation*, 132(11-12):690–697.

Chapman, S. (1954). The Chapman Printing Smoothness Tester Part I. *Pulp & Paper Canada*, 55:88–93.

Chattopadhyay, R., Bousfield, D., and Tripp, C. (2012). ATR-IR spectroscopy for dynamically measuring the effect of drying on binder migration. pages 239–249.

Chen, S., Farnood, R., Yan, N., Di Risio, S., and Song, J. (2012). Paper and printer effects on xerographic print quality. *Nordic Pulp and Paper Research Journal*, 27(4):729 – 738.

Chinga, G., Diserud, O., and Berli, E. L. (2007a). On surface details affecting the quality of commercial SC paper for gravure printing. *Nordic Pulp and Paper Research Journal*, 22(3):331–335.

Chinga, G., Eriksen, ., and Eilertsen, M. (2007b). On the suitability of desktop scanners for assessing print-through. *Journal of Pulp and Paper Science*, 33(3):125 – 132.

Chinga, G. and Helle, T. (2003). Relationships Between the Coating Surface Structural Variation and Print Quality. *Journal of Pulp and Paper Science*, 29(6):179–184.

Chinga-Carrasco, G. (2009). Exploring the multi-scale structure of printing paper - A review of modern technology. *Journal of Microscopy*, 234(3):211–242.

Cresson, T. and Luner, P. (1990). The characterization of paper formation. *Tappi Journal*, 73(12):175–185.

Dahlström, C. and Uesaka, T. (2009). New insights into coating uniformity and base sheet structures. *Industrial and Engineering Chemistry Research*, 48(23):10472–10478.

Dahlström, C., Uesaka, T., and Norgren, M. (2008). Base sheet structures that control coating uniformity: Effects of length scale. In *TAPPI Advanced Coating Fundamentals Symposium Proceedings*, pages 124–133.

Danzl, R., Helmli, F., and Scherer, S. (2011). Focus variation - A robust technology for high resolution optical 3D surface metrology. *Strojniski Vestnik/Journal of Mechanical Engineering*, 57(3):245–256.

Dickson, A. (2006). Evaluating the relationship between grammage, topography and print properties in newsprint. In *Appita Annual Conference*, volume 2006, pages 19–23.

Dickson, R., Forsström, U., and Grön, J. (2002). Coating coverage of metered size press pre-coated paper. *Nordic Pulp and Paper Research Journal*, 17(4):434–439.

Dobson, R. (1975). Burnout, a Coat Weight Determination Test Re-Examined. In *Proceedings TAPPI Coating Conference*, pages 123–131.

Duke, C., Noolandi, J., and Thieret, T. (2002). The surface science of xerography. *Surface Science*, 500(1-3):1005–1023.

Eid, A., Cooper, B., and Rippetoe, E. (2008). Characterization of mottle and low frequency print defects. In *Proceedings of SPIE - The International Society for Optical*

Engineering, volume 6808.

Elton, N. (2007a). An introduction to the surfoptic imaging reflectometer. Technical Paper 1, Surfoptic Ltd., St. Austell, Cornwall, UK.

Elton, N. (2007b). Imaging reflectometer theory. Technical Paper 2, Surfoptic Ltd., St. Austell, Cornwall, UK.

Elton, N. and Day, J. (2009). A reflectometer for the combined measurement of refractive index, microroughness, macroroughness and gloss of low-extinction surfaces. *Measurement Science and Technology*, 20(2).

Elton, N. and Preston, J. (2006a). Polarized light reflectometry for studies of paper coating structure Part I. Method and instrumentation. *Tappi Journal*, 5(7):8–16.

Elton, N. and Preston, J. (2006b). Polarized light reflectometry for studies of paper coating structure Part II. Application to coating structure, gloss and porosity. *Tappi Journal*, 5(8):10–16.

Engström, G. (1994). Formation and consolidation of a coating layer and the effect on offset-print mottle. *Tappi Journal*, 77(4):160–172.

Engström, G. (2016). Causes of back-trap mottle in lithographic offset prints on coated papers. *Tappi Journal*, 15(2):91–101.

Engström, G., Johansson, P., and Rigdahl, M. (1989). Factors in the blade coating process which influence the coating mass distribution. In *9th Fundamental Research Symposium*, pages 921–950.

Engström, G. and Rigdahl, M. (1991). Binder distribution and mass distribution of the coating layer - cause and consequence. *Tappi Journal*, (5):171–179.

Engström, G. and Rigdahl, M. (1992). Binder migration - Effect on printability and print quality. *Nordic Pulp and Paper Research Journal*, 07(2):55–74.

Eriksen, . and Gregersen, W. (2005). The influence of ink pigment penetration and paper structure on print through. *Nordic Pulp and Paper Research Journal*, 20(2):242–246.

Fahlcrantz, C. (2005). *On the Evaluation of Print Mottle*. PhD thesis, KTH Stockholm.

Fetsko, J. (1958). Printability Studies on a Survey Series of Paperboards and Coated Papers. *Tappi Journal*, 41(2):49–63.

Fuchs, W., Dauer, M., Hirn, U., and Bauer, W. (2015a). A memory effect in sheet fed offset printing. *Advances in Printing and Media Technology*, 42:35–65.

Fuchs, W., Dauer, M., Hirn, U., Bauer, W., and Steven Keller, D. (2015b). Fast evaluation of spatial coating layer formation using ultraviolet scanner imaging. *Tappi Journal*, 14(8):527–535.

Fuchs, W., Hirn, U., Bauer, W., and Keller, D. (2014). Determining the Coating Layer Distribution on Paper using UV Scanner Imaging. *Progress in Paper Physics Conference*.

Fuchs, W., Hirn, U., Bauer, W., and Keller, D. (2015c). Fast Evaluation of Spatial Coating Layer Formation using UV Scanner Imaging. *Tappi Coating Conference*.

Gate, L. and Parsons, D. (1993). The specular reflection of polarised light from coated paper. In l'Anson, S., editor, *10th Fundamental Research Symposium*, pages 263–284.

Gerstner, P. and Gane, P. (2010). Fusing of electrophotographic toner on thermally engineered coated paper. *Nordic Pulp and Paper Research Journal*, 25(1):100–106.

Gigac, J., Kasajova, M., Maholanyiova, M., Stankovska, M., and Letko, M. (2013). Prediction of surface structure of coated paper and of ink setting time by infrared spectroscopy. *Nordic Pulp and Paper Research Journal*, 28(2):274 – 281.

Goos, F. and Hänchen, H. (1947). Ein neuer und fundamentaler Versuch zur Totalreflexion. *Annalen der Physik*, 436(7-8):333–346.

Green, C. (1981). Functional Paper Properties in Xerography. *Tappi Journal*, 64(5):79–81.

Groves, R., Matthews, G., Heap, J., McInnes, M., Penson, J., and Ridgway, C. (2001). Binder Migration in Paper Coatings - A New Perspective. In l'Anson, S., editor, *12th Fundamental Research Symposium*, pages 1149–1181.

Halttunen, M., Löija, M., Vuorinen, T., Stenius, P., Tenhunen, J., and Kenttä, E. (2003). Determination of SB-latex distribution at paper coating surfaces with FTIR/ATR spectroscopy. In *Tappi Coating and Graphic Arts Conference and Trade Fair*, pages 203–211.

Heikkilä, I. (1997). Viscoelastic model of paper surface compressibility. *Paperi ja Puu/Paper and Timber*, 79(3):186–192.

Hiorns, A., Husband, J., Parsons, D., and Kent, D. (2006). Coating surface composition using ATR-IR spectroscopy. In *TAPPI Advanced Coating Fundamentals Symposium*, volume 2006, pages 58–71.

Hirn, U. (2010). Research Report F4069. Technical Report F4069, SCA RD Center, Sundsvall, Sweden.

Hirn, U., Kritzinger, J., Donoser, M., and Bauer, W. (2009a). Introducing a concept to link 3D paper structure to 2D paper properties. In l'Anson, S., editor, *14th Fundamental Research Symposium*, pages 721–747.

Hirn, U., Lechthaler, M., and Bauer, W. (2008). Registration and point wise correlation of local paper properties. *Nordic Pulp and Paper Research Journal*, 23(4):374–381.

Hirn, U., Lechthaler, M., Wind, E., and Bauer, W. (2009b). Linear regression modelling of local print density in gravure printed SC paper. In *Papermaking Research Symposium*, page 13pp.

Holik, H., editor (2013). *Handbook of Paper and Board*, volume 1. Wiley-VCH Verlag GmbH, second edition.

Hubbe, M., Pawlak, J., and Koukoulas, A. (2008). Paper's appearance: A review. *BioResources*, 3(2):627–665.

Hudd, A. (2010). *The Chemistry of Inkjet Inks*. World Scientific Publishing Co. Pte. Ltd.

ISO:2470 (2008). Paper, Board and Pulps, Part 1 (ISO Brightness) and Part 2 (D65 brightness).

ISO:24701 (2009). Paper, board and pulps - Measurement of diffuse blue reflectance factor - part 1 Indoor daylight conditions (ISO brightness).

ISO:24702 (2008). Paper, board and pulps - Measurement of diffuse blue reflectance factor - Part 2: Outdoor daylight conditions (D65 brightness).

ISO:5631 (2008). Paper and board, Determination of color by diffuse reflectance, Part 1 C/2° (2009), Part 2 D65/10° (2008) and Part 3 D50/2° (2008).

Jaehn, A. (1990). Using Panel Ranking for Rapid Discrimination of Subjective Quality Characteristics. *Tappi Journal*, 73(11):267–268.

Johansson, P. (1993). Print Mottle Evaluation by Band-Pass Image Analysis. In *Advances in Printing Science and Technology*, page 403. IARIGAI.

Järnström, L., Beghello, L., and Emilsson, P. (2010). Comparison between a curved soft tip metering element and a conventional blade in the coating of paperboard. In *Paper Conference and Trade Show*, volume 3, pages 2099–2139.

Juric, I., Randelovic, D., Karlovic, I., and Tomic, I. (2014). Influence of the surface roughness of coated and uncoated papers on the digital print mottle. *Journal of Graphic Engineering and Design*, 5(1):17–23.

Kajanto, I. (1989a). How formation should be measured and characterized. *Nordic Pulp and Paper Research Journal*, 4(3):219–228.

Kajanto, I. (1989b). The effect of formation on print quality with woodfree offset papers. *Nordic Pulp and Paper Research Journal*, 4(1):8–15.

Kajanto, I. (1991). Correlation between local amount of ink and local print density. *Journal of Pulp and Paper Science*, 17(5):178–184.

Kappel, C., Hirn, U., Donoser, M., and Bauer, W. (2008). *Annual Meeting / Pulp and Paper Technical Association of Canada*, chapter Measurement of Printing Ink Penetration in Uncoated Papers and its Influence on Print Quality, pages B539–B542.

Kartovaara, I. (1989). Coatweight distribution and coating coverage in blade coating. *Paperi ja Puu/Paper and Timber*, 9:1033–1042.

Kasajova, M. and Gigac, J. (2013). Comparison of print mottle and surface topography testing methods. *Nordic Pulp and Paper Research Journal*, 28(3).

Keller, D. and Pawlak, J. (2001). Beta-radiographic imaging of paper formation using storage phosphor screens. *Journal of Pulp and Paper Science*, 27(4):117–123.

Keller, D., Pawlak, J., Kellomäki, M., Hägglund, J.-E., and Johansson, N. (2004). Three storage phosphor systems for beta-radiographic imaging of paper. *Nordic Pulp and Paper Research Journal*, 19(2):170–175.

Kenttä, E., Juvonen, K., Halttunen, M., and Vyörykkä, J. (2000). Spectroscopic methods for determination of latex content of coating layers. *Nordic Pulp and Paper Research*

Journal, 15(5):579–585.

Kenttä, E., Pöhler, T., and Juvonen, K. (2006). Latex uniformity in the coating layer of paper. *Nordic Pulp and Paper Research Journal*, 21(5):665–669.

Kettle, J., Lamminmäki, T., and Gane, P. (2010). A review of modified surfaces for high speed inkjet coating . *Surface and Coatings Technology*, 204(12):2103 – 2109.

Kipphan, H. (2000). *Handbuch der Printmedien*. Springer.

Klein, R., Wanske, M., and Großmann, H. (2006). Measuring and evalutating the surface quality of gravure papers. In *Advances in Printing Science and Technology*.

Komppa, A. and Ebeling, K. (1981). Correlation between the areal mass and optical densities in paper. In Brander, J., editor, *7th Fundamental Research Symposium*, pages 603–633.

Krzyzkowski, J. and Pyryev, Y. (2011). Analysis of vibration of printing unit of offset printing press. *Challenges of Modern Technology*, 2(2):31–34.

Kubelka, P. and Munk, F. (1931). Ein Beitrag zur Optik der Farbanstriche. *Zeitschrift für technische Physik*, 12:593–601.

Kumpulainen, P., Mettänen, M., Lauri, M., and Ihalainen, H. (2011). Relating halftone dot quality to paper surface topography. *Neural Computing and Applications*, 20(6):803–813.

Lamminmäki, T., Kettle, J., Puukko, P., Gane, P., and Ridgway, C. (2009). Inkjet print quality: The role of polyvinyl alcohol in speciality CaCO 3 coatings. *Journal of Pulp and Paper Science*, 35(3-4):137–147.

Lamminmäki, T., Kettle, J., Puukko, P., Ketoja, J., and Gane, P. (2010). The role of binder type in determining inkjet print quality. *Nordic Pulp and Paper Research Journal*, 25(3):380–390.

Larsson, L. and Trollsas, P. (1976). Print through as an ink/paper interaction effect in newsprint. In *Trans. BPBIF Symp. Fundam. Props. Paper Related to Uses*, pages 600–612, Cambridge.

Lavrykov, S. and Ramarao, B. (2012). Thermal Properties of Copy Paper Sheets. *Drying Technology*, 30(3):297–311.

Lavrykov, S., Ramarao, B., Solimeno, R., and Singh, K. (2013). Analysis of heat and moisture transients in paper during copying and digital printing processes. *Journal of Imaging Science and Technology*, 57(6).

Le, H. (1998). Progress and trends in ink-jet printing technology. *Journal of Imaging Science and Technology*, 42(1):49–62.

Leach, R. (2010). *Fundamental Principles of Engineering Nanometrology*.

Lechthaler, M. (2007). *Bewertung des ortsabhängigen Verformungsverhaltens von SC Papier*. PhD thesis, Graz University of Technology.

Lechthaler, M. and Bauer, W. (2006). Roughness and topography - A comparison of different measurement. *Wochenblatt fuer Papierfabrikation*, 134(21):1227 – 1234.

Li, R., Zhang, Y., Yunfeng, C., and Zhulan, L. (2015). Ink Penetration of Uncoated Inkjet Paper and Impact on Printing Quality. *BioResources*, 10(4):8135–8147.

Liang, C., Yan, N., Vidal, D., and Zou, X. (2012). Effects of coating formulation on coating thermal properties and coated paper print quality in xerography. *Nordic Pulp and Paper Research Journal*, 27(2):451–458.

Lucas, R. (1918). Über das Zeitgesetz des kapillaren Aufstiegs von Flüssigkeiten. *Kolloid Zeitschrift*, 23(1):15–22.

Lundberg, A., Örtegren, J., Alfthan, E., and Ström, G. (2011). Microscale droplet absorption into paper for inkjet printing. *Nordic Pulp and Paper Research Journal*, 26(1):142–150.

Lvovsky, A. (2013). *Encyclopedia of Optical Engineering*, chapter Fresnel Equations, pages 1–6. Taylor and Francis.

MacGregor, M. and Johansson, P. (1991). Submillimeter gloss variations in coated paper. Part 2: Studying orange peel gloss effects in lightweight coated paper. *Tappi Journal*, 74(1):187–194.

MacGregor, M. A. and Conners, T. E. (1987). Image Analysis of an LWC Paper reveals Wire Mark in the Print Density Variations. *Tappi journal*, 70(9):95–99.

Makinen, M., Kontturi, V., Jaaskelainen, T., and Parkkinen, J. (2008). Evaluation of print-through with colour theory: Uniform and nonuniform prints. *Journal of Pulp and Paper Science*, 34(3):161 – 169.

Makinen, M. O. A., Jaaskelainen, T., and Parkkinen, J. (2007). Evaluation of print-through with color theory. In *Coating and Graphic Arts Conference, TAPPI*, volume 1, pages 1 – 34, Miami, FL, United states.

Maldzius, R., Sirvio, P., Sidaravicius, J., Lozovski, T., Backfolk, K., and Rosenholm, J. B. (2010). Temperature-dependence of electrical and dielectric properties of papers for electrophotography. *Journal of Applied Physics*, 107(11):1149041–1149048.

Mandlez, D. (2015). Grundlagen des Inkjet Druck und die Inbetriebnahme eines Inkjet Druckers. Bachelor Thesis, TU Graz, Austria.

Mangin, P. and Dubé, M. (2006). Fundamental questions on print quality. In *Proceedings of SPIE - The International Society for Optical Engineering*, volume 6059.

Mangin, P. J., Beland, M.-C., and Cormier, L. M. (1994). Paper surface compressibility and printing. In *Proceedings of the International Printing and Graphic Arts Conference*, pages 19–31.

Mettänen, M. (2010). Methods for measuring and predicting the printability of paper. *Nordic Pulp and Paper Research Journal*, 25(3):391–404.

Mettänen, M. and Hirn, U. (2015). A comparison of five optical surface topography measurement methods. *Tappi Journal*, 14(1):27–38.

Namedanian, M., Nyström, D., Elias, P., and Gooran, S. (2014). Physical and optical dot gain: Characterization and relation to dot shape and paper properties. In

Proceedings of SPIE - The International Society for Optical Engineering, volume 9015.

Neter, J., Kutner, M., Nachtsheim, C., and Wasserman, W. (1996). *Applied Linear Statistical Models*. Irwin, Chicago, 4th edition.

Obradovic, J., Newnham, D., and Taday, P. (2007). Attenuated Total Reflection Explores the Terahertz Region. Technical Article 1457, American Laboratory.

Oittinen, P. and Saarelma, H. (1998). *Printing*. Number 13 in Papermaking Science and Technology. Fapet Oy.

Oittinen, P. and Saarelma, H. (2009). *Print Media - Principles, Processes and Quality*. Number 13 in Papermaking Science and Technology. Fapet Oy, 2nd edition.

Oko, A., Swerin, A., and Claesson, P. (2011). Imbibition and evaporation of water droplets on paper and solid substrates. *Journal of Imaging Science and Technology*, 55(1):102011–102016.

Olzak, L. A. and Thomas, J. (1986). *Seeing Spatial Patterns*. John Wiley & Sons.

O'Neill, M. and Jordan, B. (2000). Burnout test revisited. *Journal of Pulp and Paper Science*, 26(4):131–134.

Owens, D. and Wendt, R. (1969). Estimation of the Surface Free Energy of Polymers. *Journal of Applied Polymer Science*, 13(8):1741–1747.

Ozaki, Y., Bousfield, D., and Shaler, S. (2008). Characterization of coating layer structural and chemical uniformity for samples with backtrap mottle. *Nordic Pulp and Paper Research Journal*, 23(1):8–13.

Pal, L., Agate, S., and Fleming, P. (2007). Effects of Paper Manufacturing Factors on Inkjet Print Quality. In *International Conference on Digital Printing Technology*, pages 749–754.

Pauler, N. (2012). *Paper Optics*. AB Lorentzen and Wettre, second edition.

Pawlak, J. and Keller, D. (2004). Relationships between the local sheet structure and Z-direction compressive characteristics of paper. *Journal of Pulp and Paper Science*, 30(9):256–262.

Pedrotti, F. L. (2005). *Optik für Ingenieure: Grundlagen*. Springer, Berlin [u.a.], 3rd edition.

Peterson, R. and Williams, C. (1992). Determining paper-coating thickness with electron microscopy and image analysis. *Tappi Journal*, 75(10):122–126.

Petrou, M. (2004). Image registration: An overview. *Advances in Imaging and Electron Physics*, 130:243–291.

Preston, J. (2009). The surface analysis of paper. In l'Anson, S., editor, *14th Fundamental Research Symposium*, pages 749–837.

Preston, J., Hiorns, A., Elton, N., and Ström, G. (2008). Application of imaging reflectometry to studies of print mottle on commercially printed coated papers. *Tappi Journal*, 7(1):11–18.

Pykönen, M. and Aura, S. (2012). Experimental comparison of wettability by using pico- and microliter droplets with range of liquid surface tensions on porous and non-porous substrates. pages 239–241.

Ragnarsson, M., Engström, G., and Järnström, L. (2013). Porosity variations in coating layers - Impact on back-trap mottle. *Nordic Pulp and Paper Research Journal*, 28(2):257–263.

Rayleigh, L. (1878). On the Instability of Jets. *Proceedings of the London Mathematical Society*, s1-10(1):4–13.

Rehberger, M., Odeberg Glasenapp, A., and Örtegren, J. (2010). VDP on packaging - Elementary velocity study on inkjet-printed papers for corrugated board production. pages 198–222.

Resch, P., Bauer, W., and Hirn, U. (2010). Calendering effects on coating pore structure and ink setting behavior. *Tappi Journal*, 9(1):27–35.

Ridgway, C. and Gane, P. (2004). Ink-coating adhesion: The importance of pore size and pigment surface chemistry. *Journal of Dispersion Science and Technology*, 25(4):469–480.

Ridgway, C., Gane, P., and Schoelkopf, J. (2002). Effect of capillary element aspect ratio on the dynamic imbibition within porous networks. *Journal of Colloid and Interface Science*, 252(2):373–382.

Rutar, V. and Scheicher, L. (2009). Analysis of paper properties for laser printing and black and white and colour print quality. *Paper Technology*, 50(4):45–48.

Sadovnikov, A., Lensu, L., and Kälviäinen, H. (2008). On estimation of perceived mottling prior to printing. *Proceedings of SPIE - The International Society for Optical Engineering*, 6808.

Sanders, D., Rutland, D., and Istone, W. (1996). Effect of paper properties on fusing fix. *Journal of Imaging Science and Technology*, 40(2):175 – 179.

Schoelkopf, J. (2002). *Observation and modelling of fluid transport into porous paper coating structures*. PhD thesis, University of Plymouth.

Schoelkopf, J., Gane, P., Ridgway, C., and Matthews, G. (2002). Practical observation of deviation from Lucas-Washburn scaling in porous media. *Colloids and Surfaces A: Physicochemical and Engineering Aspects*, 206(1-3):445–454.

Schoelkopf, J., Ridgway, C., Gane, P., Matthews, G., and Spielmann, D. (2000). Measurement and network modeling of liquid permeation into compacted mineral blocks. *Journal of Colloid and Interface Science*, 227(1):119–131.

Schultz-Eklund, O., Fellers, C., and Johansson, P. (1992). Method for the local determination of the thickness and density of paper. *Nordic Pulp and Paper Research Journal*, 7(3):133–139.

Simula, S., Ikalainen, S., Niskanen, K., Varpula, T., Seppa, H., and Paukku, A. (1999). Measurement of the dielectric properties of paper. *Journal of Imaging Science and*

Technology, 43(5):472–477.

Singh, S. (2008). A comparison of different methods of paper surface smoothness evaluation. *BioResources*, 3(2):503–516.

Sirvio, P. and Backfolk, K. (2008). Effect of roughness of low-grammage coated papers on print quality in color electrophotography. *Journal of Imaging Science and Technology*, 52(1).

Sirvio, P., Backfolk, K., Maldzius, R., Sidaravidus, J., and Montrimas, E. (2008). Dependence of paper surface and volume resistivity on electric field strength. *Journal of Imaging Science and Technology*, 52(3).

Sirvio, P., Sidaravicius, J., Lozovski, T., Kuskevicius, S., and Backfolk, K. (2009). Dosed charging: Application to the investigation of papers. *Journal of Electrostatics*, 67(5):730–736.

Ström, G., Karathanasis, M., and Preston, J. (2010). Impact of coating surface properties and print impression on the non-uniformity of sheet-fed offset prints. In *11th Advanced Coating Fundamentals Symposium Proceedings: The Latest Advances in Coating Research and Development*, pages 254–278.

Ström, G. and Preston, J. (2013). Impact of local variation in coating structure on uniformity in print gloss. *Tappi Journal*, 12(5):43–51.

Sung, Y., Ham, C., Kwon, O., Lee, H., and Keller, D. (2005). Application of Thickness and Apparent Density Mapping by Laser Profilometry. In l'Anson, S., editor, *13th Fundamental Research Symposium*, pages 961–1007.

Svanholm, E. (2007). *Printability and Ink-Coating Interactions in Inkjet Printing*. PhD thesis, Karlstad University.

Tomimasu, H., Kim, D., Suk, M., and Luner, P. (1991). Comparison of four paper imaging techniques: Beta-radiography, electrography, light transmission and soft X-radiography. *Tappi Journal*, 74(7):165–176.

Tomimasu, H., Luner, P., and Hanna, R. (1989). Rapid Imaging of Mass Distribution in Paper by Electron Beams. In l'Anson, S., editor, *9th Fundamental Research Symposium*, pages 159–194.

Tomimasu, H., Suzuki, K., and Ogura, T. (1990). The effect of basestock structure on coating weight distribution. *Tappi Journal*, 5(73):179–187.

Trepanier, R., Jordan, B., and Nguyen, N. (1998). Specific perimeter: A statistic for assessing formation and print quality by image analysis. *Tappi Journal*, 81(10):191–196.

Trimmel, M., Hirn, U., and Bauer, W. (2012). A new burnout test for wood containing papers. In *8th International Paper and Coatings Chemistry Symposium, Stockholm, Sweden*, pages 121–124.

Vyörykkä, J., Juvonen, K., Bousfield, D., and Vuorinen, T. (2004). Raman microscopy in lateral mapping of chemical and physical composition of paper coating. *Tappi*

Journal, 3(9):19–24.

Wagberg, P. and Johansson, P. (1993). Surface profilometry - a comparison between optical and mechanical sensing on printing papers. *Tappi Journal*, 76(12):115–121.

Walker, W. and Fetsko, J. (1955). A Concept of Ink Transfer in Printing. *American Ink Maker*, pages 38–71.

Washburn, E. (1921). The dynamics of capillary flow. *Physical Review*, 17(3):273–283.

Wikström, M., Nylund, T., and Rigdahl, M. (1997). Calendering of coated paper and board in an extended soft nip. *Nordic Pulp and Paper Research Journal*, 12(4):289–298.

Wiltsche, M., Bauer, W., and Donoser, M. (2006). Coating application method and calendering influence on the spatial coating layer formation obtained by an automated serical sectioning method. In *TAPPI Advanced Coating Fundamentals Symposium Proceedings*, volume 2006, pages 393–405.

Wind, E. (2011). *Untersuchung der Ursache für kleinräumige Druckbildstörungen im Heatset Web Offset Druck an ungestrichenen Papieren*. PhD thesis, Graz University of Technology.

Wink, W. and Baum, G. (1983). A rubber platen caliper gauge - a new concept in measuring paper thickness. *Tappi Journal*, 66(9):131–133.

Xiang, Y., Bousfield, D., Hassler, J., Coleman, P., and Osgood, A. (1999). Measurement of local variation of ink tack dynamics. *Journal of Pulp and Paper Science*, 25(9):326–330.

Yang, L. (2003). *Ink-Paper interaction, a study in ink-jet color reproduction*. PhD thesis, Linköping University.

Yang, L., Fogden, A., Pauler, N., Savborg, O., and Kruse, B. (2005). A novel method for studying ink penetration of a print. *Nordic Pulp and Paper Research Journal*, 20(4):423 – 429.

Yang, Y., Hu, S., and Liu, F. (2011). Establishment of ink penetration model and the calculation of penetration depth inside paper. In *Advanced Materials Research*, volume 295-297, pages 2028 – 2032, Sanya, China.

Zang, Y.-H. (1993). A new approach for modelling ink transfer. *Tappi Journal*, 76(7):97–103.

Zhang, Y., Liu, Z., Cao, Y., Li, R., and Jing, Y. (2015). Impact of binder composition on inkjet printing paper. *BioResources*, 10(1):1462–1476.

Zou, X., Allem, R., and Uesaka, T. (2001). Relationship between coating uniformity and basestock structures. Part 1: Lightweight coated papers. *Paper Technology*, 42(5):27–37.